The VIRUS-P Exploration of Nearby Galaxies (VENGA): spatially resolved gas-phase metallicity distributions in barred and unbarred spirals

Kyle F. Kaplan,[1]★ Shardha Jogee,[1]★ Lisa Kewley,[2] Guillermo A. Blanc,[3,4,5]
Tim Weinzirl,[6] Mimi Song,[1] Niv Drory,[1] Rongxin Luo[7]
and Remco C. E. van den Bosch[8]

[1]*Department of Astronomy, University of Texas at Austin, 2515 Speedway, Stop C1400, Austin, TX 78712-1205, USA*
[2]*Research School of Astronomy and Astrophysics, The Australian National University, Cotter Road, Weston Creek, ACT 2611, Australia*
[3]*Departamento de Astronomía, Universidad de Chile, Camino del Observatorio, 1515 Las Condes, Santiago, Chile*
[4]*Centro de Astrofísica y Tecnologías Afines (CATA), Camino del Observatorio, 1515 Las Condes, Santiago, Chile*
[5]*Visiting Astronomer, Observatories of the Carnegie Institution for Science, 813 Santa Barbara St, Pasadena, CA 91101, USA*
[6]*School of Physics and Astronomy, University of Nottingham, Nottingham NG7 2RD, UK*
[7]*Shanghai Astronomical Observatory, 80 Nandan Road, Shanghai 200030, China*
[8]*Max Planck Institute for Astronomy, Königstuhl 17, D-69117 Heidelberg, Germany*

ABSTRACT

We present a study of the excitation conditions and metallicity of ionized gas (Z_{gas}) in eight nearby barred and unbarred spiral galaxies from the VIRUS-P Exploration of Nearby Galaxies (VENGA) survey, which provides high spatial sampling and resolution (median $\sim$387 pc), large coverage from the bulge to outer disc, broad wavelength range (3600–6800 Å), and medium spectral resolution ($\sim$120 km s^{-1} at 5000 Å). Our results are: (1) We present high resolution gas excitation maps to differentiate between regions with excitation typical of Seyfert, LINER, or recent star formation. We find LINER-type excitation at large distances (3–10 kpc) from the centre, and associate this excitation with diffuse ionized gas (DIG). (2) After excluding spaxels dominated by Seyfert, LINER, or DIG, we produce maps with the best spatial resolution and sampling to date of the ionization parameter q, star formation rate, and Z_{gas} using common strong line diagnostics. We find that isolated barred and unbarred spirals exhibit similarly shallow Z_{gas} profiles from the inner kpc out to large radii (7–10 kpc or 0.5–1.0 R_{25}). This implies that if profiles had steeper gradients at earlier epochs, then the present-day bar is not the primary driver flattening gradients over time. This result contradicts earlier claims, but agrees with recent IFU studies. (3) The Z_{gas} gradients in our $z \sim 0$ massive spirals are markedly shallower, by $\sim$0.2 dex kpc^{-1}, than published gradients for lensed lower mass galaxies at $z \sim$ 1.5–2.0. Cosmologically motivated hydrodynamical simulations best match this inferred evolution, but the match is sensitive to adopted stellar feedback prescriptions.

Key words: galaxies: abundances – galaxies: ISM – galaxies: spiral.

1 INTRODUCTION

The spatially resolved distribution of a galaxy's gas phase metallicity is an important signpost of its assembly history and reflects the complex cycle of baryonic inflows and outflows, star formation (SF), as well as stellar and AGN feedback. The metallicity of the gas phase in H II regions is traced by the relative abundance of oxygen to hydrogen, which we quantify as $Z_{gas} \equiv \log(O/H)+12$. The accretion of metal-poor gas by galaxies in the form of halo accretion and proposed cold mode accretion (Kereš et al. 2005, 2009; Dekel &

Birnboim 2006; Dekel et al. 2009b; Dekel, Sari & Ceverino 2009a) can initially depress Z_{gas} within the galaxy, but can subsequently fuel SF that leads to enrichment. Galaxy mergers and interactions influence Z_{gas} by inducing stellar bars, driving gas inflows, triggering SF, and possibly fuelling AGN activity (Somerville & Primack 1999; Cole et al. 2000; Springel, Di Matteo & Hernquist 2005; Conselice 2009; Jogee et al. 2009; Lotz et al. 2011). Secular processes, such as gas inflows driven by the bar inside its co-rotation resonance (Kormendy & Kennicutt 2004; Jogee, Scoville & Kenney 2005) transport metal-poor gas from the outer disc of a galaxy towards the circumnuclear region, and often trigger powerful bursts of SF that chemically enrich the circumnuclear gas. Simulations suggest that

★ E-mail: kfkaplan@astro.as.utexas.edu (KFK); sj@astro.as.utexas.edu (SJ)

gas outflows powered by supernovae, stellar winds and/or photons from massive stars, and variations in the star formation efficiency play important roles in shaping the gas phase metallicity of galaxies (Brooks et al. 2007; Oppenheimer et al. 2010; Davé, Finlator & Oppenheimer 2011; Faucher-Giguère, Kereš & Ma 2011; Pilkington et al. 2012; Gibson et al. 2013). Many observational studies over the last decade have explored how the global integrated metallicity of galaxies correlates with other properties, such as luminosity, stellar mass, and SFR. The so-called mass metallicity relation (MZR) between total stellar mass and gas phase metallicity is remarkably tight over a wide range in stellar mass (Tremonti et al. 2004; Lee et al. 2006; Zhao, Gao & Gu 2010). Some studies suggest that the MZR has a second-parameter dependence on the SFR (Ellison et al. 2008; Lara-López et al. 2010; Mannucci et al. 2010), but this is debated by other studies (Sánchez et al. 2013; Wuyts et al. 2014).

In contrast, our knowledge of the spatially resolved distributions of Z_{gas} within galaxies has been very limited. The first studies of the distributions of Z_{gas} in nearby galaxies were done through multislit spectroscopy targeting bright H II regions, or with long-slit drift scans (e.g. Moustakas et al. 2010). Several studies (Vila-Costas & Edmunds 1992; Martin & Roy 1994; Zaritsky, Kennicutt & Huchra 1994; Dutil & Roy 1999; Henry & Worthey 1999; Considère et al. 2000; Dors & Copetti 2005; Florido et al. 2012) have explored Z_{gas} in galaxies of different morphologies, and some of them (Vila-Costas & Edmunds 1992; Martin & Roy 1994; Zaritsky et al. 1994; Dutil & Roy 1999; Henry & Worthey 1999) claim that barred spirals exhibit flatter Z_{gas} gradients than unbarred spirals.

Studies by Krabbe et al. (2008, 2011), Rupke, Kewley & Chien (2010), Kewley et al. (2010), Rosa et al. (2014), and Torres-Flores et al. (2014) claim that pairs of interacting galaxies have flatter Z_{gas} gradients than isolated galaxies due to gas flows driven by the interactions. However, studies with slit spectroscopic data often suffer from poor spatial sampling and incomplete coverage. Additionally, those studies without adequate spatial information or wavelength coverage cannot identify and exclude contaminated regions where gas is not primarily excited by photons from young massive stars.

High resolution, high-quality, integral field unit (IFU) spectroscopic data allow us to more accurately explore the gas phase metallicity distribution within barred and unbarred spirals of different Hubble types. Two recent studies by Sánchez et al. (2012, 2014) based on the PINGS (Rosales-Ortega et al. 2010) and CALIFA (Sánchez et al. 2011) IFU surveys have explored Z_{gas} in spiral galaxies. Both studies find the Z_{gas} gradients in their samples are independent of Hubble Type or being barred versus unbarred when scaled to a common effective radius (R_e). For interacting spirals, the IFU study by Rich et al. (2012) finds that Z_{gas} gradients in their sample of strongly interacting galaxies to be flatter than isolated spirals, in agreement with the earlier studies.

In this paper, we present a complementary IFU-based study of the gas phase metallicity in a sample of barred and unbarred spirals drawn from the VIRUS-P Exploration of Nearby Galaxies (VENGA) survey (Blanc et al. 2013a). Our sample of eight barred and unbarred spirals was drawn from the full VENGA sample of 30 spirals by selecting galaxies at intermediate distances (8–33 Mpc) so that the IFU data cover a large fraction of the galaxy's outer disc, while simultaneously providing a high spatial resolution (a few hundred pc). The combination of spatial coverage and resolution allows us to resolve individual galactic components, such as the bulge, primary stellar bar, outer disc, and separate regions of widely different excitation (e.g. H II regions, spiral arms, starburst or AGN driven outflows, diffuse ionized gas, etc.).

The IFU-based study in this paper complements the studies by Sánchez et al. (2012, 2014) in several respects. While our study

has a smaller sample than Sánchez et al. (2012, 2014), it benefits from a high spatial resolution (median of 387 pc), a high spectral resolution (120 km s^{-1} at 5000 Å), a broad blue-to-red wavelength coverage (3600–6800 Å), and the use of seven Z_{gas} diagnostics. The cross-comparisons between these seven Z_{gas} diagnostics allows us to break degeneracies in values of Z_{gas} (Section 4.5) and can aid other studies (e.g. at high redshifts) limited to only a few Z_{gas} diagnostics.

Another strength of this study is that it systematically tackles the following issues that have plagued many earlier long-slit and IFU-based Z_{gas} studies: (i) Many Z_{gas} diagnostics work well when using emission line ratios from gas that is predominantly ionized by photons from local massive stars, but break down when the gas is predominantly ionized by a hard radiation field from an AGN or is shocked (e.g. in starburst-driven outflows). Studies without the spatial resolution needed to exclude contaminated regions often yield erroneous Z_{gas} values, as emphasized by Kewley & Dopita (2002), Kewley & Ellison (2008), and Yuan et al. (2012). We avoid this pitfall by removing regions dominated by Seyfert or LINER conditions, as well as regions dominated by diffuse ionized gas (DIG) before calculating Z_{gas}. (ii) The value of some Z_{gas} diagnostics (e.g. $R_{23} \equiv$ ([O II]λ3727+[O III]$\lambda\lambda$4959,5007/Hβ) depend on the ionization parameter q, but not all calibrations of Z_{gas} take this into account. In this work, we calculate *spatially resolved* maps of q across the bulge, bar, and outer disc.

This paper is organized as follows: Section 2.1 introduces the VENGA IFU survey; Section 2.2 describes the selection of our sub-sample of eight nearby spirals; and Section 3 covers the data reduction. For our methodology, Section 4.1 discusses the use of excitation diagnostic diagrams to remove Seyfert and LINER contaminated regions; Section 4.2 discusses how we identify and remove regions dominated by emission from DIG; Section 4.3 details how we compute SFRs; Section 4.4 describes our computation of the ionization parameter q; and Section 4.5 shows how we derive the seven different Z_{gas} diagnostics. For our results, Section 5.1 presents the spatially resolved maps and deprojected radial profiles of Z_{gas}, q, and SFR; Section 5.2 compares the absolute value of Z_{gas} between the different diagnostics; Section 5.3 presents our results on the Z_{gas} distributions in our barred and unbarred galaxies; Section 5.4 compares our Z_{gas} profiles in nearby spirals to published profiles for high redshift galaxies; and Section 5.5 compares the observed evolution in Z_{gas} profiles from $z \sim 2$ to 0 with the evolution predicted by different suites of simulations. Section 6 presents our summary and conclusions.

2 OBSERVATIONS AND SAMPLE

2.1 VENGA

VENGA is an integral field spectroscopic survey of the inner and outer regions of the disc of a sample of 30 nearby spiral galaxies with the Mitchell Spectrograph (formerly called VIRUS-P) IFU on the 2.7 metre telescope at McDonald Observatory (Blanc et al. 2013a). The Mitchell Spectrograph has large (5.6 arcsec full width half-maximum [FWHM]) sensitive fibres and the largest FOV (110 arcsec × 110 arcsec or 3.36 arcmin^2) among existing IFUs (Hill et al. 2008). Over four years, this survey has been allocated ∼150 nights of observing time (PIs: G. Blanc and T. Weinzirl). Three dithers are performed on each galaxy to compensate for the 1/3 filling factor of the Mitchell Spectrograph, and multiple pointings are used to acquire spectra over a large fraction of the R_{25} radius (the galactocentric radius where the B-band surface brightness = 25 mag arcsec^{-2}) of each galaxy's disc (Fig. 1). Each galaxy is observed with both a blue (3600–5800 Å) and red (4600–6800 Å)
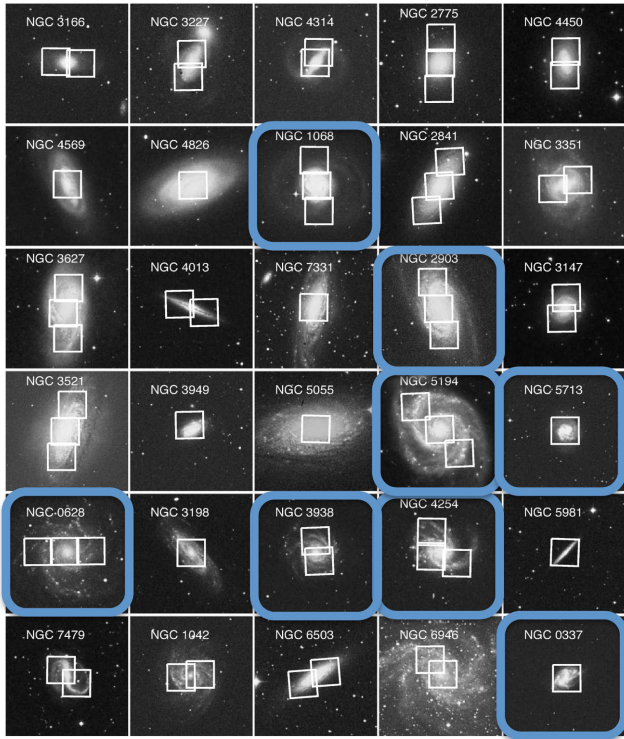
Figure 1. DSS[1] images of the VENGA sample of 30 nearby spiral galaxies are overlaid with squares, which indicate the individual pointings of the Mitchell Spectrograph IFU. Blue highlights our sub-sample of eight spirals which are selected to maximize both our spatial resolution and spatial coverage of the disc for studying Z_{gas} (see Section 2.2).

setup to obtain a wide wavelength coverage. The spectral resolution is $R \approx 1000$ or ~ 5 Å FWHM at 5000 Å, which corresponds to ~ 120 km s^{-1}. An example 1D VENGA spectrum from the galaxy NGC 0628 can be found in Blanc et al. (2013a).

The VENGA sample consists of 30 nearby spirals at distances out to 50 Mpc, 80 per cent of which are closer than 20 Mpc. All the target galaxies are shown in Fig. 1. The VENGA sample was chosen to cover a range of Hubble types (Sa to Sd), inclinations from face to edge on, include galaxies with classical bulges and pseudo-bulges (e.g. Kormendy & Kennicutt 2004; Fisher & Drory 2008; Weinzirl et al. 2009), as well as include barred and unbarred spirals. The VENGA galaxies have a global SFR typically in the range of 0.5–10 M$_\odot$ yr^{-1}, and stellar masses primarily in the range of 10^9–10^{11} M$_\odot$, and for those galaxies with stellar mass above 10^{10} M$_\odot$, they span a representative range of the stellar mass-SFR plane, as shown in Blanc et al. (2013a). Most galaxies have ancillary data from a variety of sources including *HST*, *Spitzer*, *GALEX*, CO maps from BIMA SONG (Helfer et al. 2003) and the CARMA CO survey STING (Rahman et al. 2011), archival HI 21 cm maps from THINGS (Walter et al. 2008) and ALFALFA (Giovanelli et al. 2005). Half of the VENGA sample is covered by the KINGFISH survey (Kennicutt et al. 2011).

---

[1] The Digitized Sky Surveys were produced at the Space Telescope Science Institute under U.S. Government grant NAG W-2166. The images of these surveys are based on photographic data obtained using the Oschin Schmidt Telescope on Palomar Mountain and the UK Schmidt Telescope. The plates were processed into the present compressed digital form with the permission of these institutions.

2.2 Sub-sample selection

We selected a subset of eight spiral galaxies from the 30 VENGA spirals for our study of Z_{gas}, based on the four criteria below. In particular, we simultaneously require IFU data coverage over a large fraction of the galaxy's disc (criterion ii), as well as high spatial resolution (criteria iii and iv; Table 1).

(i) *Inclination*. A very high inclination results in large extinction by dust and makes it difficult to spatially resolve the separate galactic components. Face-on galaxies lack information on the kinematics of the stars and gas, which is important for detecting azimuthal and radial motions. To balance out these two extremes, our sub-sample covers a range of low to moderate inclinations, between $9°$ and $66°$,[2] with a median of $35°$.

(ii) *Fraction of R_{25}*. R_{25} is the galactocentric radius where the *B*-band surface brightness equals 25 mag arcsec^{-2}. We select galaxies where the fraction of the disc's R_{25} radius ($f_{R_{25}}$) covered by the Mitchell Spectrograph observations is at least 35 per cent ($f_{R_{25}} > 0.35$). Our sample has $f_{R_{25}}$ ranging from 0.38 to 0.81 with a median of 0.66.

(iii) *(R_e-bulge/FPSF)*. For galaxies with significant bulges (bulge-to-total ratio B/T > 0.01), we ensure that we resolve the bulge by requiring that (R_e-bulge/FPSF) > 1, where R_e-bulge denotes the half-light radius of the bulge and FPSF is the FWHM of the point spread function (PSF) of the observations (5.6 arcsec). Our sub-sample has a median (R_e-bulge/FPSF) of 2.2.

(iv) *Spatial resolution*. In addition to the relative requirement (R_e-bulge/FPSF) > 1, we also require an absolute spatial resolution of FPSF < 900 pc in order to resolve the individual galactic components such as the bulge, primary stellar bar, outer disc, and to separate regions of different excitations (e.g. H II regions, starburst or AGN driven outflows, DIG, etc.). This condition sets the maximum distance of our sub-sample to be ~ 33 Mpc. With a combination of criteria (ii)–(iv), we obtain a sub-sample of eight galaxies with a median distance of 14.3 Mpc, giving us a median spatial resolution of 387 pc.

Table 1 shows our sub-sample of eight VENGA spiral galaxies satisfying the above selection criteria. The sample spans a range of Hubble types from Sab to Sd. It includes six isolated galaxies, of which two are barred (NGC 2903 and 5173) and four are unbarred (NGC 0628, 1068, 3938, and 4254), as well as one weakly interacting barred galaxy (NGC 0337), and one weakly interacting unbarred galaxy (NGC 5194 or M51a). We describe the interacting systems in our study as weakly interacting because they are consistent with minor interactions/mergers with mass ratios below 1:3. NGC 5194 or M51a is interacting with a dwarf galaxy (M51b), while NGC 0337 shows subtle asymmetries in the stellar distribution of its disc. When assigning a bar type to the sample, we do not use only the optically based visual bar classification in RC3, but further verify the bar type using quantitative analyses of near-infrared images in Section 5.3.

Table 2 compares previous IFU studies of the distribution of Z_{gas} in spiral galaxies to the IFU study in this paper. The study by Sánchez et al. (2012) analyses data of 7 spirals from the PINGS (Rosales-Ortega et al. 2010) IFU survey and 31 spirals from the CALIFA (Sánchez et al. 2011) IFU survey. Their median spatial

---

[2] In the initial selection of our sub-sample, we used the inclination from Tully (1988) for all galaxies, and our subsample had an inclination range of $27°$–$66°$. However, at the time of submission of this paper, we adopted the lower inclination of $8°.7$ published for NGC 0628 (Blanc et al. 2013a), compared to the value of $27°$ from Tully (1988).

Table 1. Our sub-sample of VENGA spirals.

NGC	D (Mpc)	$a_{25} \times b_{25}$ (′)	i (°)	Type	$M_\star$	Bar?	Inter.?	B/T	R_e-bulge (pc)	Bulge n	FPSF (pc)	Ratio	$f_{R_{25}}$
(1)	(2)	(3)	(4)	(5)	(6)	(7)	(8)	(9)	(10)	(11)	(12)	(13)	(14)
0337	19.3^α	1.44×0.91	55	SB(s)d	1.6E+10	y	y^a				523		0.72
0628	8.6^β	5.24×4.78	9^b	SA(s)c	2.0E+10	n	n	0.10	600	1.35	268	2.24	0.47
1068	10.1	3.54×3.01	35	SA(rs)b	7.9E+10	n	n				273		0.72
2903	8.9	6.29×3.01	66	SAB(rs)bc	5.0E+10	y	n	0.09	360	0.42	241	1.49	0.38
3938	17.9	2.69×2.45	27	SA(s)c	3.2E+10	n	n	0.07	560	1.18	485	1.15	0.60
4254	14.3	2.69×2.34	33	SA(s)c	4.0E+11	n	n	0.39	2110	2.68	387	5.45	0.81
5194	8.4	5.61×3.46	56	SA(s)bc	7.9E+10	n	y				228		0.56
5713	32.6	1.38×1.23	30	SAB(rs)bc	7.9E+10	y	n	0.33	2460	1.84	883	2.79	0.66

Columns: (1) Galaxy NGC number. NGC 5194 is also commonly known as M51a. (2) Distance D to galaxy in Mpc. For NGC 03337 and 4254, we use Springob et al. (2007). For NGC 0628, we adopt the value from Herrmann et al. (2008), also used in Blanc et al. (2013a). For NGC 1068, we use Tully et al. (2008). For NGC 2903 we use Drozdovsky & Karachentsev (2000). For NGC 3938 and 5194, we use Poznanski et al. (2009). For NGC 5713, we use Tully (1988), corrected H_0 from 75 to 70 km/s/Mpc. (3) The major axis a_{25} and minor axis b_{25} of the galaxy's projected radius R_{25} from RC3 (de Vaucouleurs et al. 1991). R_{25} is defined as the radius where the surface brightness of the outer disc reaches 25 mag arcsec^{-2} in the *B*-band. (4) For all galaxies, except NGC 0628, we adopt the inclination based on Tully (1988), calculated from inclination $= \cos^{-1}\left(\sqrt{\left[(a_{25}/b_{25})^2 - 0.2^2\right] / \left[1 - 0.2^2\right]}\right) + 3°$. For NGC 0628, we adopt the inclination value of 8°7 published by Blanc et al. (2013a), compared to the value of 27° from Tully (1988). (5) Hubble type from RC3 (de Vaucouleurs et al. 1991). (6) Total stellar mass in units of $M_\odot$ from Blanc et al. (2013a). (7) Does galaxy host a large-scale stellar bar? In assessing the presence or absence of a large-scale stellar bar, we do not rely only on the RC3 classification based on visual inspection of optical photographic plates, but instead base the final assessment on the quantitative analyses of near-infrared images, as detailed in Table 6. (8) Is galaxy interacting? We use interaction status from NED unless otherwise indicated. ^{a}In the case of NGC 0337, which NED[3] characterizes as non-interacting, The Carnegie Atlas of Galaxies (Sandage & Bedke 1994) classifies NGC 0337 as Sc(s)II.2 pec due to the patchiness and asymmetry in the stellar distribution. Our own data also shows the same patchiness and asymmetry in both the stellar and Hα distributions (see Fig. 3), prompting us to classify this galaxy as weakly interacting. (9) Bulge-to-total (B/T) mass ratio. Reported ratios for NGC 0628 and 2938 are from Fisher & Drory (2008), the ratio for NGC 2903 is from Dong & De Robertis (2006), and the ratios for NGC 4254 and 5713 are from Weinzirl et al. (2009). For galaxies where bulge-plus-disc decomposition has not been performed, no bulge parameters are listed. (10) Bulge half-light radius R_e-bulge. See note for column 9 for references. (11) Bulge Sérsic index. See note for column 9 for references. (12) Spatial resolution FPSF (defined as the full width half-maximum of the point spread function) of the Mitchell Spectrograph. (13) Ratio (R_e-bulge/FPSF) of the bulge half-light radius R_e to the spatial resolution of the Mitchell Spectrograph. (14) Fraction of the major axis a_{25} of the R_{25} radius covered by VENGA. This is illustrated in Fig. 1.

Table 2. Comparison of IFU studies of Z_{gas} in nearby spirals.

Study (1)	No. of spirals analysed (2)	Parent IFU Survey (3)	Median dist. (Mpc) (4)	Median res. (pc) (5)	Wavelength range (Å) (6)	Spectral res. (km s^{-1}) (7)	No. of Z_{gas} diagnostics (8)
This study	8	VENGA	14.3	387	3600–6800	120 @ 5000 Å	7
Sánchez et al. (2012)	7	PINGS	10.6	103	3700–6900	600 @ 5400 Å	3
	31	CALIFA	66.4	644	3700–6900	600 @ 5400 Å	3
Sánchez et al. (2014)	306	CALIFA	68	985	3745–7500	350 @ 5600 Å	1

Columns: (1) IFU study of Z_{gas} radial profiles. (2) Number of spiral galaxies analysed in study. (3) Parent IFU study. (4) Median distance to galaxies in study in Mpc. (5) Median spatial resolution of study in pc. (6) Wavelength range from blue to red of IFU used in Å. (7) Spectral resolution of study in km s^{-1}. (8) Number of Z_{gas} diagnostics used in study.

resolution is 644 pc, the spectral resolution is 600 km s^{-1} at 5000 Å, and only three diagnostics of Z_{gas} are used (Table 2). The more recent study by Sánchez et al. (2014) uses 306 spiral galaxies from CALIFA with a median spatial resolution of 985 pc, a spectral resolution of 350 km s^{-1} at 5000 Å, and uses only one Z_{gas} diagnostic (Table 2). In contrast, our IFU study of 8 spirals in this paper has a higher median spatial resolution (387 pc), a higher spectral resolution (120 km s^{-1} at 5000 Å), and uses a full set of seven Z_{gas} diagnostics.

3 DATA REDUCTION

The data reduction pipeline VACCINE (Adams et al. 2011) is used to perform the basic data reduction, including the bias and dark subtraction, flat fielding, wavelength calibration, cosmic ray rejection and sky subtraction. Fig. 2 illustrates our data reduction and analysis steps (Adams et al. 2011; Blanc et al. 2013a). After running VACCINE, a custom made sky subtraction method based on a spline interpolation of all available sky exposures throughout each night is performed. Flux calibration is conducted in two steps. The first step uses spectrophotometric standard star frames for wavelength-dependent flux calibration for each observing run. The second step uses SDSS broad-band images (Alam et al. 2015) to perform absolute flux calibration and astrometry correction to compensate for changing weather conditions and uncertainty in the pointings. The uncertainty for the flux in each fibre is a combination of the readout noise, Poisson uncertainty, and systematic error. Calculation of the

[3] The NASA/IPAC Extragalactic Database (NED) is operated by the Jet Propulsion Laboratory, California Institute of Technology, under contract with the National Aeronautics and Space Administration. (https://ned.ipac.caltech.edu/)
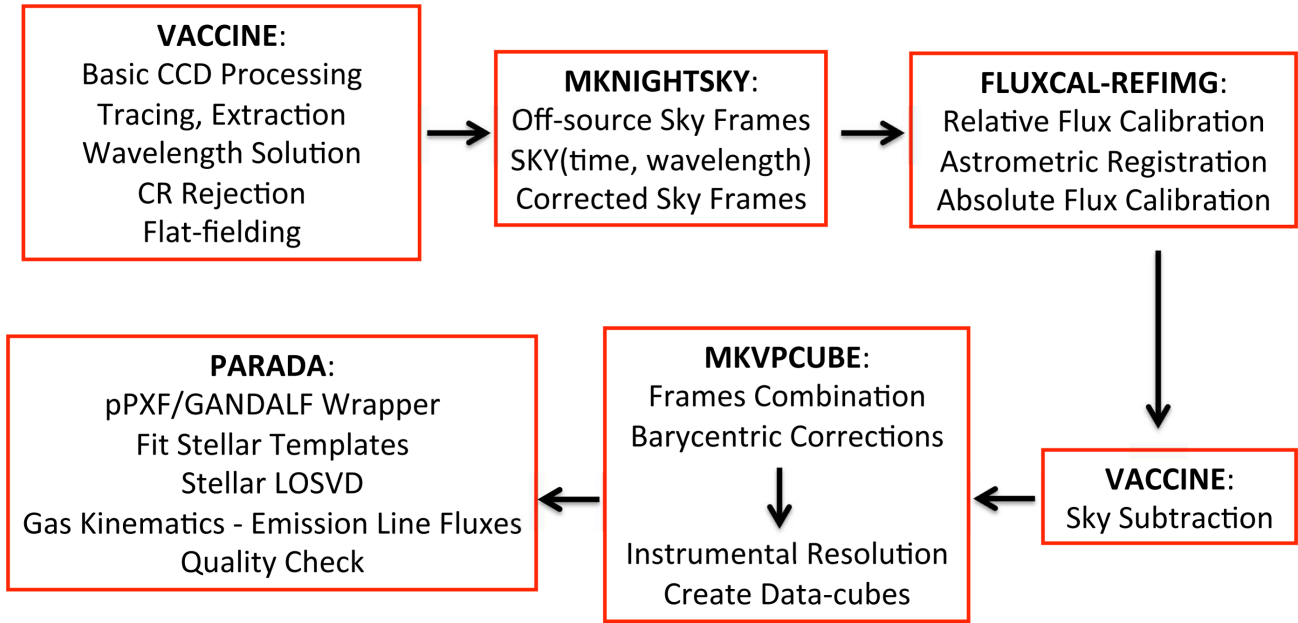
Figure 2. Flow chart of our data reduction and analysis pipeline, as outlined in Section 3.

uncertainty is detailed in Blanc et al. (2013a). Finally, all science frames are combined into a data cube which is regularly spaced in right ascension, declination, and wavelength. The spaxel size in the data cube is 2 arcsec, which implies a Nyquist sampling of the PSF FWHM.

We extract the emission lines from the underlying stellar continuum by using PARADA, a modified version of GANDALF (Sarzi et al. 2006). To fit the stellar continuum, we use the MILES (Sánchez-Blázquez et al. 2006) empirical stellar library, which has over 900 stars with a wide range of spectral types and metallicities, and is accurately flux-calibrated (with typical differences between photometric data bases and synthetic colours derived from MILES of <0.1 mag). Each MILES stellar spectrum is convolved to the wavelength-dependent Mitchell Spectrograph spectral resolution (median of ∼5 Å FWHM at 5000 Å). The observed spectra are fit with the templates in pixel space using the Penalized Pixel-Fitting (pPXF; Cappellari & Emsellem 2004) method, from which the stellar continuum and kinematics are extracted.

Galactic extinction is corrected using the extinction map of Schlegel, Finkbeiner & Davis (1998). Spectra are decomposed by Gaussian-shaped emission lines being simultaneously fitted with the underlying stellar continuum. A multiplicative high order Legendre polynomial is used to account for the internal reddening. We check the quality of our data using a technique outlined by Oh et al. (2011), comparing the residuals of our fits of the stellar continuum and emission lines to the statistical noise in the data. Regions with residuals greater than three times the noise are flagged and removed. Typically only a few per cent of the regions are flagged by this quality check and many of these regions are also flagged and removed by other means (e.g. signal-to-noise cuts, DIG, excitation diagnostics; Sections 4.1 and 4.2).

Galactic stars are a source of contamination in the spaxels of our 2D maps and must be masked out. They are identified as regions which have a stellar velocity that deviates more than 50 km s^{-1} from the average stellar velocity over a 10 arcsec radius. Identified galactic stars are then removed from further analysis by masking out spaxels within a 2 arcsec radius of the identified star.

The resulting data cubes store spatially resolved 2D information on the gas emission line fluxes, stellar continuum spectra, stellar and gas velocities, and velocity dispersions from which we will derive excitation diagrams, Z_{gas}, SFRs, and the ionization parameter q. All emission line fluxes are corrected for extinction by dust intrinsic to the observed galaxies using the Hα/H$\beta = 2.86$ line ratio decrement described in Osterbrock & Ferland (2006). Examples of the data products, such as the stellar flux, stellar velocity field, extinction corrected Hα map, and Hα velocity field are shown for NGC 2903 in Fig. 3. For the isovelocity contours, we use Voronoi binning for regions with low signal-to-noise (S/N), with a minimum of S/N ≥ 3 for Hα and a minimum S/N ≥ 50 for the stellar continuum.

4 METHODOLOGY

For our analysis, we first identify in each galaxy 'star-forming' regions or spaxels where the ionized gas is predominantly photoionized by massive hot young stars, and we exclude contaminating spaxels where the gas is mainly excited by the hard radiation field of an AGN or by shocks (Section 4.1). We also exert particular care in dealing with diffuse ionized gas (Section 4.2). We then use only the 'star-forming' spaxels for calculating SFRs (Section 4.3), the ionization parameter q (Section 4.4), and Z_{gas} (Section 4.5).

4.1 Identifying gas in different excitation conditions (SF, Seyfert, LINER)

Gas metallicity (Z_{gas}) diagnostics are all based on the assumption that the emission line fluxes we measure stem from gas that is predominantly being photoionized by UV light from massive hot young stars. However, if the gas is predominantly ionized by other sources, such as AGN or shocks in the gas, then Z_{gas} values computed from the measured emission line ratios will be incorrect as discussed by Kewley & Dopita (2002), Kewley & Ellison (2008), and Yuan et al. (2012). In this study, we avoid regions predominantly ionized by sources other than young massive stars by using high spatial resolution IFU data to probe regions on scales of a few hundred pc, and by using lines observed at high spectral resolution in each region to construct standard optical excitation diagnostic diagrams
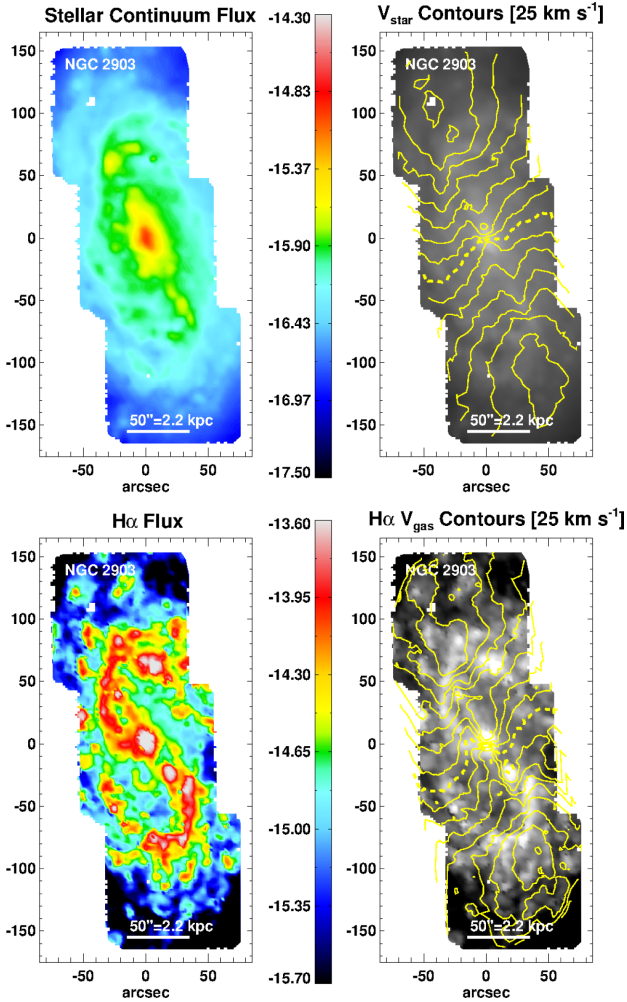
Figure 3. Example IFU-based data products for NGC 2903. From top to bottom, left to right: the optical stellar continuum [erg s^{-1} cm^{-2} Å^{-1}], stellar velocity field, extinction corrected Hα map [erg s^{-1} cm^{-2}], and Hα velocity field. The solid yellow isovelocity contours are in increments of 25 km s^{-1}, with the dashed yellow contour showing the systemic velocity where $v_{sys} = 0$ km s^{-1}. For the isovelocity contours, we use Voronoi binning for regions with low S/N, with a minimum of S/N $\geq$ 3 for Hα and a minimum S/N $\geq$ 50 for the stellar continuum.

(e.g. Baldwin, Phillips & Terlevich 1981; Veilleux & Osterbrock 1987; Kewley et al. 2001, 2006; Kewley & Dopita 2002; Rich et al. 2010), which can separate gas in different excitation conditions.

Common excitation diagnostic diagrams include plots of [O III]$\lambda\lambda$4959,5007/Hβ versus [S II]$\lambda\lambda$6717,6731/Hα, [O III]$\lambda\lambda$4959,5007/Hβ versus [N II]λ6584/Hα, and [O III]$\lambda\lambda$4959,5007/Hβ versus [O I]λ6300/Hα. For this work, we use the [O III]/Hβ versus [S II]/Hα diagnostic diagram (hereafter [S II] excitation diagnostic diagram) using spaxels where all the lines used have S/N > 5. In the [S II] excitation diagnostic diagrams seen on the far left-hand panel of Fig. 4, regions to the left of the SF threshold curve (middle black; Kewley et al. 2001) represent gas predominantly photoionized by massive stars, while regions to the right host gas predominantly excited by shocks or AGN. The latter regions are separated into Seyfert and LINERs via the blue diagonal line defined by Kewley et al. (2006). For local galaxies, shocked regions with velocities <500 km s^{-1} tends to have enhanced [N II]/Hα and [S II]/Hα and low [O III]/Hβ and these

regions are typically found in the LINER part of the excitation diagnostic diagrams (Farage et al. 2010; Rich, Kewley & Dopita 2011), while shocked gas with velocities >500 km s^{-1} and gas excited by a hard UV radiation field from an AGN tends to have high [O III]/Hβ, [N II]/Hα, and [S II]/Hα and fall in the Seyfert part of the diagram (Allen et al. 2008; Kewley et al. 2013).

Next we aim to map the spatial location of gas in different excitation phases in the galaxy. To do this, we first make a sliced excitation diagnostic diagram (far left-hand panel in Fig. 4) by dividing the excitation diagnostic diagram into six slices defined by five curves, based on the method by Davies et al. (2014). One of these curves is the SF threshold (middle black curve), while the other four curves are scaled upwards and downwards by 0.4 and 0.8 dex along the log([O III]/Hβ) axis. Spaxels between these curves are colour-coded based on how far they are above or below the SF threshold. Next, these colour-coded spaxels are over-plotted back on to the galaxy image to produce [S II] excitation maps (centre left-hand panel in Fig. 4). The term LINER stands for a low-ionization *nuclear* emission-line and it is conventionally assumed low luminosity AGN or central starbursts excite LINER conditions found near the centre of galaxies, while shocked gas such as in starburst-driven outflows can be found outside the nucleus. We find that in our seven spiral galaxies, LINER conditions exist well outside nuclear regions and are seen out to projected distances of several kpc (centre left-hand panel in Fig. 4). As we will show in Section 4.2, the extra-nuclear gas with LINER excitation characteristics often seem to be spatially associated with diffuse ionized gas.

Two of our sample galaxies, NGC 1068 and NGC 5194 (M 51a) are classified as having Seyfert 2 nuclei. In NGC 1068, which has an AGN-driven outflow (Antonucci & Miller 1985; Evans et al. 1991; Macchetto et al. 1994; Riffel et al. 2014), the [S II] excitation maps show Seyfert type conditions out to large projected distances of 7 kpc. NGC 5194 (M 51a) shows LINER like excitation in its centre (previously discussed in Blanc et al. 2009). Our data and a search through the literature shows no discernible evidence for AGN activity in any of the other galaxies.

4.2 Identifying and correcting for diffuse ionized gas

Diffuse ionized gas (DIG) consists of warm ($\sim$10^4 K) ionized gas that resides up to two kiloparsecs above and below the plane of a spiral galaxy's disc (Mathis 2000; Madsen, Reynolds & Haffner 2006; Haffner et al. 2009). This gas has been raised above the galactic disc by superbubbles created from regions in the disc where multiple supernovae have occurred and possibly by Type Ia supernovae at large scale heights (Wood et al. 2010). The DIG consists of the majority of ionized gas in a galaxy (Walterbos 1998), and its low level emission is a possible source of contamination superimposed over emission from H II regions ionized by photons from local massive stars in the disc. The low density, clumpy structure, and sufficient number of photons from hot OB stars in the galactic disc are enough to keep the DIG mostly ionized (Haffner et al. 2009), although shock ionization might also be a small secondary contributor (Martin 2000). The majority of the energy ionizing the DIG is currently thought to come from massive OB stars in the galactic disc from which ionizing Lyman continuum photons can travel large path lengths, up to several kpc above the disc, before ionizing the DIG (Walterbos 1998). Therefore the source of ionizing photons for the DIG is non-local. Current Z_{gas} diagnostics are calibrated to H II regions where the ionizing photons originate from local massive stars, but are not calibrated for DIG where the ionizing photons have a non-local origin. In order to avoid contamination by DIG, some IFU
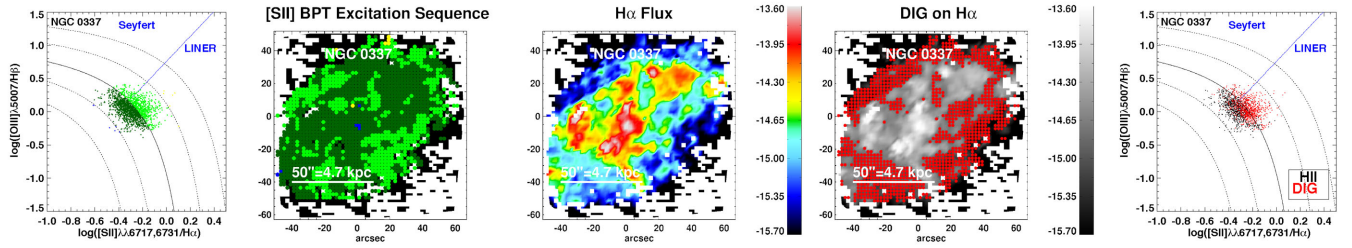
Figure 4. For NGC 0337 we show the following. Far left: the sliced [S II] excitation diagnostic diagram where the regions are plotted in different colours, according to their distance above or below the SF threshold curve (middle black curve) defined by Kewley et al. (2001) to separate regions dominated by massive SF from those dominated by shocks or AGN-excited gas. The diagram is divided into six slices defined by five curves based on the method by Davies et al. (2014). One of these curves is the SF threshold (middle black curve), while the other four curves are scaled upwards and downwards by 0.4 and 0.8 dex along the log([O III]/Hβ) axis (dotted curves). For regions above the SF threshold, the diagonal blue line separates the Seyfert and LINER regions based on prescriptions in Kewley et al. (2006). Centre left: the [S II] excitation map shows the spatial distribution of the colour-coded regions on the galaxy. Note that many of the green LINER-dominated regions lie in the outer parts of the galaxy. This is related to diffuse ionized gas, as we show in the centre right and far right-hand panels. Centre: for comparison, we show distribution of Hα flux which traces the current SF. Centre right: the diffuse ionized gas (DIG) dominated regions are over-plotted on the Hα map of the galaxy: they lie mostly in the outer parts of the galaxy, away from the spiral arms and regions of high SFR. Note that these DIG-dominated regions account for most of the puzzling LINER type regions present in the outer parts of the galaxies, as seen above. Far right: the [S II] excitation diagnostic diagram is shown with regions dominated by 100 per cent diffuse ionized gas (DIG) colour-coded as red. These regions tend to fall on the upper right diagram due to their high [S II]/Hα ratio.
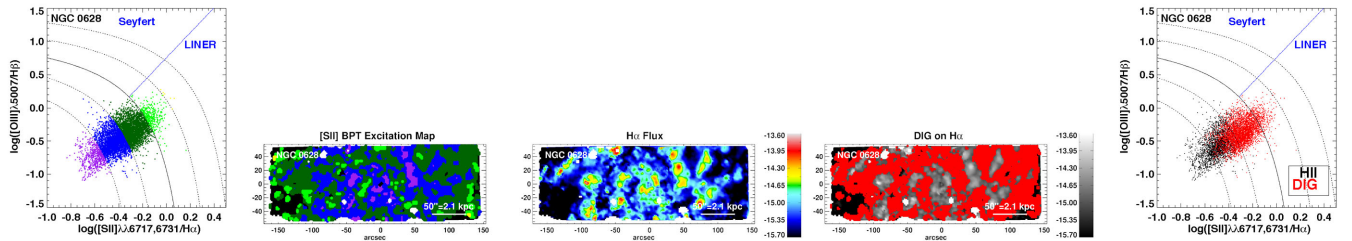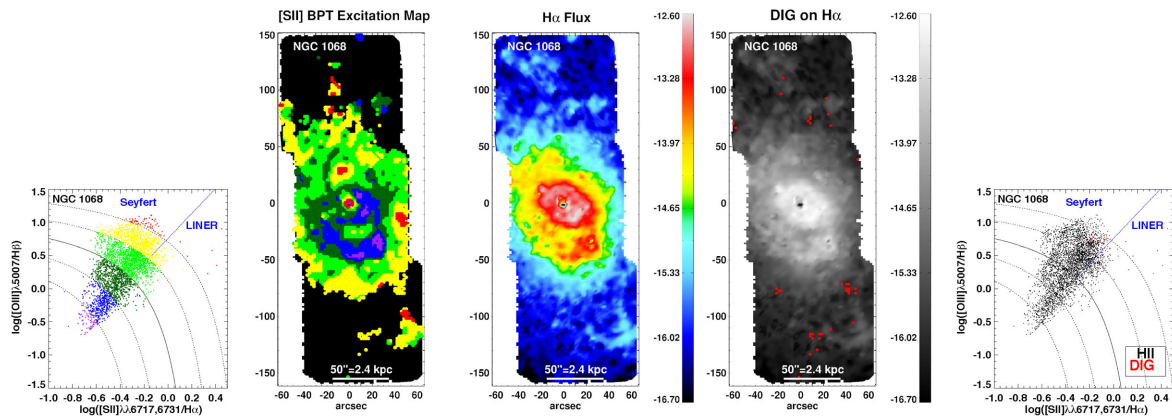

Figure 4 – *continued*: For NGC 0628.

Figure 4 – *continued*: For NGC 1068.

studies of Z_{gas} specifically target only bright H II regions (e.g. see Sánchez et al. 2012), thereby sacrificing spatial sampling. In this study, we try to identify and exclude regions dominated by DIG emission from our Z_{gas} analysis.

The contributions from H II regions and DIG for each individual emission line are hard to disentangle from each other, since we are seeing each galaxy in projection. The flux from an emission line measured in a single spaxel is integrated along the line of sight through the galaxy and will include some fraction of flux from H II regions and some fraction from DIG. We explore the contributions to the Hα flux by H II regions and DIG by expanding upon the

method developed in Blanc et al. (2009). For the Hα line, we call the fraction of flux coming from H II regions C_{HII} and the fraction of flux coming from DIG C_{DIG} such that the total Hα flux $f(H\alpha)$ is given by:

$$f(H\,\alpha) = f(H\,\alpha)_{HII} + f(H\alpha)_{DIG} \tag{1}$$

$$= C_{HII} f(H\alpha) + C_{DIG} f(H\alpha), \tag{2}$$

where $C_{HII} = 1 - C_{DIG}$.

The Wisconsin Hα Mapper (WHAM) sky survey (Madsen et al. 2006) observed DIG and H II regions in the Milky Way and found

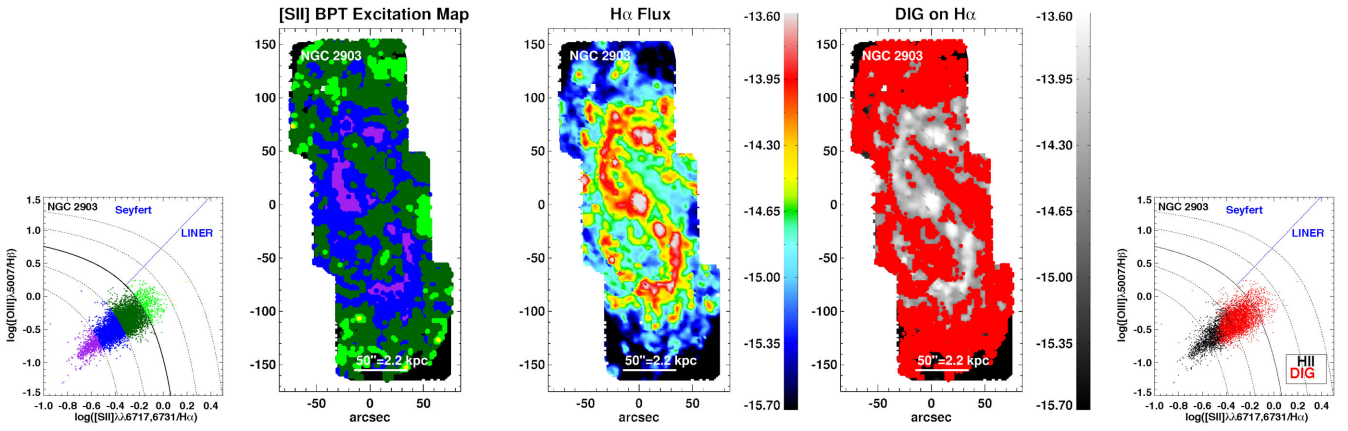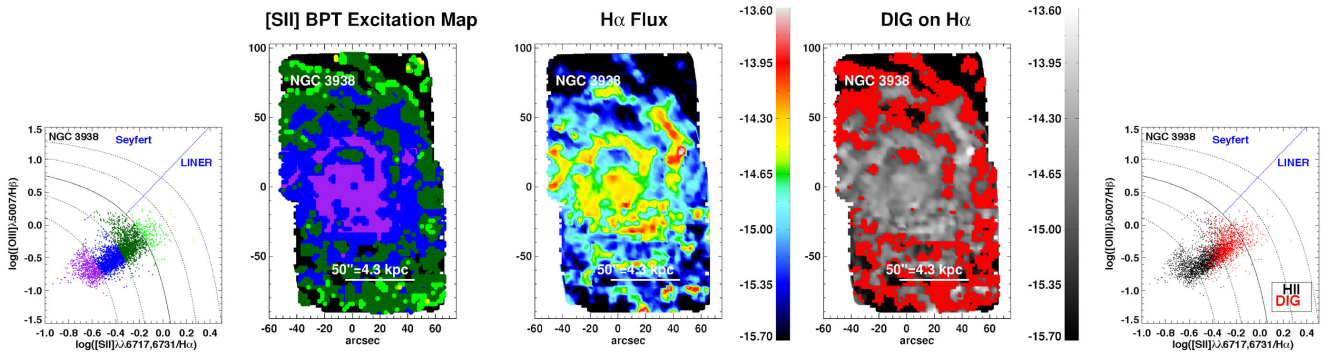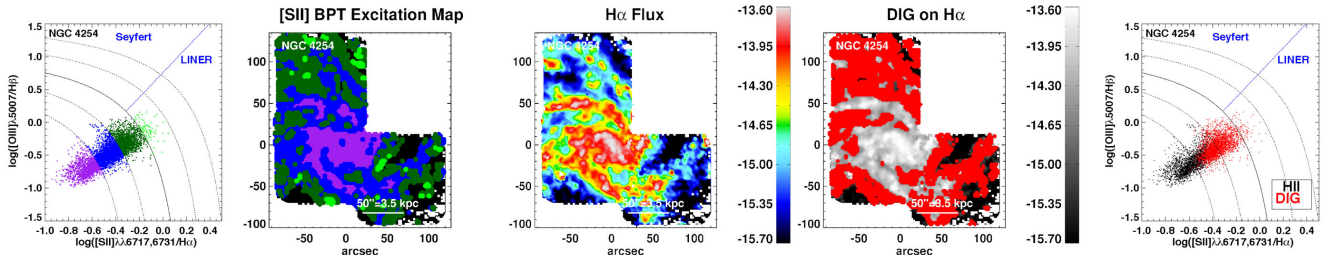**Figure 4** – *continued*: For NGC 2903.

Figure 4 – *continued*: For NGC 3938.

Figure 4 – *continued*: For NGC 4254.

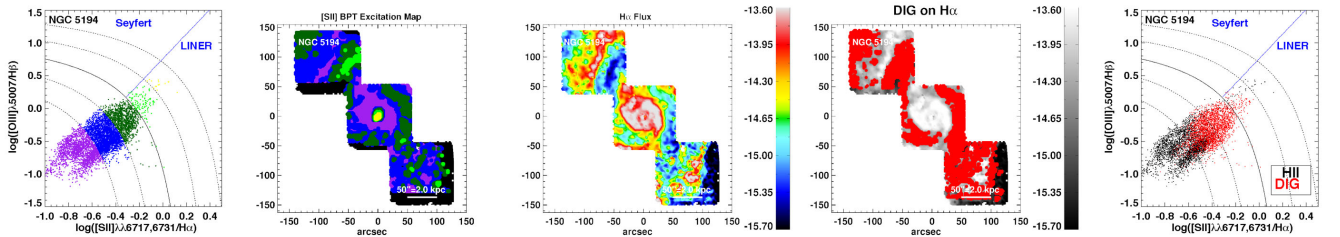**Figure 4** – *continued*: For NGC 5194.

that DIG has lower Hα surface brightness and higher [S II]/Hα than H II regions. The higher [S II]/Hα observed in DIG appears to mainly be caused by the higher temperatures found in DIG than in H II regions (Madsen et al. 2006; Haffner et al. 2009), but ionization effects might also play a role. In our work, we start by assuming H II regions dominate the observed areas of a galaxy with the highest

Hα flux, and DIG dominates the areas with the lowest. Using all spaxels where f(Hα) S/N > 3, we estimate the characteristic values of [S II]/Hα for H II regions ([S II]/Hα)$_{HII}$ and DIG ([S II]/Hα)$_{DIG}$ by finding the median [S II]/Hα in the 100 brightest and dimmest spaxels respectively. The value of [S II]/Hα in a given galaxy can be affected by several factors including variations in the ionization

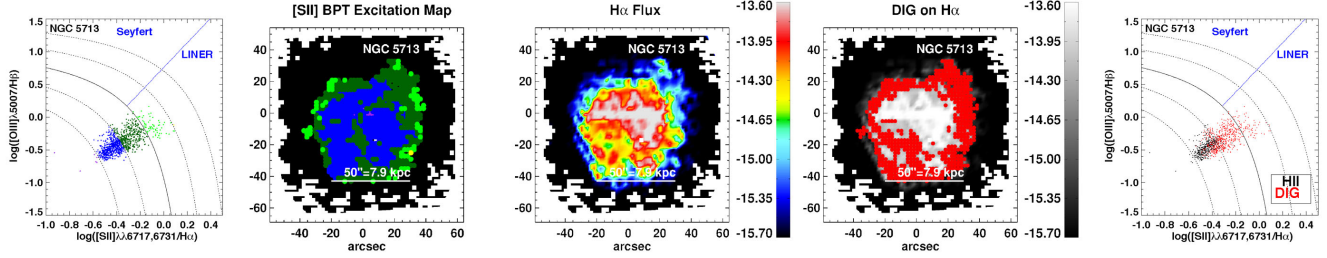**Figure 4** – *continued*: For NGC 5713.

parameter q, the hardness of the local radiation field and Z_{gas} (Diaz et al. 1991; Dors et al. 2011) so we calculate ([S II]/Hα)$_{\mathrm{H\,II}}$ and ([S II]/Hα)$_{\mathrm{DIG}}$ separately for each individual galaxy following the steps below.

Step 1: Obtain initial estimate for each spaxel's $C_{\mathrm{H\,II}}$. An initial estimate for each spaxel's $C_{\mathrm{H\,II}}$ is obtained from each spaxel's [S II]/Hα with the following equation:

$$\frac{[\text{S\,II}]}{\text{H}\alpha} = C_{\mathrm{H\,II}} \left(\frac{[\text{S\,II}]}{\text{H}\alpha} \right)_{\mathrm{H\,II}} + C_{\mathrm{DIG}} \left(\frac{[\text{S\,II}]}{\text{H}\alpha} \right)_{\mathrm{DIG}}, \qquad (3)$$

and solving for our initial guess of $C_{\mathrm{H\,II}}$:

$$C_{\mathrm{H\,II}} = \frac{\frac{[\text{S\,II}]}{\text{H}\alpha} - \left(\frac{[\text{S\,II}]}{\text{H}\alpha} \right)_{\mathrm{DIG}}}{\left(\frac{[\text{S\,II}]}{\text{H}\alpha} \right)_{\mathrm{H\,II}} - \left(\frac{[\text{S\,II}]}{\text{H}\alpha} \right)_{\mathrm{DIG}}}. \qquad (4)$$

Step 2: Solve for one value of f_0 and β for each galaxy. Next we use our initial estimate for $C_{\mathrm{H\,II}}$ and $f(\mathrm{H}\alpha)$ for all the individual spaxels to find one value of Hα flux f_0 for a given galaxy where we assume 100 per cent of the flux comes from DIG. This procedure is illustrated in Fig. 5. We solve for f_0 by fitting a single curve to the following equation:

$$C_{\mathrm{H\,II}} = 1.0 - \left(\frac{f_0}{f(\mathrm{H}\alpha)} \right)^{\beta}; \quad (\text{for } f(\mathrm{H}\alpha) > f_0), \qquad (5)$$

weighting the fit by the uncertainty in [S II]/Hα. Variation in DIG surface brightness is accounted for with the exponent β, where the DIG would have a constant surface brightness across the disc of a galaxy at $\beta = 1$, and tracks the distribution of SF in the disc at $\beta < 1$. We report the values found for f_0 and β for each galaxy in Table 3.

Step 3: Solve for a final $C_{\mathrm{H\,II}}$ for each spaxel where $f(\mathrm{H}\alpha) > f_0$: Once we solve for f_0 and β, we reuse equation (5) and each spaxel's $f(\mathrm{H}\alpha)$ to solve for a final $C_{\mathrm{H\,II}}$ for each spaxel where $f(\mathrm{H}\alpha) > f_0$. Any spaxels where $f(\mathrm{H}\alpha) \leq f_0$ are considered to have 100 per cent contribution from the DIG to $f(\mathrm{H}\alpha)$. From here, $C_{\mathrm{H\,II}}$ serves two functions, it acts as a correction for $f(\mathrm{H}\alpha)$ such that the Hα flux coming from H II regions is $f(\mathrm{H}\alpha)_{\mathrm{H\,II}} = C_{\mathrm{H\,II}} f(\mathrm{H}\alpha)$, and it allows us to identify and exclude DIG contaminated spaxels from our Z_{gas} analysis. For this study we exclude spaxels where DIG takes up 40 per cent or more of $f(\mathrm{H}\alpha)$, so we only include spaxels where $C_{\mathrm{H\,II}} > 0.6$.

For each galaxy, the far right-hand panel of Fig. 4 illustrates the location of the DIG on the excitation diagnostic diagram, while the centre right-hand panel of Fig. 4 shows the projected spatial distribution of DIG in the galaxy. Most of the DIG-dominated regions occupy the mid-to-upper right side of the excitation diagnostic diagram. This behaviour is expected since high [N II]/Hα and [S II]/Hα line ratios are associated with DIG emission. Within the galaxies, most of the DIG-dominated emission is located at large projected distances from the centre of the galaxy and is often associated with

the regions between the spiral arms. A comparison of the centre left and centre right-hand panels of Fig. 4 shows that many of the LINER-type regions, which are located in the outer regions of galaxies and are far from spiral arms or other sites of high SFRs, tend to be spatially associated with DIG. This effect has also been observed by Greenawalt, Walterbos & Braun (1997), Hoopes & Walterbos (2003), Singh et al. (2013), and Belfiore et al. (2015).

In NGC 2903 we calculate the effect of erroneously including DIG when calculating Z_{gas}. We find that including the DIG-dominated regions only changes the average absolute value of Z_{gas} for all our diagnostics by at most ± 0.1 dex and the slope of the Z_{gas} gradients by ± 0.015 dex kpc^{-1}, even in the outer regions of the disc where emission is the most dominated by the DIG. The uncertainty of 0.1 dex is about the same as the uncertainty found when the T_e method is used to estimate Z_{gas} (Kennicutt, Bresolin & Garnett 2003; Hägele et al. 2008). While this is a small effect in NGC 2903, for accuracy we remove all DIG-dominated regions where $C_{\mathrm{H\,II}} \leq 0.6$ when calculating Z_{gas} in our sub-sample galaxies.

4.3 Computing star formation rates

We can estimate the current star formation rate (SFR) by measuring the intensity of recombination lines such as Hα. UV photons bluewards of the Lyman break ionize neutral atomic hydrogen and when ionized hydrogen recombines, part of that energy is radiated away as recombination lines such as Hα (Kennicutt 1998). Our IFU data include readily available spatially resolved Hα emission from which we can compute SFRs. Hα derived SFRs can be used in IFU studies to directly compare against different parameters (e.g. Z_{gas}, q, or gas excitation) and environments in a galaxy, be combined with multiwavelength data to study SF laws and efficiency (Blanc et al. 2009, 2013b), and be tested against other SFR diagnostics (Catalán-Torrecilla et al. 2015). Before any SFR can be measured, we correct the Hα flux for extinction using the Hα/Hβ = 2.86 line ratio decrement described in Osterbrock & Ferland (2006). We apply a reddening correction using a Milky Way like extinction curve, typically of $E(B - V) \sim 0.5$ although the reddening correction can range anywhere from $E(B - V) = 0$ to 2. Contaminated regions such as Seyfert and LINER are masked out, as described in Section 4.1. We correct for the DIG contribution to the Hα flux $f(\mathrm{H}\alpha)$ by multiplying it by the value of $C_{\mathrm{H\,II}}$ calculated in Section 4.2. While DIG contamination affects the local SFR measured in a given spaxel, the total SFR across an entire galaxy includes emission from the DIG since the photons ionizing the DIG originated from hot massive young stars. To account for this, we scale the DIG corrected SFR in each spaxel by dividing by the ratio of the total $f(\mathrm{H}\alpha)$ from H II regions to the total $f(\mathrm{H}\alpha)$ across the galaxy $(\sum C_{\mathrm{H\,II}} f(\mathrm{H}\alpha))/(\sum f(\mathrm{H}\alpha))$. The SFR for a given spaxel is calculated
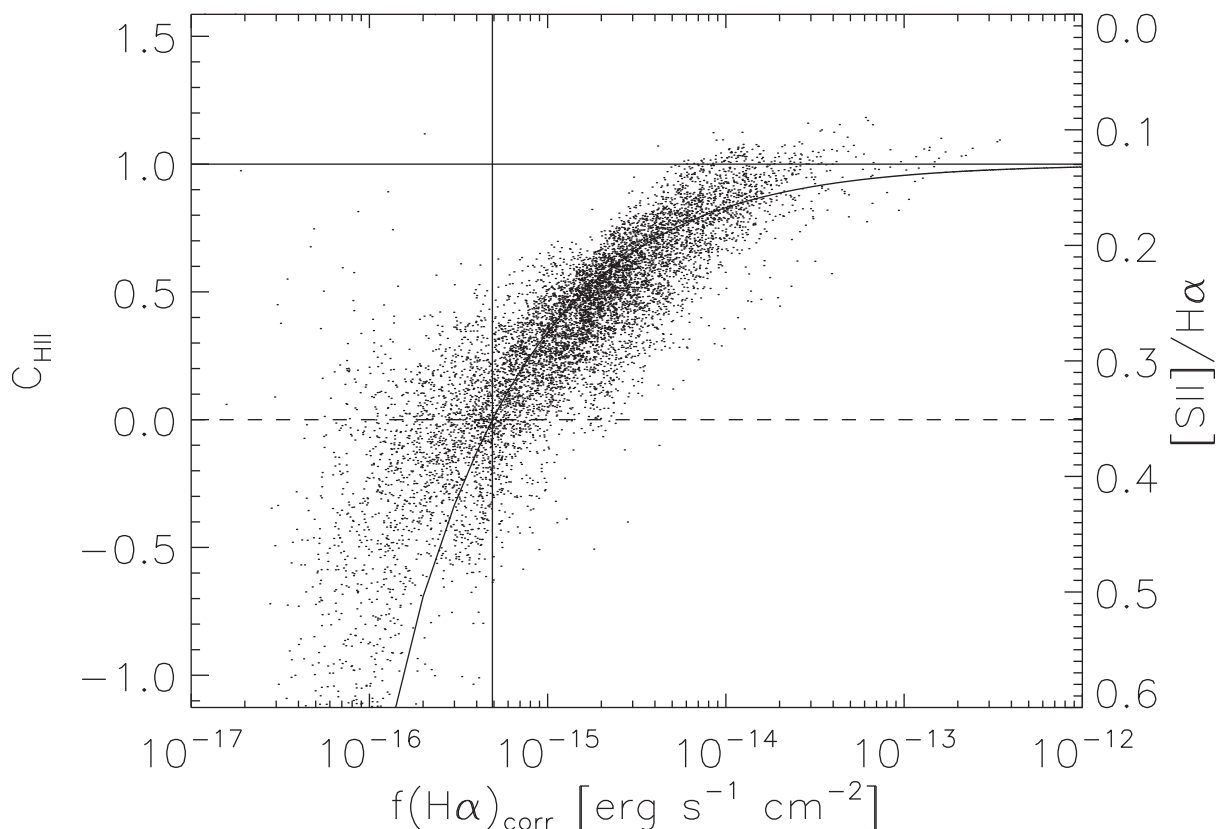
Figure 5. How we identify diffuse ionized gas (DIG) in a galaxy's spaxels as described in Section 4.2 and building upon the methodology and fig. 9 from Blanc et al. (2009). Each data point represents an individual spaxel from NGC 2903. The x-axis is $f(H\alpha)_{corr}$, the extinction corrected flux of Hα per spaxel. The right y-axis is the [S II]/Hα ratio per spaxel. The horizontal solid line represents the median [S II]/Hα of the 100 brightest spaxels ([S II]/Hα)$_{H II}$, where we assume nearly all the flux is coming from gas in H II regions excited by star formation. The dashed horizontal line represents the median [S II]/Hα of the 100 dimmest spaxels with sufficient signal-to-noise ([S II]/Hα)$_{DIG}$, where we assume 100 per cent of the flux comes from the DIG. We make an initial guess for each spaxel of $C_{H II}$, the fraction of $f(H\alpha)_{corr}$ coming from star formation, from each spaxel's [S II]/Hα value, ([S II]/Hα)$_{H II}$, and ([S II]/Hα)$_{DIG}$ as shown on the left y-axis. From each spaxel's $f(H\alpha)_{corr}$ and the initial guess of $C_{H II}$, we fit equation (5) (solid curved line) to find the final estimate of $C_{H II}$ for each spaxel and f_0, the flux where we assume 100 per cent of the emission is from the DIG marked with the vertical solid line.

Table 3. Star formation rates.

Galaxy	$M_\star$	$f_{R_{25}}$	R_{vp} (kpc)	R_{25} (kpc)	f_0 (erg s^{-1} cm^{-2})	β	VENGA SFR(Hα) (M$_\odot$ yr^{-1})	Global TIR Lum. (erg s^{-1})	Global SFR(TIR) (M$_\odot$ yr^{-1})
(1)	(2)	(3)	(4)	(5)	(6)	(7)	(8)	(9)	(10)
NGC 0337	1.6E+10	0.72	5.8	8.1	5.74E-16	0.772	1.52	4.88E+43	1.90
NGC 0628	2.0E+10	0.47	6.2	13.1	2.52E-16	0.789	0.50	3.80E+43	1.48
NGC 2903	5.0E+10	0.38	6.2	16.3	4.90E-16	0.587	1.48	7.73E+43	3.01
NGC 3938	3.2E+10	0.60	8.4	14.0	3.53E-16	0.891	1.75	6.10E+43	2.37
NGC 4254	4.0E+11	0.81	9.0	11.1	5.74E-16	0.637	4.11	1.30E+44	5.06
NGC 5194	7.9E+10	0.56	7.7	13.8	8.68E-17	0.804	2.27	1.05E+44	4.08
NGC 5713	7.9E+10	0.66	8.6	13.0	1.47E-15	0.653	9.50	3.02E+44	11.76

Columns: (1) Galaxy NGC number. (2) Total stellar mass in units of M$_\odot$ from Blanc et al. (2013a). (3) Fraction of R_{25} radius covered, as illustrated in Fig. 1. (4) Projected radius of galaxy covered by our Mitchell Spectrograph IFU data in kpc. (5) The galaxy's projected radius R_{25} from RC3 (de Vaucouleurs et al. 1991). R_{25} is defined as the radius where the surface brightness of the outer disc reaches 25 mag arcsec^{-2} in the B-band. (6) f_0 is the Hα flux per spaxel in units of erg s^{-1} cm^{-2} where we assume 100 per cent of the emission is from the DIG. See equation (5) in Section 4.2. (7) β quantifies variation in DIG surface brightness across a galaxy's disc. The DIG would have a constant surface brightness across the disc of a galaxy at $\beta = 1$, and tracks the distribution of SF in the disc at $\beta < 1$. See equation (5) in Section 4.2. (8) Extinction corrected Hα-based SFRs (M$_\odot$ yr^{-1}) measured from integrated Hα flux over the regions covered by our pointings of the Mitchell Spectrograph. See Section 4.3 for details. (9) TIR luminosity, in units of solar luminosity, calculated from the IRAS 25, 60 and 100 μm bands. See Section 4.3 for details. (10) TIR-based SFR (M$_\odot$ yr^{-1}) calculated from the TIR luminosity. See Section 4.3 for details.

from the flux of the Hα line using the prescription from Kennicutt & Evans (2012):

$$\text{SFR (M}_\odot \text{ yr}^{-1}) = \frac{5.37 \times 10^{-42} \, C_{H II} \, f(H\alpha)}{\left(\sum C_{H II} f(H\alpha)\right) / \left(\sum f(H\alpha)\right)}, \quad (6)$$

where $f(H\alpha)$ is in units of erg s^{-1}. We convert the SFR for each individual spaxel into a SFR density (Σ_{SFR} M$_\odot$ yr^{-1} kpc^{-2}) by dividing the SFR for each spaxel by its deprojected area in kpc^2. Table 3 lists the total integrated SFR over our spatial coverage for
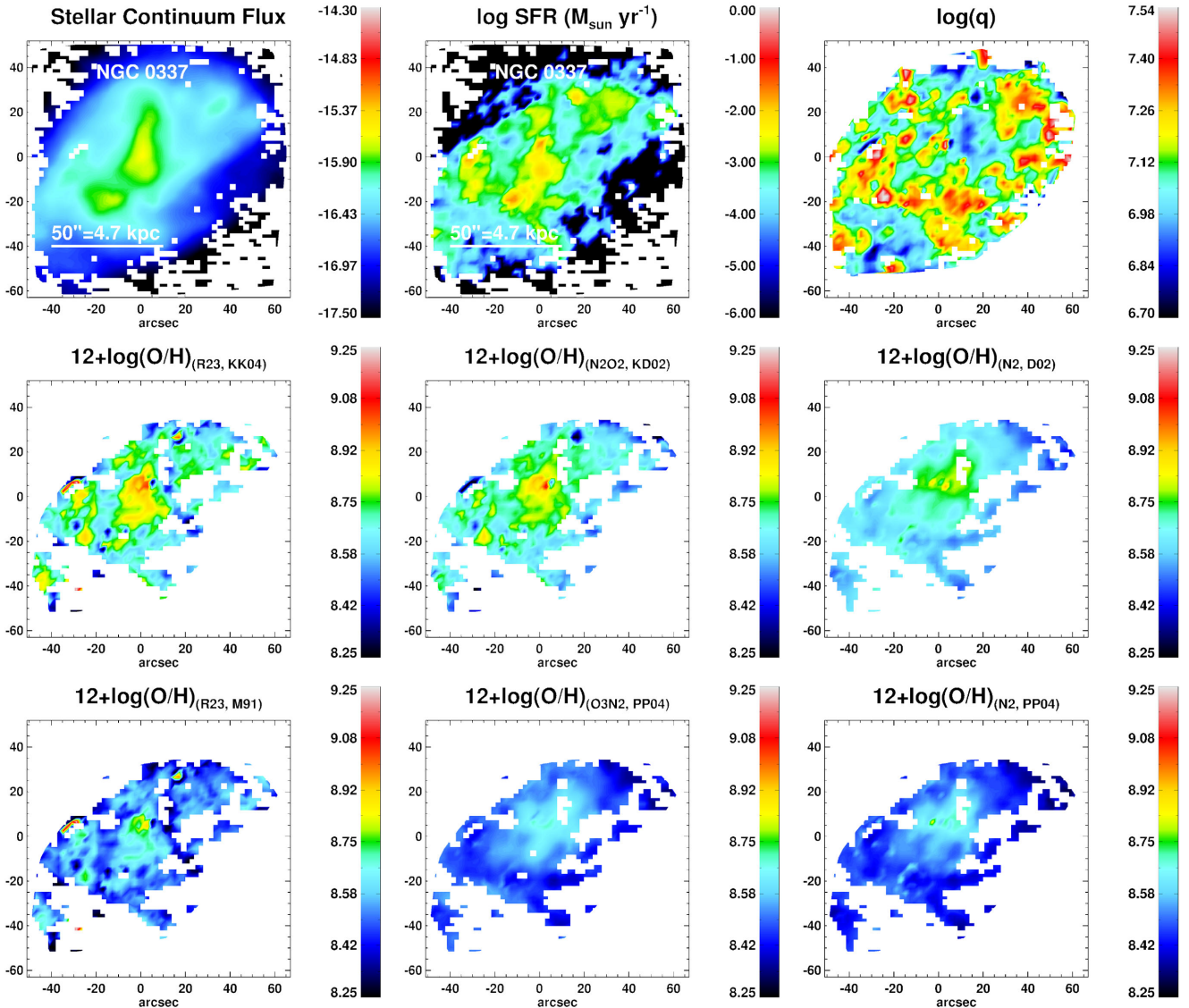
Figure 6. For NGC 0337, we show the following from left to right.Top row: bolometric stellar flux in units of erg s^{-1} cm^{-2} Å^{-1}; SFR in units of M$_\odot$ yr^{-1} derived from extinction corrected Hα flux using the calibration from Kennicutt & Evans (2012); ionization parameter q in units of the cm s^{-1} calculated as described in Section 4.4. Middle and bottom row: gas phase metallicity Z_{gas}, or log(O/H)+12, based on six different Z_{gas} diagnostics R_{23}-KK04, N2O2-KD02, N2-DO2, R_{23}-M91, O3N2-PP04, N2-PP04.

each galaxy. Maps of Σ_{SFR} can be seen in Fig. 6 and radial gradients for Σ_{SFR} are shown on the right side of Fig. 7.

To assess the robustness of our SFR estimates, we compare the extinction corrected Hα SFRs from our IFU data to the SFRs inferred from the global total infrared (TIR) luminosity between 3–1100 μm. Infrared derived SFRs avoid the issues of extinction or contamination (ie. from shocks) that can affect Hα derived SFR estimates. Fluxes from the 25, 60, and 100 μm *IRAS* bands are obtained from the *IRAS* Revised Bright Galaxy Sample (Sanders et al. 2003). The *IRAS* fluxes are converted into luminosities given the distance to each galaxy, and then into a global TIR luminosity using equation (5) from Dale & Helou (2002). TIR SFRs are computed using the TIR SFR calibration from Kennicutt & Evans (2012). The global TIR luminosities and SFRs we calculate for our galaxies can be seen in Table 3. Although our IFU data only cover a fraction of the disc's R_{25} radius (see Table 1), our extinction corrected Hα based

SFR from VENGA is a large fraction (34–81 per cent) of the global SFR$_{TIR}$. This is reasonable because most of the obscured SF in a galaxy (as traced by TIR light) takes place in the central regions of a galaxy.

4.4 Computing the ionization parameter q

Kewley & Dopita (2002) define an effective ionization parameter q as the flux of ionizing photons above the Lyman limit (energy >13.6 eV) through the surface of a Strömgren sphere of radius R divided by the electron density n:

$$q \text{ (cm s}^{-1}) = \frac{Q}{4\pi R^2 n} \qquad (7)$$

where Q is the flux of ionizing photons produced at the surface of the central star(s). The ionization parameter q for a given spaxel is set by
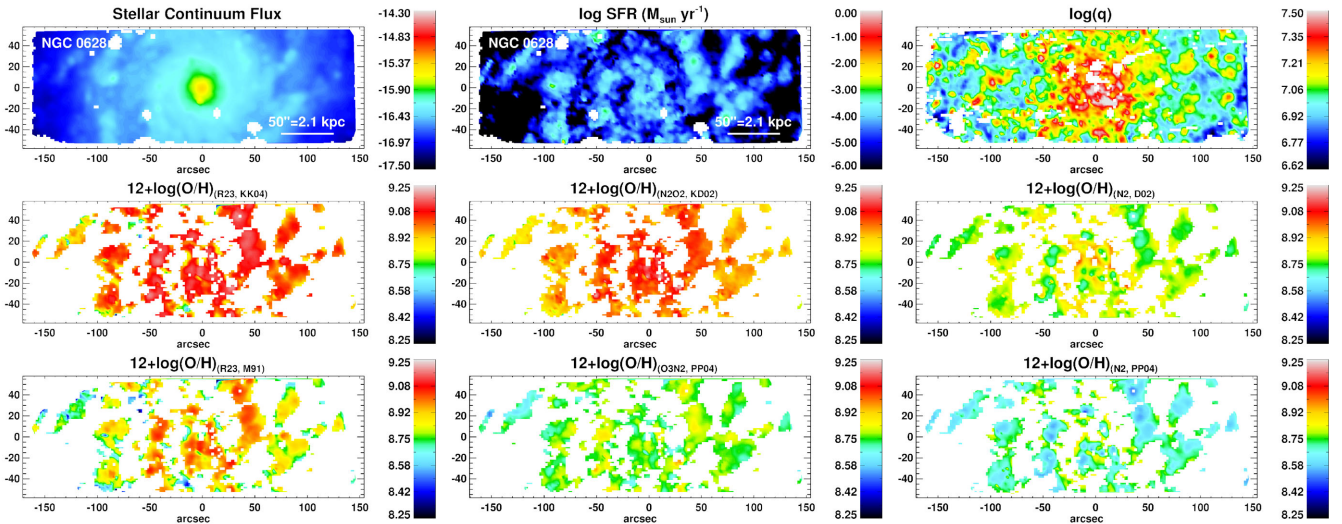
Figure 6 – *continued*: For NGC 0628.

the mass, metallicity, and age of the stellar populations that make up the local ionizing sources and the structure, geometry, metallicity, and dust content of the illuminated gas. There is a known inverse correlation between q and Z_{gas} (Freitas-Lemes et al. 2014; Pérez-Montero 2014; Rosa et al. 2014) which is hypothesized to arise from the Z_{gas} tracing the metallicity of the underlying stellar popluations (Dors et al. 2011; Sánchez et al. 2015). For each spaxel consistent with photoionization primarily by massive stars, we calculate q with several goals in mind: (a) We wish to explore how q varies across regions which have different SFR densities (see Section 5.1 and Fig. 6); (b) We need to know q because several of the Z_{gas} diagnostics we use (listed in Table 4) attempt to correct for variations in q; (c) We wish to compare to Z_{gas} diagnostics that do not explicitly include q (see Table 4) and explore their *relative* radial trends.

In the first method we use to calculate q, we start by deriving Z_{gas} from the diagnostic based on the [N II]/[O II] ratio (Kewley & Dopita 2002), which is fairly invariant to the value of q (bottom left-hand panel of Fig. 8) due to the similar ionization potentials of N^{+} and O^{+}. Once we have Z_{gas}, we use the line ratio [O III]/[O II] to calculate q, using the fact that this ratio depends heavily on q (bottom right-hand panel of Fig. 8). Specifically, we derive q by placing Z_{gas} and [O III]/[O II] into the following equations from Kobulnicky & Kewley (2004):

$$y = \log\left(\frac{[\text{O III}]}{[\text{O II}]}\right) \tag{8}$$

$$Z_{gas} = \log(\text{O/H}) + 12 \tag{9}$$

$$\log q = 32.81 - 1.153y^2$$
$$+ Z_{gas}(-3.396 - 0.025y + 0.1444y^2)/$$
$$[4.603 - 0.3119y - 0.163y^2$$
$$+ Z_{gas}(-0.48 + 0.0271y + 0.02037y^2)] \tag{10}$$

We discuss an alternative method for finding q in Appendix A. That method gets q from the [O III]/[O II] line ratio, but it solves iteratively for Z_{gas} and q, to ensure they are consistent with multiple line ratios such as [O III]/[O II], [N II]/[O II], and R_{23} (Fig. 8). Both methods give similar results for q.

4.5 Computation of Z_{gas} using different diagnostics

The most direct method for computing Z_{gas} from emission line fluxes involves measuring the electron temperature (T_e) from the flux ratio of the [O III] lines: [O III]$\lambda 4363$ to [O III]$\lambda\lambda 4959,5007$. By placing the measured value of T_e into a classical H II region model, one finds Z_{gas} (Osterbrock & Ferland 2006). Our VENGA observations do not go deep enough to detect the emission of the [O III]$\lambda 4363$ line with high enough S/N to use the direct T_e method. Instead, taking advantage of the broad wavelength coverage (3600–6800 Å) and ~120 km s^{-1} spectral resolution of the VENGA IFU data, we use several stronger detectable emission lines ([O II], [O III], Hβ, Hα, [N II]) to compute four different widely used Z_{gas} indicators (R_{23}, N2O2, N2, O3N2), which are defined, respectively, by the line ratios $R_{23} \equiv$ ([O II]$\lambda 3727$+[O III]$\lambda\lambda 4959,5007$)/Hβ, N2O2 $\equiv$ [N II]$\lambda 6584$/[O II]$\lambda 3727$, N2 $\equiv$ [N II]$\lambda 6584$/Hα, and O3N2 $\equiv$ ([O III]$\lambda\lambda 4959,5007$/Hβ)/([N II]$\lambda 6584$/Hα) (Table 4).

It is extremely important to have multiple Z_{gas} indicators in order to break degeneracies and explore the systematics between indicators. Different methods to determine Z_{gas} may differ from each other by up to 0.7 dex (Kewley & Ellison 2008; López-Sánchez et al. 2012; Blanc et al. 2015). The variation of R_{23} with Z_{gas} and q is shown in the top left of Fig. 8. It can also be seen that for moderate to high values of R_{23}, we have a degeneracy with two possible ranges of Z_{gas} for every R_{23} value at fixed q. We call these ranges the low and high branches of Z_{gas} for R_{23} (Kewley & Dopita 2002; Kobulnicky & Kewley 2004). H II regions have temperatures typically around 10^4 K, so are hot enough to collisionally excite the forbidden [O II] and [O III] transitions. On the lower branch of Z_{gas} where R_{23} rises with Z_{gas} at a given q, the main coolant is oxygen and the strength of the [O II] and [O III] lines increases with oxygen abundance. On the higher branch of Z_{gas}, R_{23} falls with Z_{gas} at a given q because at high Z_{gas}, cooling is dominated by far-IR fine structure metal lines and the electron temperature becomes too low to collisionally excite the [O II] and [O III] lines (Pagel et al. 1979). Adding in other line ratios can help solve for q and break Z_{gas} degeneracies. The [O III]/[O II] line ratio depends heavily on q (bottom right-hand panel of Fig. 8) due to the different ionization potentials of O^+ and O^{++}, while the N2O2 indicator ([N II]/[O II] line ratio) does not depend strongly on q and maps monotonically on to
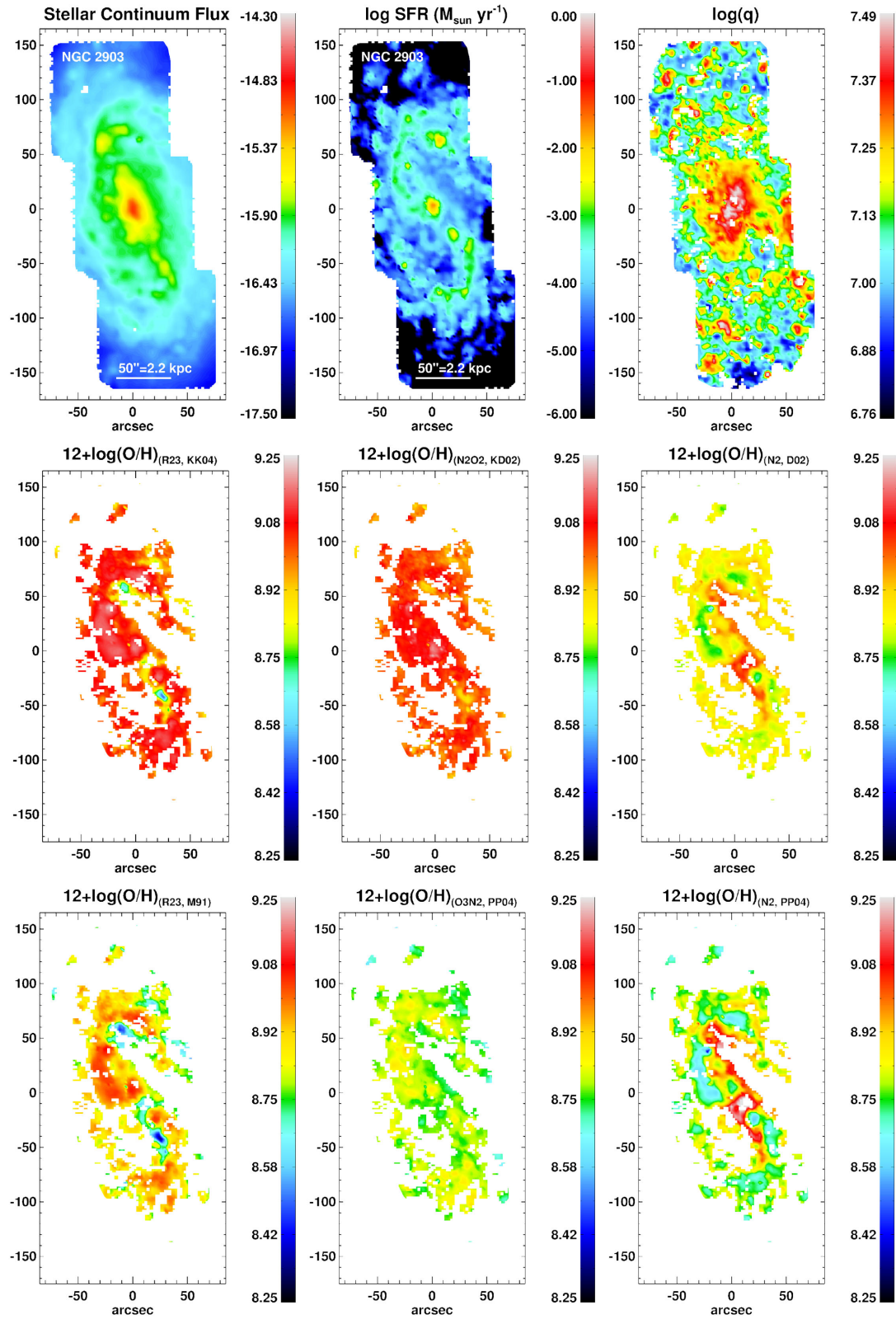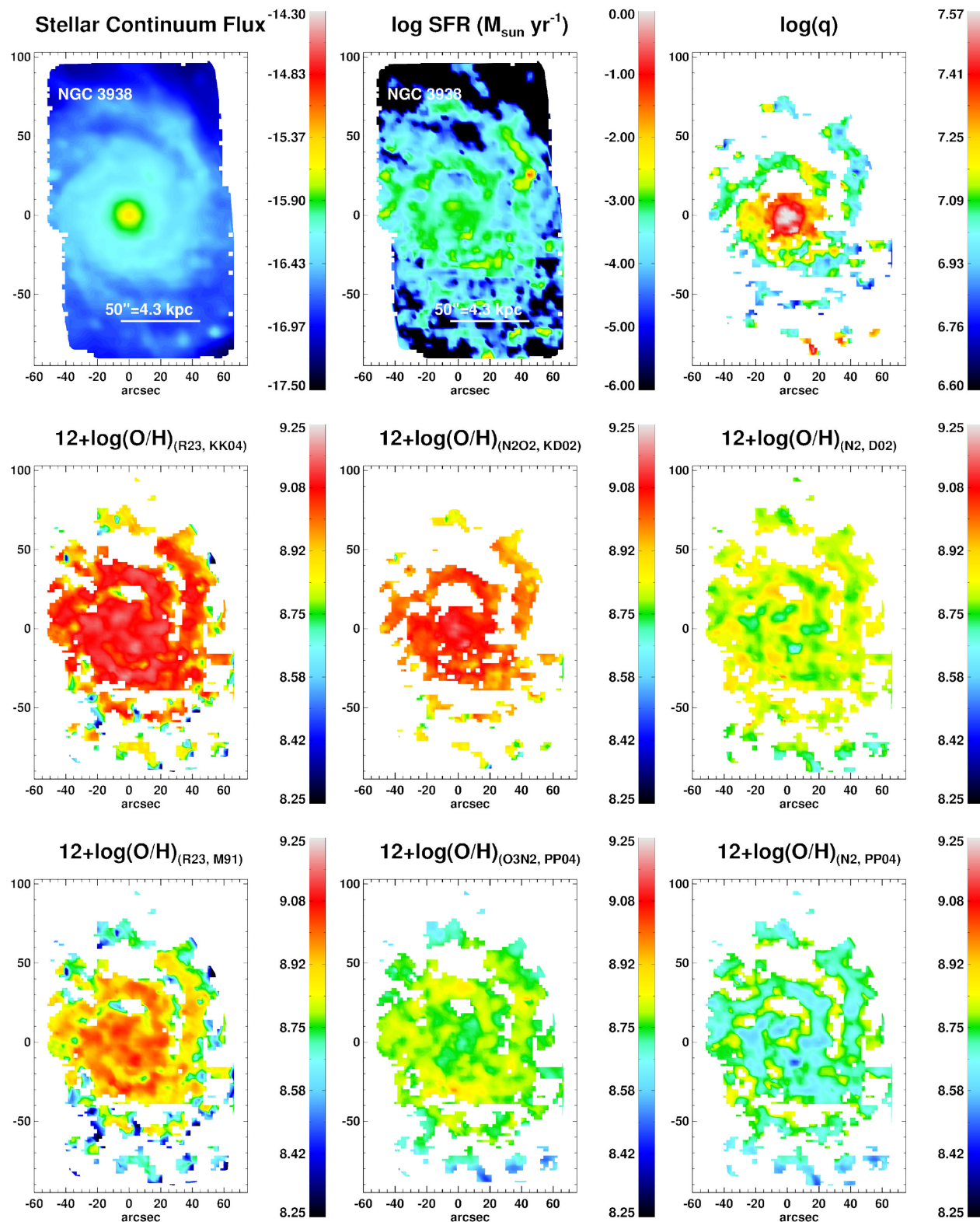
Figure 6 – *continued*: For NGC 2903.

Figure 6 – *continued*: For NGC 3938.

Z_{gas} (bottom left-hand panel of Fig. 8) due to the similar ionization potentials of N^+ and O^+.

For our study, we do not build our own empirical or theoretical Z_{gas} diagnostics, but instead use seven of the eight published Z_{gas} diagnostics detailed in Kewley & Ellison (2008) based on the four

Z_{gas} indicators (R_{23}, N2O2, N2, O3N2) to derive Z_{gas} in our targets: R_{23}-M91 (McGaugh 1991), R_{23}-KK04 (Kobulnicky & Kewley 2004), R_{23}-Z94 (Zaritsky et al. 1994), N2O2-KD02 (Kewley & Dopita 2002), N2-D02 (Denicoló et al. 2002), N2-PP04 (Pettini & Pagel 2004), and O3N2-PP04 (Pettini & Pagel 2004) (see list of Z_{gas}
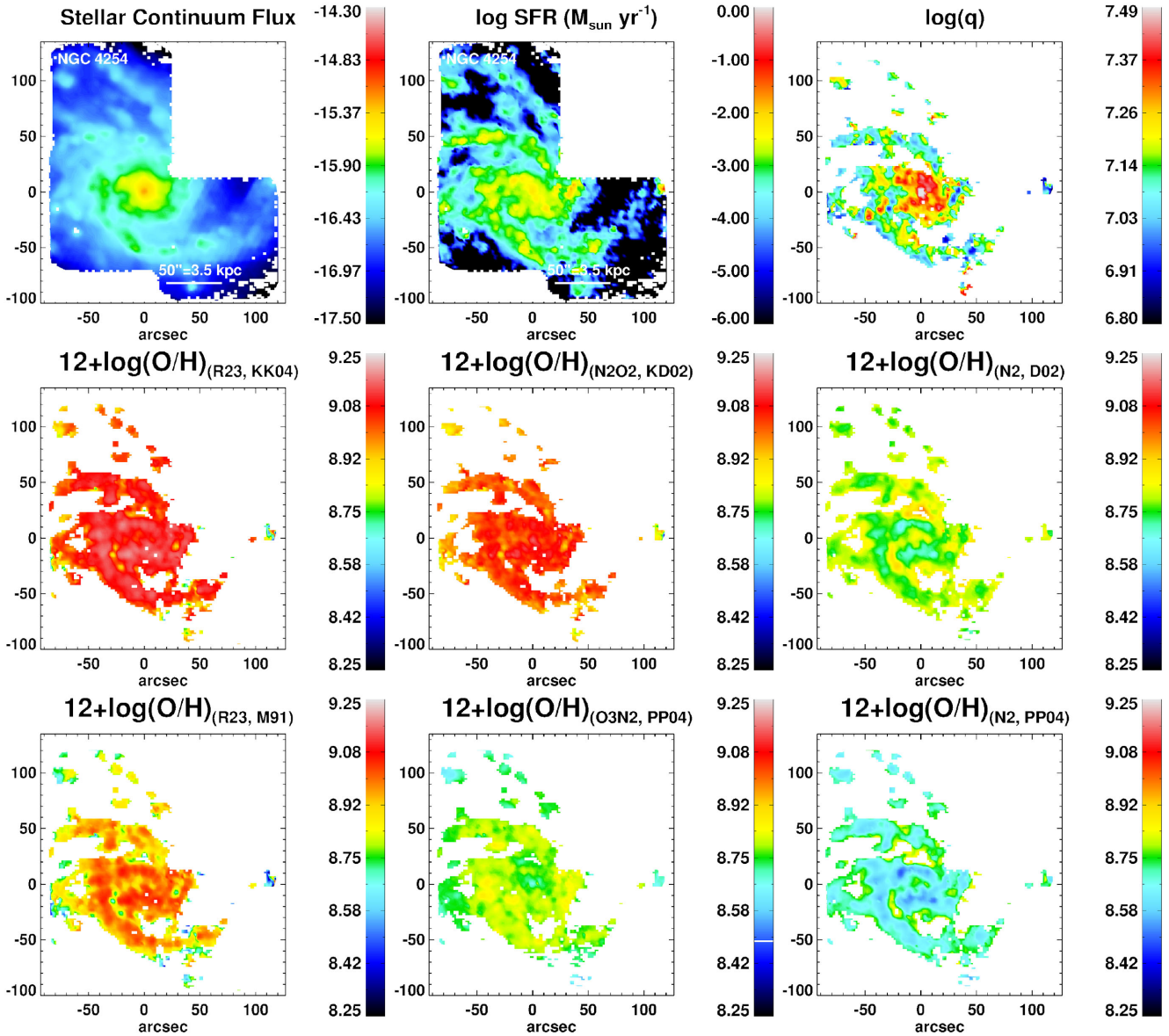
Figure 6 – *continued*: For NGC 4254.

diagnostics in Table 4). We do not use R_{23}-P05 (Pilyugin & Thuan 2005) due to its large systematic offset from the other diagnostics.

Different Z_{gas} diagnostics using the same Z_{gas} indicator can yield different metallicities due to the different theoretical and empirical calibrations and corrections for variations in the ionization parameter q (see Appendix B). For instance, R_{23}-M91 and R_{23}-KK04 both correct for variations in q, but correct for q via two different methods (outlined in Section 4.4), while the R_{23}-Z94 diagnostic does not correct for q. Another difference is that some Z_{gas} calibrations we use are 'empirical' and others are 'theoretical'. Empirical calibrations involve calibrating the strong emission line ratios observed in H II regions to the Z_{gas} derived from the direct T_e method. Theoretical Z_{gas} calibrations base their line ratios on models of stellar populations, radiative transfer, and nebular photoionization (Dopita et al. 2000; Kewley & Dopita 2002).

We compute the full suite of seven Z_{gas} diagnostics from our VENGA data. We start by making a signal-to-noise cut of

S/N > 5 for the Balmer decrement line ratio (Hα/Hβ = 2.86) to ensure we have a reliable extinction correction, and S/N > 3 for all the emission line fluxes used in each Z_{gas} diagnostic. We exclude all regions that are LINER or Seyfert on the excitation diagnostic diagrams (Section 4.1), along with all regions flagged as DIG-dominated (Section 4.2), and only use regions where the gas is primarily photoionized by massive stars from recent SF. For each spaxel, we compute the line ratios for the four indicators (R_{23}, N2O2, N2, O3N2) and then apply the different calibrations to derive the seven Z_{gas} diagnostics (Table 4), following the steps detailed in Kewley & Ellison (2008) and Appendix B. This is possible for seven (NGC 0337, 0628, 2903, 3938, 4254, 5194, and 5713) of the eight galaxies in our sample. The rejected galaxy, NGC 1068, is classified as a Seyfert 2 AGN and most of the spaxels in both the nuclear regions and extended disc show Seyfert type excitation conditions (as seen in Fig. 4) so we remove this galaxy from further Z_{gas} analysis.
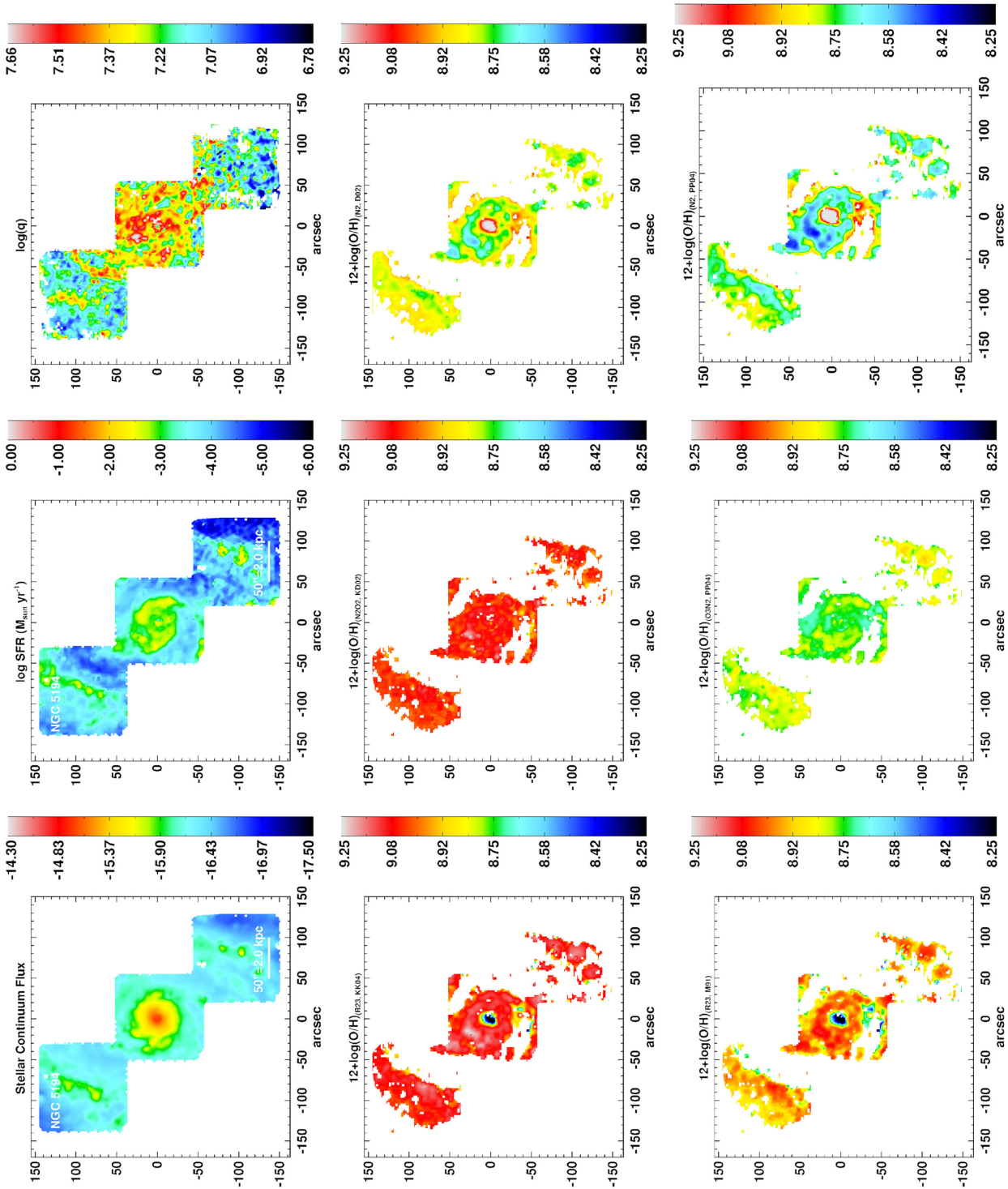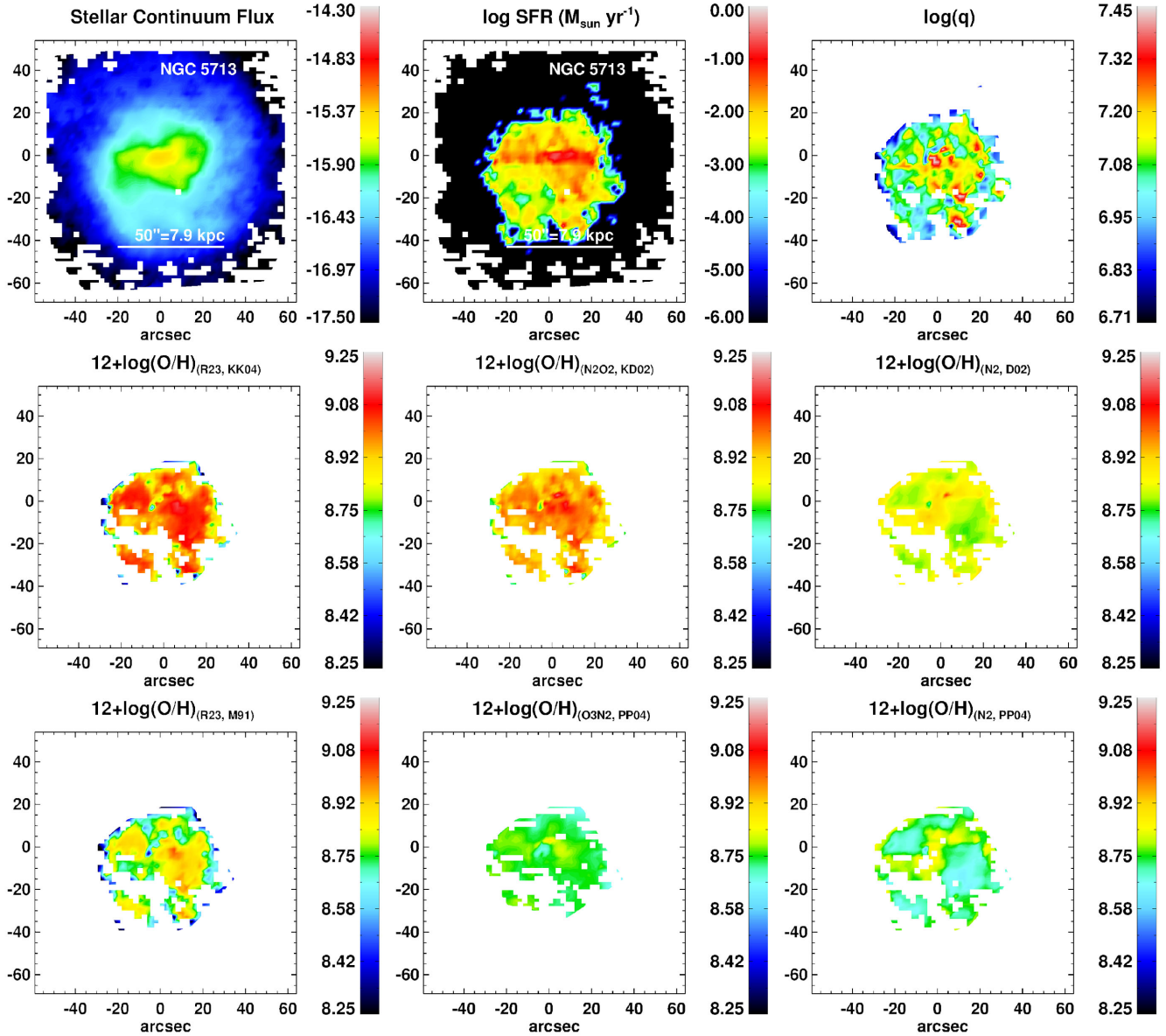
Figure 6 – *continued*: For NGC 5194.

Figure 6 – *continued*: For NGC 5713.

5 RESULTS AND DISCUSSION

5.1 2D maps of SFR, *q*, and Z_{gas} across different galactic components

Fig. 6 shows a montage of 2D maps of *q* and six Z_{gas} diagnostics (R_{23}-KK04, R_{23}-M91, N2O2-KD02, O3N2-PP04, N2-D02, and N2-PP04), along with the stellar continuum and extinction-corrected Hα-based SFRs. We do not show the seventh Z_{gas} diagnostic R_{23}-Z94 because it gives very similar results to R_{23}-KK04. Two of these galaxies are barred and isolated (NGC 2907 and 5713), three are unbarred and isolated (NGC 0628, 3938, and 4254), one is barred and weakly interacting (NGC 0337), and one is unbarred and weakly interacting (NGC 5194). The high spatial resolution (median FWHM of the PSF (FPSF) of 387 pc and a median (R_e-bulge/FPSF) of 2.2) and IFU data coverage over a large fraction of the galaxy's disc (median $f_{R_{25}}$ of 0.66) in our sub-sample allows us to resolve individual galaxy components such as the bulge, bar,

and outer disc, and thereby explore how *q*, SFR, and Z_{gas} vary across these components for the seven galaxies.

5.1.1 SFRs

For the central 10–15 kpc mapped by VENGA, our galaxies have an extinction-corrected Hα-based SFR of 0.50–9.50 $M_\odot$ yr^{-1}. We report the total measured Hα SFRs for our VENGA subsample of galaxies along with their TIR-based SFRs in Table 3. Our Hα-based SFRs for all the galaxies in our sub-sample are less than their global TIR-based SFRs (see Section 4.3 and Table 3), with our Hα based SFRs ranging from 34 to 81 per cent of the TIR-based global SFRs. We show the deprojected radial profiles of the SFR surface density Σ_{SFR} ($M_\odot$ yr^{-1} kpc^{-2}) on the right side of Fig. 7. The average Σ_{SFR} falls by over an order of magnitude from the inner 2 kpc to the outer disc. (e.g. from 0.1 to below 0.01 or from 0.01 to below 0.001 $M_\odot$ yr^{-1} kpc^{-2}). The 2D maps of the Hα based SFR (Section 4.3) can be seen in the top centre of Fig. 6, and the maps show that
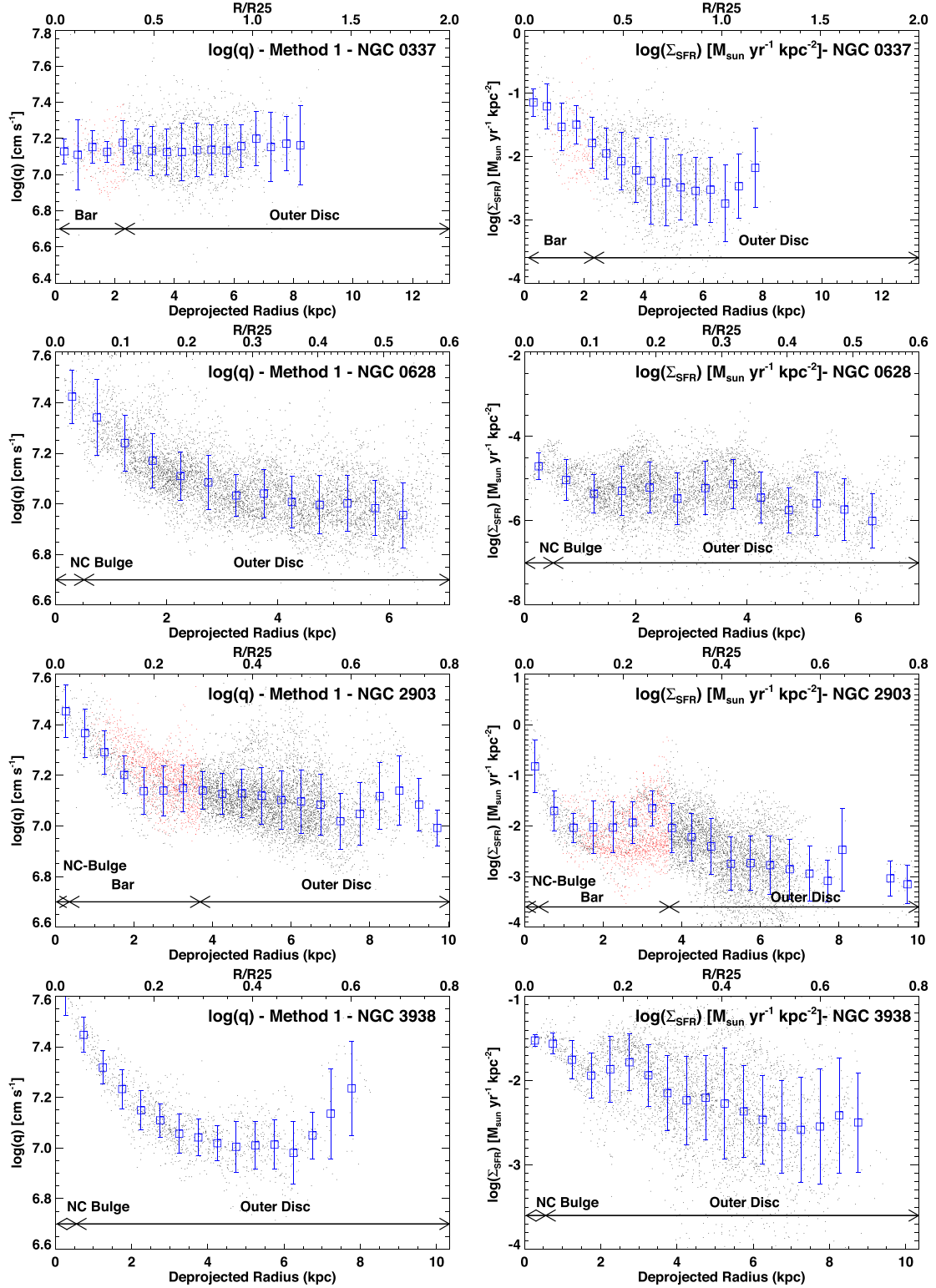
Figure 7. Deprojected radial profiles for the ionization parameter *q* (left; Section 4.4) in units of cm s^{-1} and the SFR surface density Σ_{SFR} in units of M$_\odot$ yr^{-1} kpc^{-2} (right) for NGC 0337, 0628, 2903, and 3938. The arrows on the bottom show our decomposition of each galaxy into non-classical (NC) bulge (which refers to discy/pseudo bulge), bar, and outer disc. The blue squares and error bars are the mean and 1σ dispersion of 0.5 kpc bins. In the case of barred galaxies, the region labelled 'Bar' on the plot refers to the radii between the bulge and the end of the bar. In this region, we show regions in the bar feature as black points, and regions azimuthally offset from the bar feature as red points. The blue squares denoting the mean only use regions within the bar.

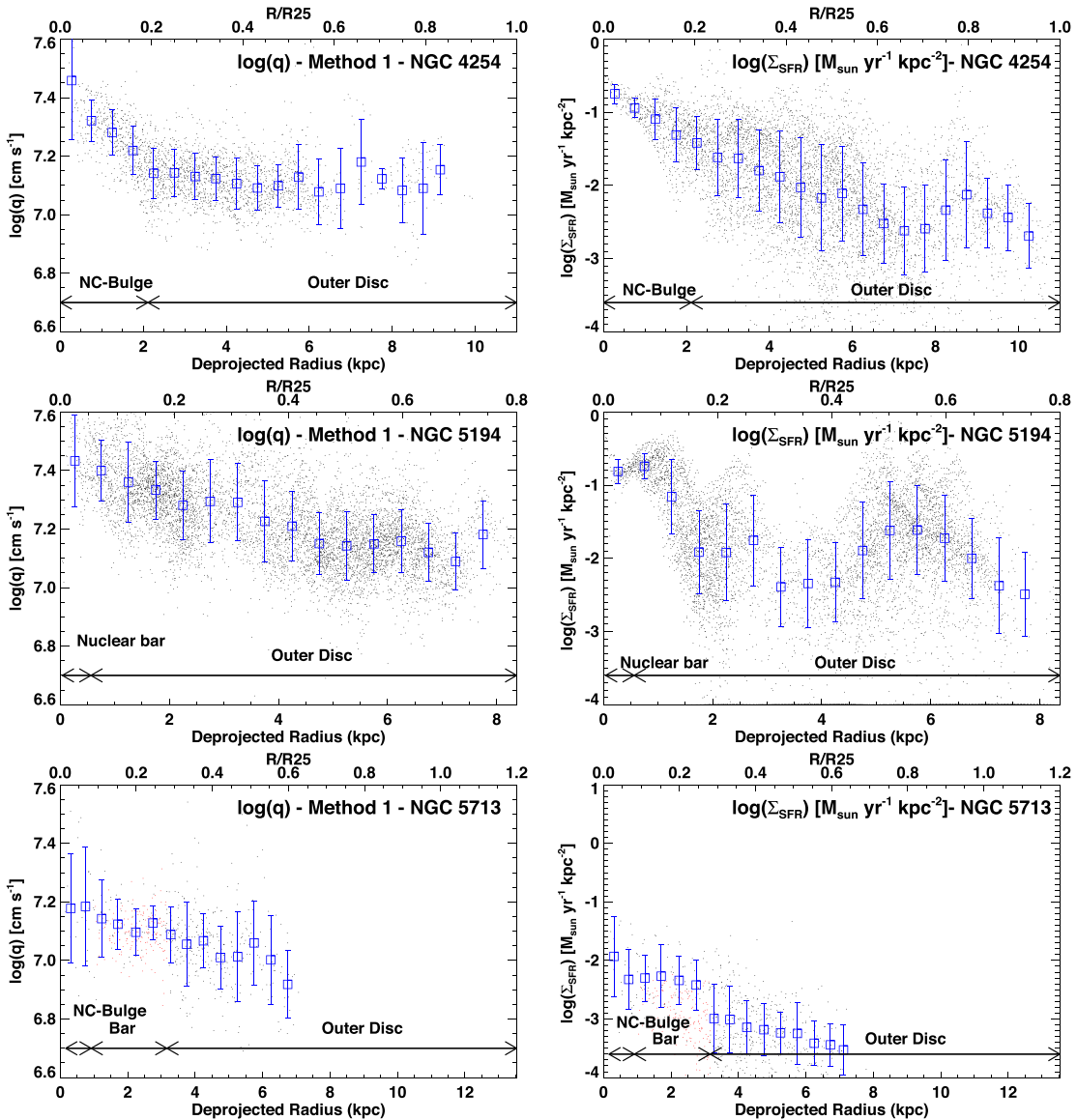**Figure 7** – *continued*: For NGC 4254, 5194, & 5713.

SF tends to be concentrate and in the nuclear regions, bar, and spiral arms and becomes less prominent in the inter-arm regions of the outer disc. The SF shows the patchy morphology expected from the distribution of H II regions throughout a spiral galaxy.

5.1.2 q

The 2D maps of the ionization parameter q (Section 4.4) can be seen in the top right-hand panel in Fig. 6. For most of our galaxies, the maps show a peak in q in the central part of the galaxy and regions of localized enhancements in the outer disc. The distribution of q and SFR are qualitatively similar in many galaxies.

The azimuthally averaged values of q and Σ_{SFR} shown in Fig. 7 complement the 2D maps. For NGC 0628, 2903, 3938, 4254 and 5713, the azimuthally averaged profiles of q and Σ_{SFR} are qualitatively similar, tending to peak in the centre, and to fall at larger radii. The average Σ_{SFR} falls by over an order of magnitude (e.g. from 0.1 to below 0.01 or from 0.01 to below 0.001 $M_\odot$ yr^{-1} kpc^{-2}), the average value of q typically varies by no more than a factor

of 3 (e.g. from 6.95 to 7.40 dex, corresponding to 0.8–3 times 10^7 cm s^{-1}).

In fact, in these galaxies, q does not fall below ∼6.95 dex even at large radii. Similar lower limits in q have been seen by Shields (1990), Dopita et al. (2000), Rosa et al. (2014), Pérez-Montero (2014), and Sánchez et al. (2015). The observed lower limit of $q > 10^7$ cm s^{-1} is not well understood. It might be a limitation of the current photoionization models used in constructing diagnostics for q. Another possible explanation is that the [O III] line intensity becomes dimmer and harder to detect at $q < 10^7$ cm s^{-1} (see evolution of [O III]/Hβ versus q in the figures found in Kewley et al. 2001 and Kewley, Geller & Jansen 2004) due to a combination of a lower number of ionizing photons and a lower ionization fraction for O^{++}, so for any given fibre the [O III] emission detected would be weighted towards regions where the gas has $q \gtrsim 10^7$ cm s^{-1}. There is evidence that q and Z_{gas} are correlated with each other (Freitas-Lemes et al. 2014; Pérez-Montero 2014; Rosa et al. 2014) since metal poor stars give off more ionizing UV radiation (Dors et al. 2011; Sánchez et al. 2015), but we do not notice any clear

Table 4. Summary of the seven Z_{gas} diagnostics.

Z_{gas} diagnostics (1)	Z_{gas} indicator (2)	Reference (3)	Calibration type (4)	q-corrected? (5)
R_{23}-M91	R_{23}=([O II]λ3727+[O III]$\lambda\lambda$4959,5007)/Hβ	McGaugh (1991)	Theoretical	y[a]
R_{23}-KK04	R_{23}=([O II]λ3727+[O III]$\lambda\lambda$4959,5007)/Hβ	Kobulnicky & Kewley (2004)	Theoretical	y[b]
R_{23}-Z94	R_{23}=([O II]λ3727+[O III]$\lambda\lambda$4959,5007)/Hβ	Zaritsky et al. (1994)	Theoretical	n
N2O2-KD02	$N2O2$=[N II]λ6584/[O II]λ3727	Kewley & Dopita (2002)	Theoretical	Invariant[c]
N2-D02	$N2$=[N II]λ6584/Hα	Denicoló, Terlevich & Terlevich (2002)	Empirical	n
N2-PP04	$N2$=[N II]λ6584/Hα	Pettini & Pagel (2004)	Empirical	n
O3N2-PP04	$O3N2$=([O III]$\lambda\lambda$4959,5007/Hβ)/([N II]λ6584/Hα)	Pettini & Pagel (2004)	Empirical	n

Columns: (1) Abbreviation for each Z_{gas} diagnostic. Details for each diagnostic can be found in Section 4.5, Appendix B, and in Kewley & Ellison (2008). (2) The Z_{gas} indicator used for each Z_{gas} diagnostic, and its definition in terms of emission line ratios (see Appendix B for details). (3) Reference from the literature for each Z_{gas} diagnostic. (4) Type of calibration used for each Z_{gas} diagnostic. Theoretical calibrations are based on model H II regions from plasma simulation codes, while empirical calibrations are based on correlations between observed line ratios in H II regions and Z_{gas} derived from the direct T_e method. See Section 4.5 for details. (5) This column indicates whether this Z_{gas} diagnostic is corrected for variations in the ionization parameter q. A 'y' indicates 'yes' and 'n' indicates 'no.'
[a] q corrected for using the [O III]/[O II] line ratio. See Appendix B.
[b] q and Z_{gas} are solved for iteratively as seen in Appendix A.
[c] The [N II]/[O II] line ratio is invariant to the value of q, as shown in Fig. 8.

trends between q and Z_{gas} when comparing them across deprojected radii (Figs 7 and 9) or the 2D maps (Fig. 6).

We also note that the azimuthally averaged profile of q in the weakly interacting late-type galaxy NGC 0337 is markedly different from that of the other six galaxies. In NGC 0337, Σ_{SFR} rises by over an order of magnitude from a radius of 8 kpc to the centre of the galaxy, but the q profile remains flat at a value of $\sim$7.1 dex. The value of q in the central 2 kpc radius of NGC 0337 does not rise to the typical values of 7.4 dex shown by other galaxies although Σ_{SFR} in this region is as high as in NGC 2903, NGC 4254, NGC 5194, and almost a factor of 10 above that of NGC 3938. This effect is not due to distance or resolution effects as NGC 0337 is at a similar distance as NGC 4254 and NGC 3938. Since stellar metallicity is thought to correlate with q (Dors et al. 2011; Sánchez et al. 2015), the flat radial gradient in q in NGC 0337 might possibly be tied to the galaxy's lower absolute metallicity when compared to the other galaxies in our subsample.

5.1.3 Z_{gas}

Our 2D maps (Fig. 6) of six Z_{gas} diagnostics (R_{23}-KK04, R_{23}-M91, N2O2-KD02, O3N2-PP04, N2-D02, and N2-PP04) show a range in Z_{gas} of $\sim$8.5 to 9.3 dex across our spirals. For the Z_{gas} diagnostics using the indicators R_{23} based on ([O II]+[O III])/Hβ, N2O2 based on [N II]/[O II], and O3N2 based on ([O III]/Hβ)/([N II]/Hα), Z_{gas} peaks roughly in the same regions as SF, mainly in the central bulge and along the spiral arms. However, the two Z_{gas} diagnostics (N2-D2 and N2-PP04) based on [N II]/Hα often show spatial trends that are *opposite to those shown by other indicators in regions of high SFR*. For example, in NGC 2903, the N2-D2 and N2-PP04 Z_{gas} diagnostics appear to show lower Z_{gas} along the leading edges of the bar and along the spiral arms than on the trailing edge, while the opposite behaviour is seen in the other Z_{gas} diagnostics (Fig. 6). Similarly flipped behaviour is clearly seen in almost all our galaxies, especially in the spiral arms where there is a high SFR. The inconsistency between the N2-D2 and N2-PP04 diagnostics and the other Z_{gas} diagnostics may be due to several reasons, which we discuss in Section 5.2, point (iii).

Fig. 9 complements the 2D maps and shows deprojected radial Z_{gas} gradients based on all seven Z_{gas} diagnostics for NGC 0337, 0628, 2903, 3938, 4254, 5194, and 5713. In terms of the *shape* of the radial Z_{gas} profile, the seven Z_{gas} diagnostics show fairly good agreement beyond the inner 1–2 kpc, and yield flat to slightly negative gradients (Fig. 9). The gradients are shallow and in dex kpc^{-1}, they range from (0.001 to $-$0.055) in R_{23}-KK04, ($-$0.007 to $-$0.041) in N2O2-KD02 and (0.003 to $-$0.035) in N2-PP04, while in dex $(R/R_{25})^{-1}$ they range from (0.01 to $-$0.77) in R_{23}-KK04, ($-$0.09 to $-$0.57) in N2O2-KD02, and (0.03 to $-$0.57) in N2-PP04. For comparison, the Z_{gas} gradient for the Milky Way was determined by Shaver et al. (1983) using the R_{23} ratio and finds the gradient to be $-$0.07 $\pm$ 0.015 dex kpc^{-1}. Table 5 summarizes the results for our Z_{gas} gradients. It is remarkable that all the galaxies in our sub-sample including unbarred, barred, and interacting galaxies exhibit such flat Z_{gas} gradients across all their galactic components. We return to this point in Sections 5.3 and 5.4.

5.2 Comparison of absolute values of Z_{gas} from different diagnostics

Currently, one long-standing major issue in studies of gas-phase metallicity is that there are systematic offsets between *absolute* values of Z_{gas} given by the different diagnostics. Attempts have been made to reconcile the differences between the diagnostics (for example see Kewley & Dopita 2002; Kewley & Ellison 2008; Lopez-Sanchez & Esteban 2010; Blanc et al. 2015), but the issue is far from settled. Using our 2D maps (Fig. 6) and radial gradients (Fig. 9) of the seven Z_{gas} diagnostics (R_{23}-KK04, R_{23}-M91, R_{23}-Z94, N2O2-KD02, O3N2-PP04, N2-D02, and N2-PP04), we explore how the absolute value of Z_{gas} varies between some of the different Z_{gas} diagnostics:

(i) R_{23} Z_{gas} *diagnostics.* The three R_{23} Z_{gas} diagnostics (R_{23}-KK04, R_{23}-M91, R_{23}-Z94) show a similar shape in the radial profile of Z_{gas} and yield absolute values that agree within 0.1–0.2 dex. The fact that these three Z_{gas} diagnostics agree within 0.1–0.2 dex although they do not all use q to estimate Z_{gas} (see Appendices A and B) is likely due to the fact that we are on the upper branch of R_{23} where Z_{gas} is high ($>$8.87) and there is only a small dependence on q (see top left of Fig. 8).

(ii) *The N2O2-KD02 Z_{gas} diagnostic.* The N2O2-KD02 diagnostic shows a low amount of scatter when compared to the R_{23} and N2
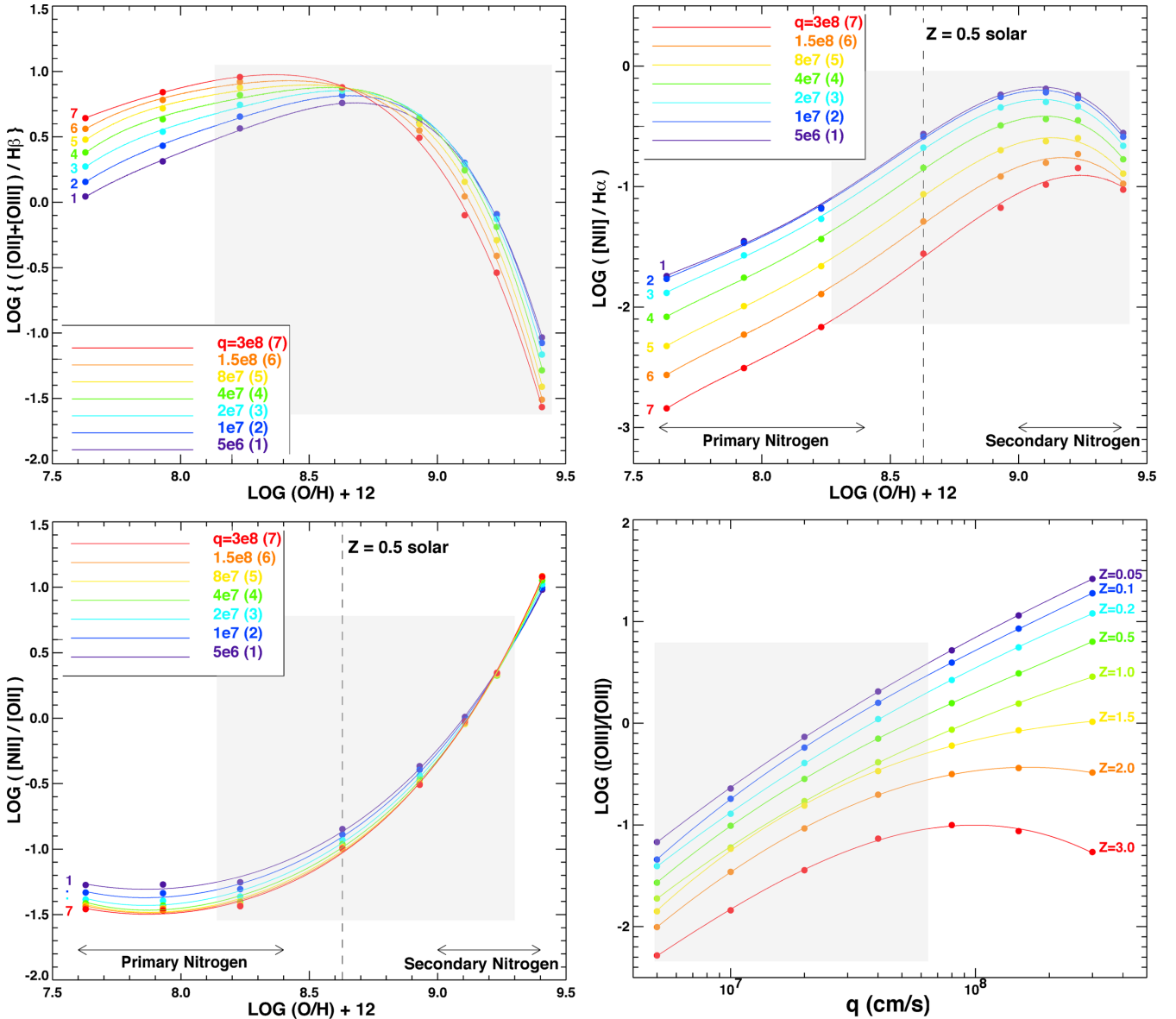
Figure 8. Plots from Kewley & Dopita (2002) showing the theoretical dependence of different emission line ratios on the gas phase metallicity Z_{gas} (defined as log(O/H)+12) and ionization parameter q for gas in regions primarily photoionized by photons from massive stars. The shaded rectangles illustrate the range of values for the line ratios, Z_{gas}, and q found in our data. The line ratio ([O II]+[O III])/Hβ defining the Z_{gas} indicator R_{23} varies with Z_{gas} and q. High values of R_{23} are degenerate with Z_{gas} at a given q (top left). The [N II]/[O II] ratio used to define the N2O2 Z_{gas} indicator is not highly sensitive to q (bottom left). The [N II]/Hα is used to define the N2 Z_{gas} indicator (top right). The [O III]/[O II] line ratio is highly sensitive to q (bottom right).

diagnostics. N2O2-KD02 gives Z_{gas} values similar to the three main R_{23} diagnostics (R_{23}-KK04, R_{23}-M91, and R_{23}-Z94). We note that N2O2-KD02 is a theoretical calibration that uses the [N II]/[O II] line ratio, which has little dependence on q (Fig. 8).

(iii) *The N2-D02 and N2-PP04 Z_{gas} diagnostics.* The N2-D02 and N2-PP04 Z_{gas} diagnostics use the [N II]/Hα line ratio and are based on empirical calibrations that do not correct for local variations in q. N2-PP04 gives a Z_{gas} that tends to be systematically lower, by as much as 0.4 dex, compared to the three main R_{23} diagnostics (R_{23}-KK04, R_{23}-M91, and R_{23}-Z94). The systematically lower Z_{gas} values given by the empirically calibrated N2-D02 and N2-PP04 diagnostics, compared to the theoretically-calibrated R_{23} diagnostics, is likely related to the temperature gradients and variations in the nebulae used as empirical calibrators (Kewley & Ellison 2008). Furthermore, in the inner 2 kpc of some of our galaxies, the radial

gradients in Z_{gas} given by N2-D02 and N2-PP04 can *be opposite to those* given by other diagnostics. For instance, in NGC 2903, the first five Z_{gas} diagnostics give a slightly negative to flat Z_{gas} gradient in the inner 1.5 kpc radius, but N2-KD02 and N2-PP04 give a slightly positive gradient, which then inverts (see Fig. 9). Similar opposite trends were seen in the 2D maps of Z_{gas} (see Section 5.1.2). A milder example can be seen in the form of a negative central gradient in NGC 4254.

We have explored possible explanations for the large difference between the N2-D02 and N2-PP04 diagnostics and the R_{23} diagnostics. At typical q values below 10^8 cm s^{-1}, high [N II]/Hα (>0.1) values allow for two possible values of Z_{gas}, which are typically above and below 9.1 dex (see upper right-hand panel of Fig. 8). Therefore, one possible reason for erroneous Z_{gas} is that the N2-D02 and N2-PP04 diagnostics are picking the wrong value of Z_{gas}.
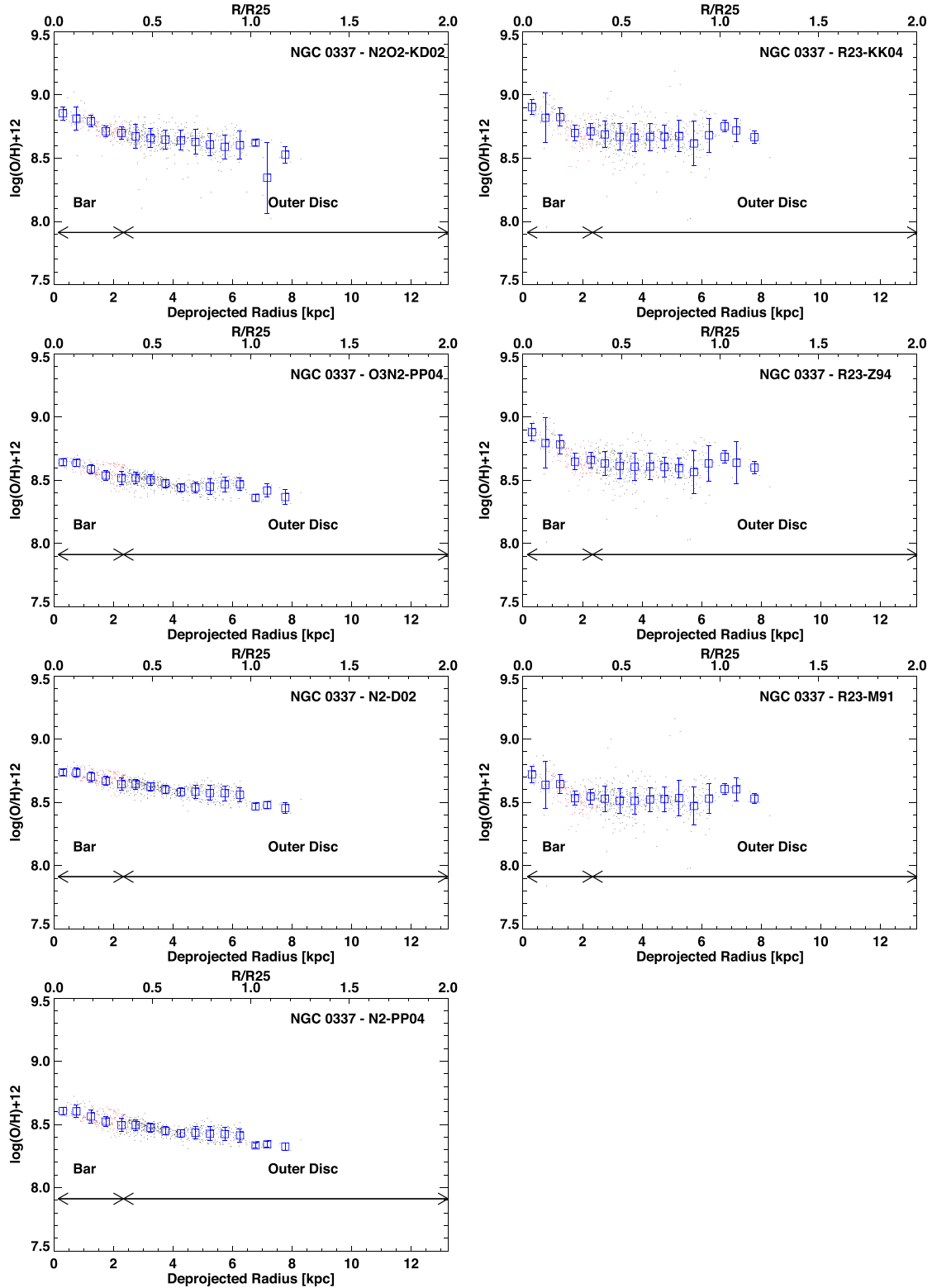
Figure 9. For NGC 0337, we show the deprojected radial Z_{gas} profiles for the seven different Z_{gas} diagnostics: N2O2-KD02, R_{23}-KK04, O3N2-PP04 R_{23}-Z94, N2-D02, R_{23}-M91, and N2-PP04. The arrows on the bottom show our decomposition of each galaxy into non-classical (NC) bulge (which refers to discy/pseudo bulge), bar, and outer disc. The blue squares and error bars are the mean and 1σ dispersion of 0.5 kpc bins. In the case of barred galaxies, the region labelled 'Bar' on the plot refers to the radii between the bulge and the end of the bar. In this region, we show regions in the bar feature as black points, and regions azimuthally offset from the bar feature as red points. The blue squares denoting the mean only use regions within the bar. The white masked regions in the maps represent spaxels, which were not used in the computation of Z_{gas} and q because they are associated with data of low quality or dominated by DIG or gas with LINER or Seyfert excitation conditions.
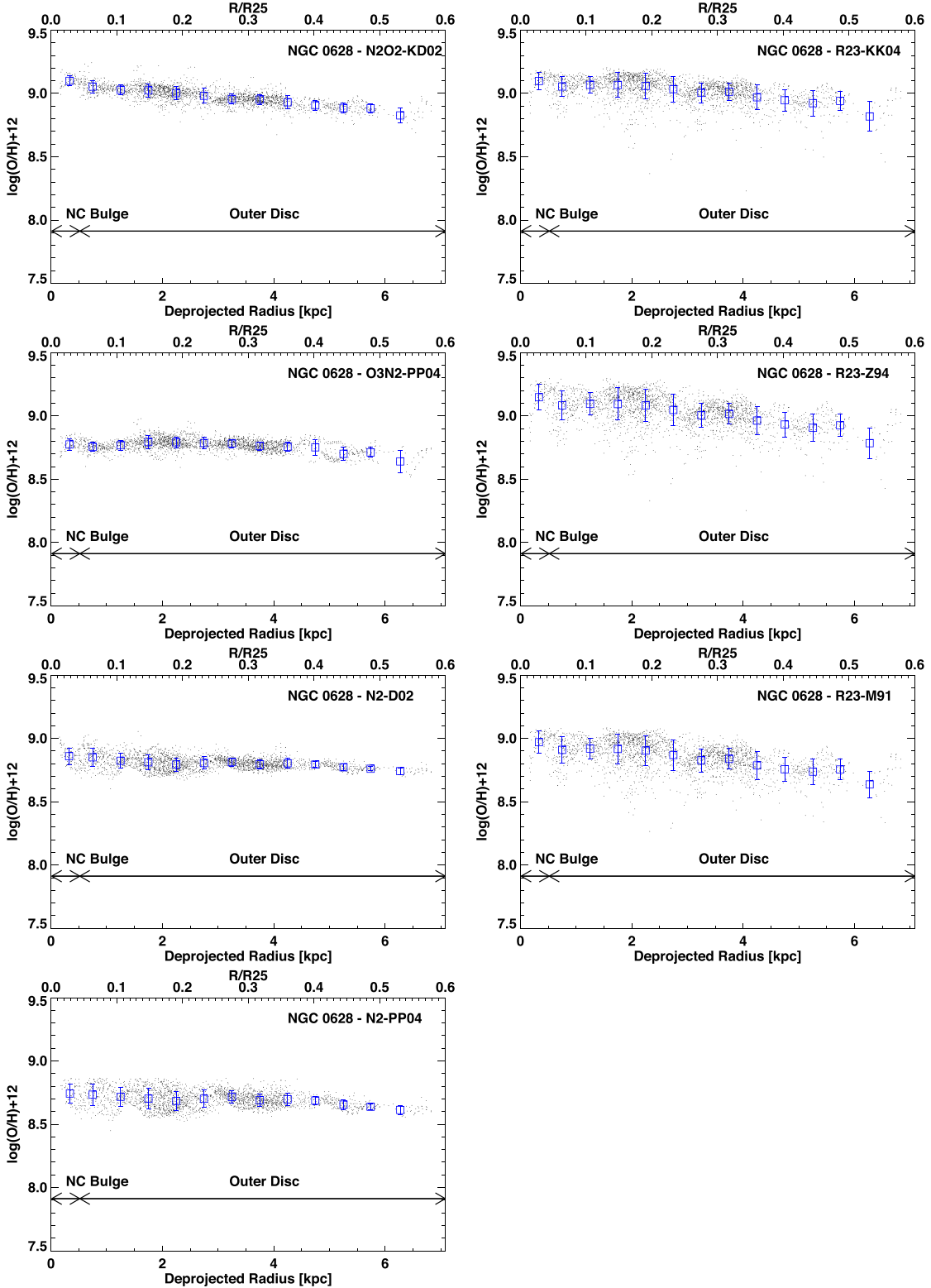
Figure 9 – *continued*: For NGC 0628.

A second possibility is that erroneous Z_{gas} values are caused by the fact that the N2-KD02 and N2-PP04 empirical calibrations do not take into account variations in q when computing Z_{gas}.

To evaluate the impact of q variations, we attempted to calculate Z_{gas} by interpolating over the theoretical [N II]/Hα curves from

Kewley & Dopita (2002) which use the [N II]/Hα ratio and corrects explicitly for local variations in q. For this exercise, we used the q we calculated based on the [O III]/[O II] line ratio (Section 4.4). We found that the shape and absolute value of the radial profiles did not change significantly from the empirical N2-D02 and N2-PP04
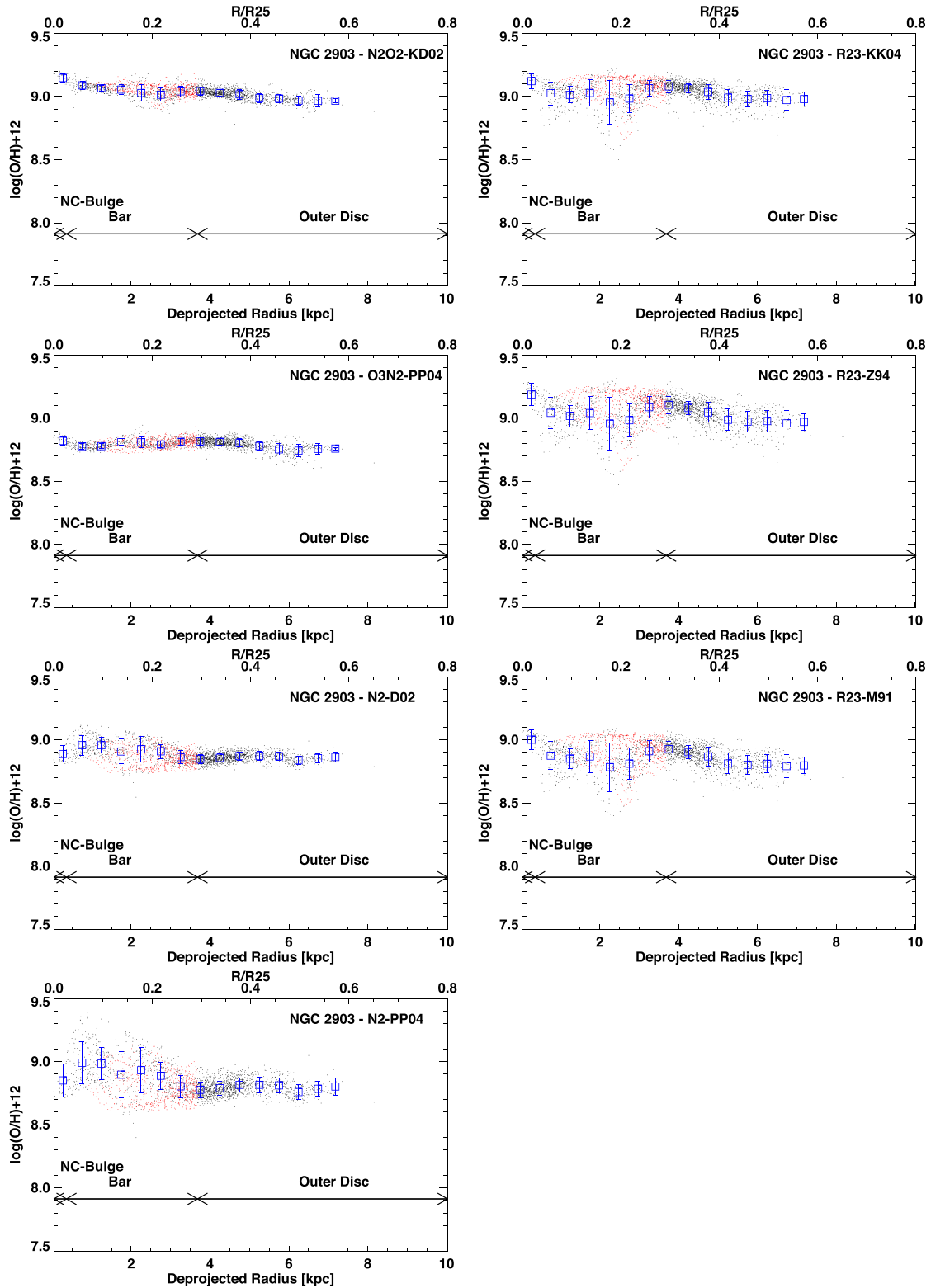
Figure 9 – *continued*: For NGC 2903.

diagnostics, suggesting that variations in q are not at the root of the problem.

(iv) *The O3N2-PP04 Z_{gas} diagnostic.* The O3N2-PP04 diagnostic shows a low amount of scatter when compared to the R_{23} diagnostics, and yields a Z_{gas} value that is systematically lower by 0.2 to 0.3 dex compared to the three main R_{23} diagnostics. The fact that the empirically calibrated diagnostics, O3N2-PP04, as well as N2-D02 and N2-PP04 (discussed in point (iii)), give systematically lower Z_{gas} than the theoretically-calibrated R_{23} diagnostics, suggests that temperature gradients and variations in the nebulae used as empirical calibrators (Kewley & Ellison 2008) may be important. A related factor is that the O3N2-PP04 diagnostic does not correct for
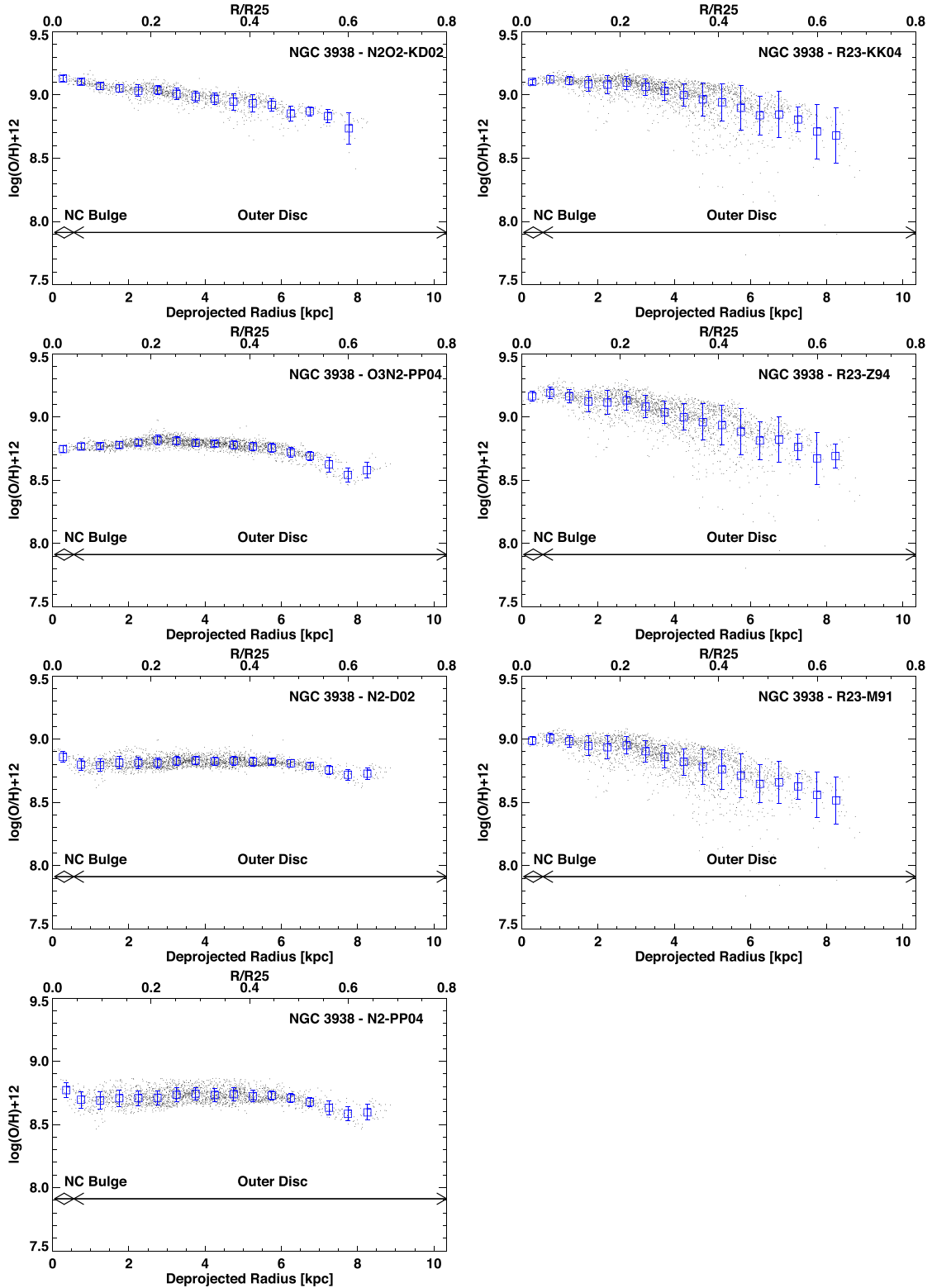
Figure 9 – *continued*: For NGC 3938.

local variations in q. This is particularly problematic because our procedure of using a fixed $H\beta/H\alpha$ value for extinction correction means that the O3N2-PP04 diagnostic effectively depends directly on the [O III]/[N II] line ratio, which is shown by Kewley & Dopita (2002) to be strongly dependent on q.

5.3 Comparison of Z_{gas} between barred and unbarred galaxies

5.3.1 Our results

Column 7 of Table 1 indicates whether our sample galaxies host a large-scale stellar bar. In making this assessment, we do not
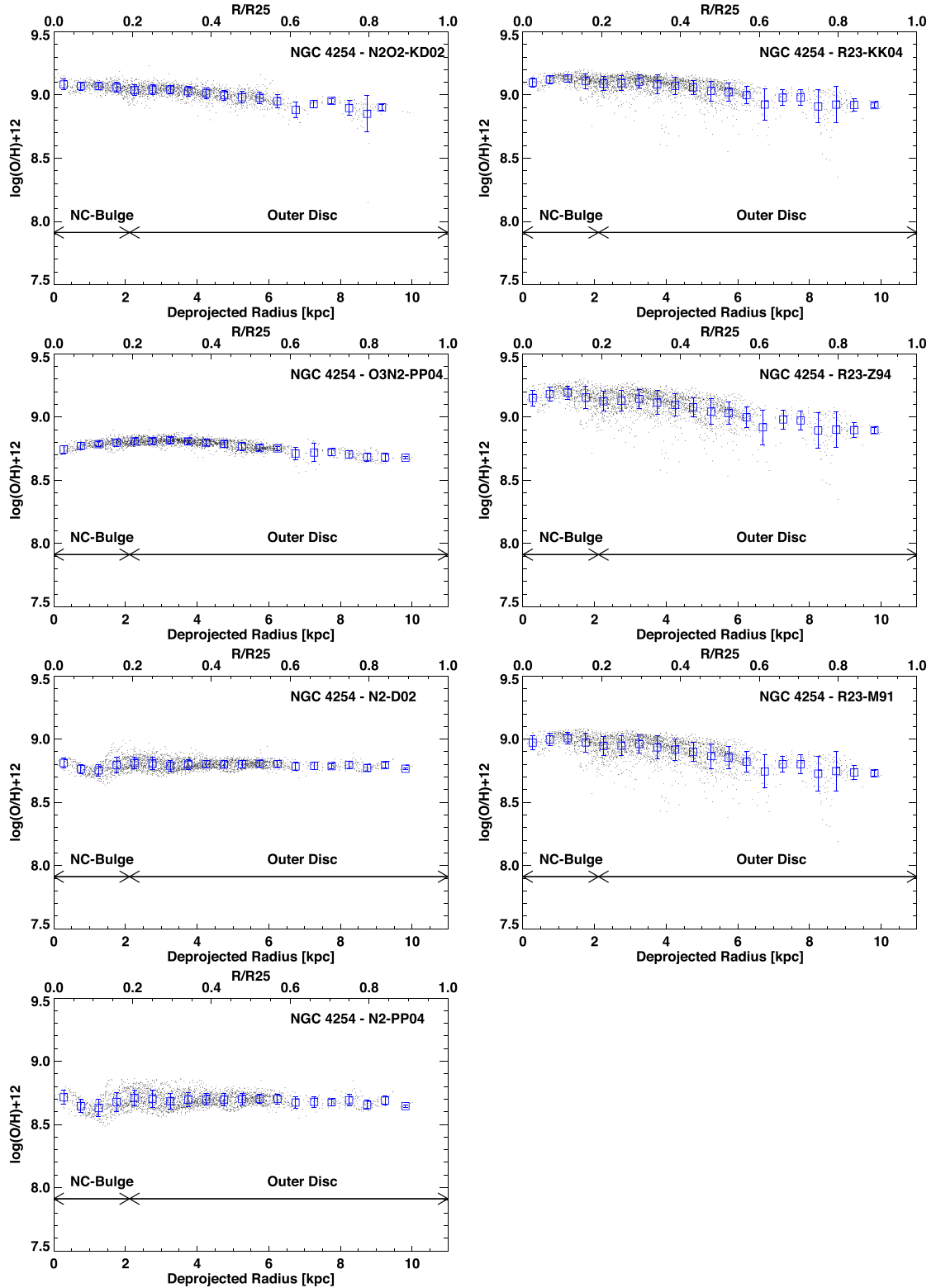
Figure 9 – *continued*: For NGC 4254.

rely solely on the RC3 classification as these are based on visual inspection of optical photographic plates (de Vaucouleurs et al. 1991) and may suffer from obscuration by dust and SF. Instead, we also use quantitative analyses of near-infrared images (Table 6), such as ellipse fits (Marinova & Jogee 2007; Menéndez-Delmestre et al. 2007), multicomponent bulge-bar-disc decomposition (Weinzirl et al. 2009), and Fourier decomposition (Laurikainen & Salo 2002). For all sample galaxies, the NIR-based methodologies agree with the RC3 classification on the presence/absence of a large-scale stellar bar. We classify NGC 1068 and 5194 as
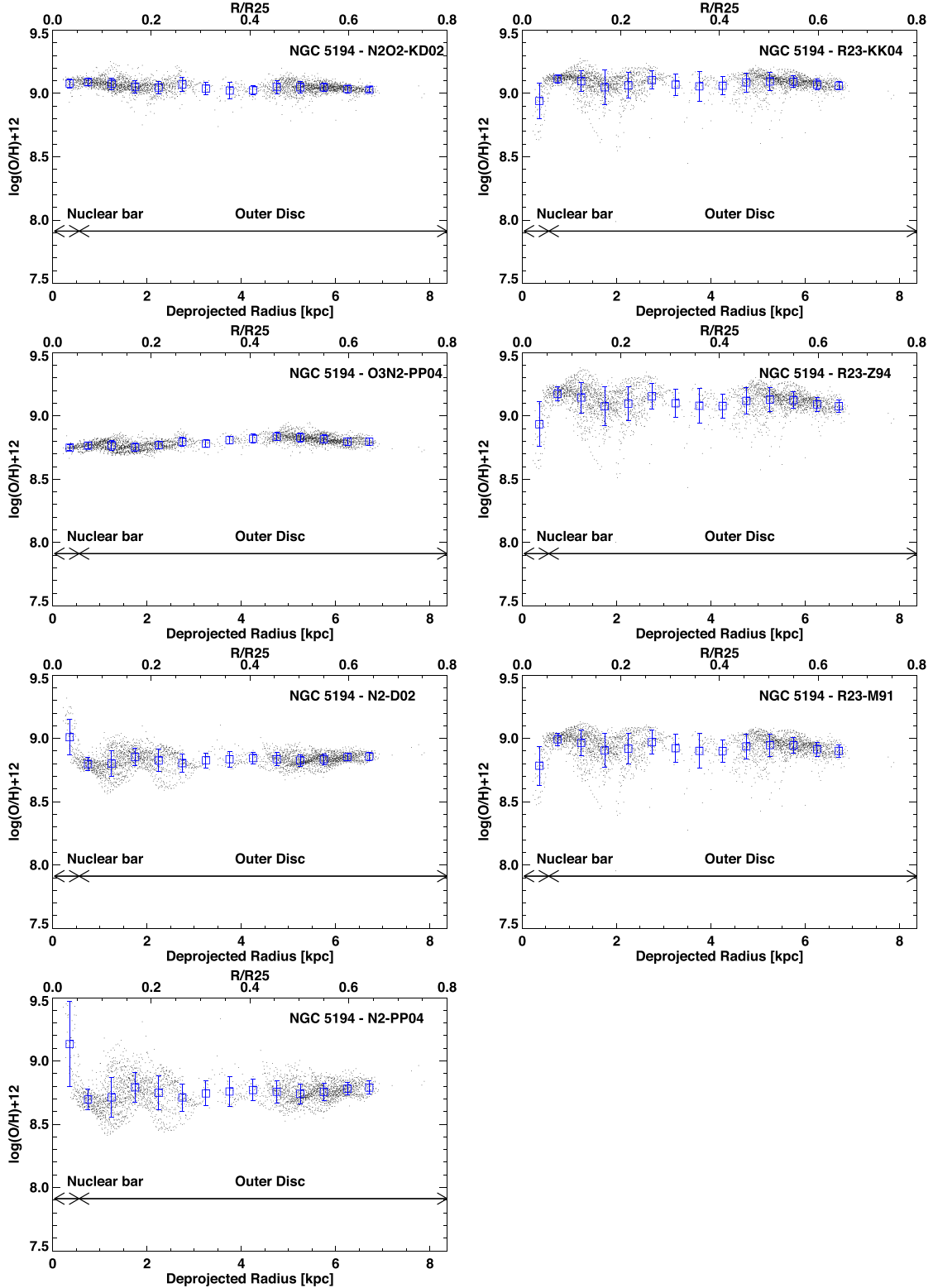
Figure 9 – *continued*: For NGC 5194.

unbarred because they do not host large-scale stellar bars and show evidence of only nuclear bars with respective $a_{bar}/R_{25} = 0.07$ and 0.06, (Menéndez-Delmestre et al. 2007), where a_{bar} denotes the bar semi-major axis. Large-scale stellar bars have typical a_{bar}/R_{25} ranging from 0.1 to 0.5 (Erwin 2005; Marinova &

Jogee 2007), while nuclear bars have $a_{bar}/R_{25} < 0.1$ (Laine et al. 2002), and are thus are too short to significantly impact the outer disc. The final division of our sample yields two barred isolated galaxies (NGC 2903 and 5713), three unbarred isolated galaxies (NGC 0628, 3938, and 4254), one barred weakly interacting
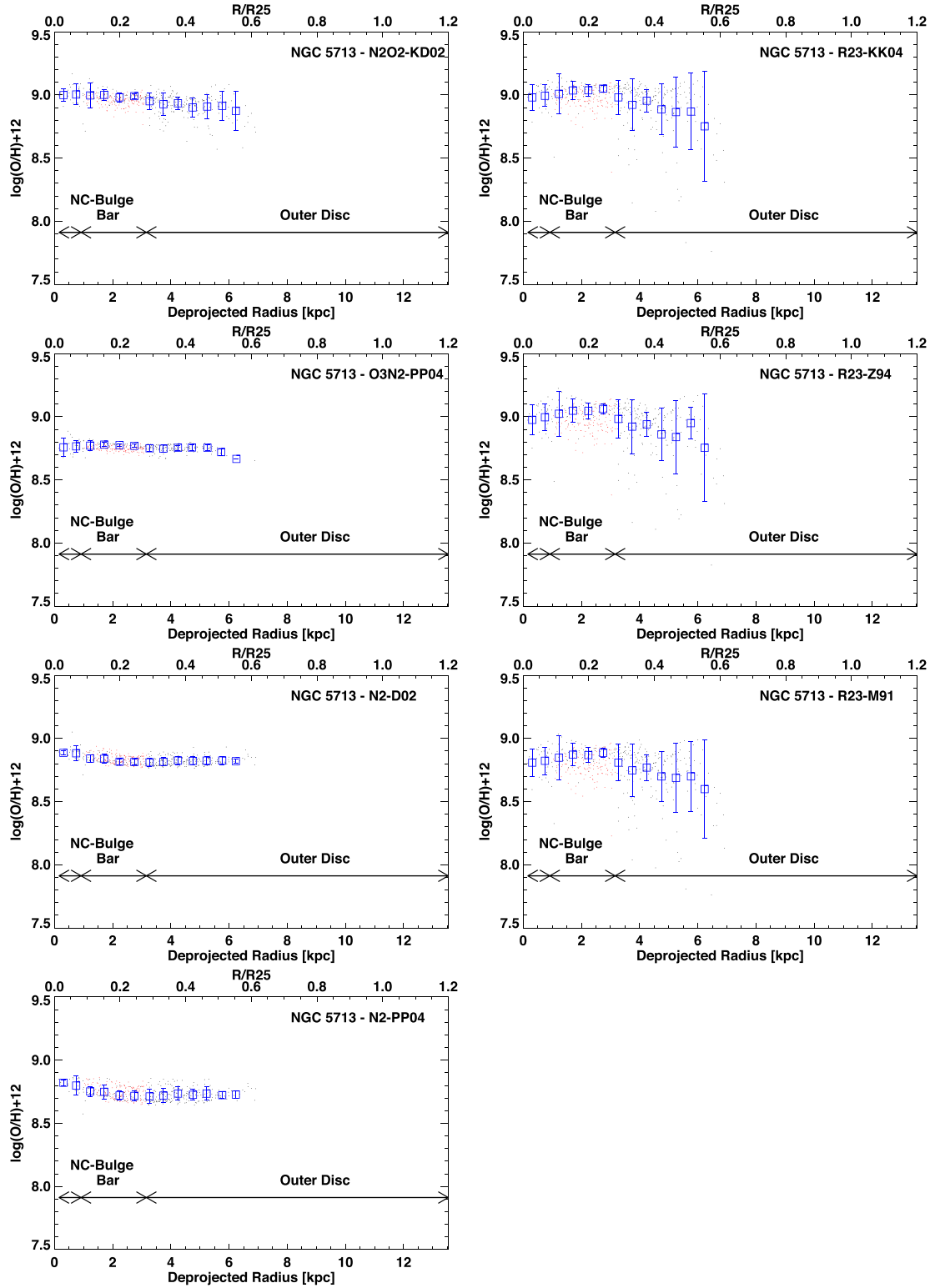
Figure 9 – *continued*: For NGC 5713.

galaxy (NGC 0337[4]), and one unbarred weakly interacting galaxy (NGC 5194).

Fig. 10 over-plots the Z_{gas} radial profiles from the R_{23}-KK04 diagnostic. In terms of the absolute value of Z_{gas}, the lowest mean Z_{gas} occur in the galaxy NGC 0337, which has the latest Hubble type (Sd) and the lowest stellar mass (1.6×10^{10} M$_\odot$). The other six galaxies, which have higher stellar masses and later Hubble types, show Z_{gas} values higher than those in NGC 0337,

---

[4] There is some evidence that NGC 0337 might be undergoing an interaction or minor merger. See notes for column 8 in Table 1.

Table 5. Summary of Z_{gas} gradients in our study and other published studies.

Reference (1)	Galaxy or class of galaxies (2)	Z_{gas} diagnostic (3)	dex $(R/R_{25})^{-1}$ or dex$/(R_e)^a$ (4)	dex kpc^{-1} (5)
Our results for barred and unbarred spirals at $z \sim 0^b$ using the N2O2-KD02 Z_{gas} diagnostic				
This study	NGC 0337 (Sd, barred/weakly inter.)	N2O2-KD02	-0.31 ± 0.02	-0.038 ± 0.002
This study	NGC 0628 (Sc, unbarred/isolated)	N2O2-KD02	-0.49 ± 0.01	-0.037 ± 0.001
This study	NGC 2903 (Sbc, barred/isolated)	N2O2-KD02	-0.32 ± 0.01	-0.019 ± 0.001
This study	NGC 3938 (Sc, unbarred/isolated)	N2O2-KD02	-0.57 ± 0.01	-0.041 ± 0.001
This study	NGC 4254 (Sc, unbarred/isolated)	N2O2-KD02	-0.26 ± 0.01	-0.023 ± 0.001
This study	NGC 5194 (Sbc, unbarred/weakly inter.)	N2O2-KD02	-0.09 ± 0.01	-0.007 ± 0.001
This study	NGC 5713 (Sbc, barred/isolated)	N2O2-KD02	-0.34 ± 0.04	-0.026 ± 0.003
This study	All seven galaxies	N2O2-KD02	-0.34 ± 0.14	-0.027 ± 0.011
This study	4 unbarred	N2O2-KD02	-0.35 ± 0.19	-0.028 ± 0.013
This study	3 barred	N2O2-KD02	-0.32 ± 0.01	-0.028 ± 0.008
This study	3 unbarred/isolated	N2O2-KD02	-0.44 ± 0.13	-0.034 ± 0.008
This study	2 barred/isolated	N2O2-KD02	-0.33 ± 0.01	-0.023 ± 0.003
This study	1 unbarred/weakly interacting	N2O2-KD02	-0.09 ± 0.01	-0.007 ± 0.001
This study	1 barred weakly interacting	N2O2-KD02	-0.31 ± 0.02	-0.038 ± 0.002
Our results for barred and unbarred spirals at $z \sim 0$ using the R_{23}-KK04 Z_{gas} diagnostic				
This study	All seven galaxies	R_{23}-KK04	-0.33 ± 0.26	-0.026 ± 0.018
This study	4 unbarred	R_{23}-KK04	-0.036 ± 0.28	-0.027 ± 0.020
This study	3 barred	R_{23}-KK04	-0.28 ± 0.21	-0.024 ± 0.016
This study	3 unbarred/isolated	R_{23}-KK04	-0.49 ± 0.21	-0.037 ± 0.013
This study	2 barred/isolated	R_{23}-KK04	-0.33 ± 0.25	-0.024 ± 0.019
This study	1 unbarred/weakly inter.	R_{23}-KK04	0.01 ± 0.01	0.001 ± 0.001
This study	1 barred weakly inter.	R_{23}-KK04	-0.20 ± 0.03	-0.025 ± 0.003
Our results for barred and unbarred spirals at $z \sim 0$ using the O3N2-PP04 Z_{gas} diagnostic				
This study	All seven galaxies	O3N2-PP04	-0.11 ± 0.13	-0.010 ± 0.012
This study	4 unbarred	O3N2-PP04	-0.09 ± 0.15	-0.007 ± 0.011
This study	3 barred	O3N2-PP04	-0.14 ± 0.08	-0.014 ± 0.012
This study	3 unbarred/isolated	O3N2-PP04	-0.18 ± 0.05	-0.014 ± 0.003
This study	2 barred/isolated	O3N2-PP04	-0.09 ± 0.01	-0.006 ± 0.001
This study	1 unbarred/weakly interacting	O3N2-PP04	0.16 ± 0.01	0.011 ± 0.001
This study	1 barred weakly interacting	O3N2-PP04	-0.25 ± 0.01	-0.031 ± 0.001
Our results for barred and unbarred spirals at $z \sim 0$ using the N2-PP04^c Z_{gas} diagnostic				
This study	All seven galaxies	N2-PP04	-0.16 ± 0.19	-0.012 ± 0.014
This study	4 unbarred	N2-PP04	-0.04 ± 0.08	-0.003 ± 0.006
This study	3 barred	N2-PP04	-0.31 ± 0.20	-0.025 ± 0.013
This study	3 unbarred/isolated	N2-PP04	-0.07 ± 0.08	-0.005 ± 0.006
This study	2 barred/isolated	N2-PP04	-0.33 ± 0.24	-0.021 ± 0.014
This study	1 unbarred/weakly interacting	N2-PP04	0.02 ± 0.01	0.001 ± 0.001
This study	1 barred weakly interacting	N2-PP04	-0.26 ± 0.01	-0.033 ± 0.001
Published IFU studies of spirals at $z \sim 0$ using the O3N2-PP04 Z_{gas} diagnostic				
Sánchez et al. (2014)	38 barred (RC3 type B)	O3N2-PP04	-0.09 ± 0.07^a	–
Sánchez et al. (2014)	30 barred (RC3 type AB)	O3N2-PP04	-0.13 ± 0.09^a	–
Sánchez et al. (2014)	78 unbarred (RC3 type A)	O3N2-PP04	-0.12 ± 0.08^a	–
Published studies of isolated and strongly interacting spirals at $z \sim 0$				
Rupke et al. (2010)	16 strongly interacting	N2O2-KD02	-0.25 ± 0.11	-0.020 ± 0.009
Rupke et al. (2010)	11 isolated	N2O2-KD02	-0.57 ± 0.18	-0.051 ± 0.030
Kewley et al. (2010)	8 strongly interacting	N2O2-KD02	-0.25 ± 0.12	–
Published studies at higher z using the N2-PP04 zgas diagnostic.				
Yuan et al. (2011)	Sp1149 ($z \sim 1.5$)	N2-PP04	-1.92 ± 0.24	-0.16 ± 0.02
Jones et al. (2010)	Clone Arc ($z \sim 2$)	N2-PP04	–	-0.27 ± 0.05

Columns: (1) Reference for Z_{gas} study. (2) Name and/or classification (Hubble class, barred versus unbarred, isolated versus weakly or strongly interacting) galaxy or set of galaxies. (3) Z_{gas} diagnostic used for reported Z_{gas} gradients. (4) Z_{gas} gradient in units of dex $(R/R_{25})^{-1}$ or dex$/(R_e)^a$. Reported gradients for single galaxies are the slope from linear least squares fit to equal data points, and the reported uncertainty is the 1σ uncertainty in the slope's fit. Reported gradients for groups of galaxies are the mean gradient of the group and the uncertainty is the 1σ scatter about the mean. (5) Z_{gas} gradient reported in the same manner as column 4, but in units of dex kpc^{-1}.
^{a}We give dex $(R/R_{25})^{-1}$ for all studies except for Sánchez et al. (2014) where we give dex$/(R_e)^{-1}$
^{b}Note that NGC 1068 has been excluded from Z_{gas} analysis since most of the gas is excited by the central AGN. See Section 5.1 and Fig. 4.
^{c}Note that we consider the N2 Z_{gas} diagnostics less reliable than the other Z_{gas} diagnostics, as discussed in Section 5.2. Since N2 diagnostics are frequently used in high redshift Z_{gas} studies as discussed in Section 5.4, we report N2-PP04 Z_{gas} gradients here for our VENGA sub-sample.

Table 6. Bar identification.

NGC (1)	RC3 bar identification (2)	NIR large-scale bar identification (3)	NIR references (4)
0337	SB	Barred	MD07
0628	SA	Unbarred	MD07
1068	SA	Unbarred[a]	MD07, LS02
2903	SAB	Barred	LS02
3938	SA	Unbarred	MD07, MJ07, W09
4254	SA	Unbarred	MD07, MJ07, W09
5194 (M51a)	SA	Unbarred[a]	MD07
5713	SAB	Barred	MD07, MJ07, LS02

Columns: (1) NGC galaxy name. (2) Bar identification in RC3 based on qualitative examination of galaxies imaged with photographic plates at optical wavelengths (de Vaucouleurs et al. 1991). SA = Unbarred; SAB = Intermediate bar strength; SB = Barred. See Section 5.3 for more details. (3) Large-scale bar identification based on quantitative analysis of near-infrared (J,H, or K band) images. We use this classification to definitively identify galaxies with and without large-scale stellar bars, since the qualitative classification from photographic plates at optical wavelengths can be significantly affected by dust obscuration, ongoing star formation, and the subjective judgement of the classifier. See column (4) for references and Section 5.3 for more details. (4) The abbreviated references for the bar identification in column (3) refer to the following papers and methodologies: MD07 = (Menéndez-Delmestre et al. 2007) ellipse fitting to 2MASS *JHK*-band images; MJ07 = (Marinova & Jogee 2007) ellipse fitting to OSU *H*-band images taking into account projection effects; W09 = (Weinzirl et al. 2009) multicomponent bulge-bar-disc decomposition of OSU H-band images; LS02 = (Laurikainen & Salo 2002) Fourier decomposition of 2MASS JHK-band images. [a]NGC 5194 (M51a) and NGC 1068 do not appear to host large-scale stellar bars, but do host nuclear bars. The small size of nuclear bars compared to the total size of the disc in a galaxy limits their ability to radially redistribute gas, so we classify these galaxies as 'Unbarred'. These nuclear bar structures are confirmed in both galaxies by Menéndez-Delmestre et al. (2007), where $a_{bar}/R_{25} < 0.1$.

by ∼0.1 to 0.4 dex, depending on the radius being considered. These differences in the value of Z_{gas} are expected from the mass–metallicity relation (e.g. Tremonti et al. 2004; Lee et al. 2006; Zhao et al. 2010).

The most interesting result, however, lies in the similar shape of the Z_{gas} profile shown by barred and unbarred galaxies. Table 5 shows the Z_{gas} gradients for all our sample galaxies, differentiating between isolated barred/unbarred spirals versus those that may be weakly interacting barred/unbarred spirals. This is important in order to try to disentangle the effect of the bar from that of an ongoing interaction. Table 5 also lists the gradients found in other Z_{gas} studies. For the individual galaxies, we report the Z_{gas} gradients as the slope of a linear least squares fit to the equally weighted data points along with the 1σ uncertainty of the slope in the fit. For groups of galaxies, we report the mean Z_{gas} gradient and 1σ scatter about the mean. While our high spatial resolution and radial profiles in Figs 9 and 10 shows that the Z_{gas} radial profiles in our galaxies have fine structure and are probably not best fit with a single line, we use a linear fit to allow a statistical comparison of the Z_{gas} gradients in our galaxy sample to other studies.

Isolated barred and unbarred galaxies in our sample exhibit similarly shaped Z_{gas} profiles, which are flat or show very small negative gradients from the inner kpc out to large radii (7–10 kpc or 0.5–1.0R_{25}) in the outer disc. Specifically, the isolated barred galaxies (NGC 2903 and NGC 5713) show very shallow N202-KD02 Z_{gas} gradients of -0.33 ± 0.01 in units of dex $(R/R_{25})^{-1}$ and $-0.023/ \pm 0.003$ in units of dex kpc^{-1}. The three isolated unbarred galaxies (NGC 0628, 3938, and 4254) also show similarly shallow Z_{gas} gradients of -0.44 ± 0.13 in units of dex $(R/R_{25})^{-1}$ and -0.034 ± 0.008 in units of dex kpc^{-1}. There is no statistically significant difference between the Z_{gas} gradients reported for isolated barred versus unbarred spirals in our sample. The values cited above are for the N2O2-KD02 Z_{gas} diagnostic, but the other Z_{gas} diagnostics

give similarly shallow negative gradients as seen in Table 5 and Fig. 9.

Some studies (e.g. see Sánchez et al. 2012, 2014) caution that differences in Z_{gas} profiles may arise due to different units used for radial distance (kpc versus the disc half-light radius R_e). It is therefore relevant to note that our Z_{gas} profiles show no significant difference between barred and unbarred galaxies even when we use different radial units, such as the radius in absolute units of kpc (top panel of Fig. 10) or the radius scaled in terms of half-light radius R_e or R_{25} (e.g. bottom panel of Fig. 10).

Disentangling the effect of bars from minor mergers and tidal interactions is difficult for several reasons. Bars can form spontaneously in an isolated galaxy or can be induced via a tidal interaction or minor merger (e.g. Hernquist & Mihos 1995). Furthermore, during a tidal interaction or minor merger, gas inflows are driven by tidal torques from the smaller companion, as well as torques from a bar induced in the disc of the primary (e.g. Hernquist & Mihos 1995). Therefore, we exert extra caution in our analysis by separating our *isolated* barred/unbarred galaxies from *weakly interacting* barred/unbarred galaxies. The two weakly interacting galaxies (NGC 0337, NGC 5194 or M51a) in our sample have properties consistent with minor interactions/mergers of mass ratios below 1:3, and their morphologies are regular enough for a bar type (barred or unbarred) to be reliably assigned. The two left-hand panels of Figs 11 and 12, show our data for barred and unbarred galaxies, divided between isolated (top row) and interacting (bottom row). The N2O2-KD02 Z_{gas} gradient for the interacting barred Sd galaxy NGC 0337 is -0.31 ± 0.02 dex $(R/R_{25})^{-1}$, compared to -0.33 ± -0.01 dex $(R/R_{25})^{-1}$ for the isolated barred galaxies (NGC 2903 and NGC 5713). Similarly, the Z_{gas} gradient for the weakly interacting unbarred Sbc galaxy NGC 5194 is -0.09 ± 0.01 dex $(R/R_{25})^{-1}$, compared to -0.44 ± 0.13 dex $(R/R_{25})^{-1}$ for the isolated unbarred galaxies (NGC 0628, 3938, and 4254). This comparison hints at the
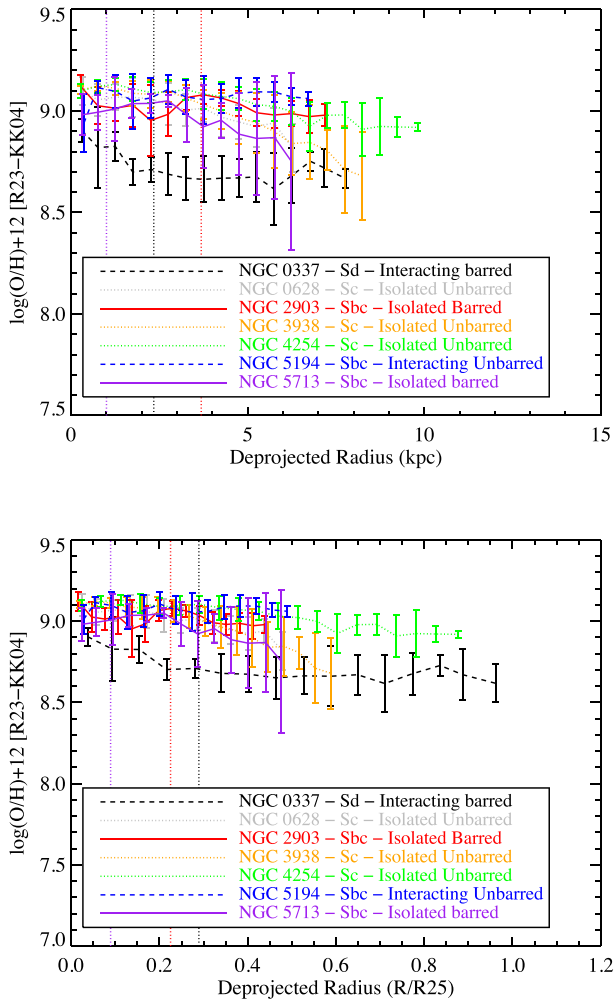
Figure 10. Comparison of deprojected Z_{gas} profiles using the R_{23}-KK04 diagnostic for two barred isolated galaxies (NGC 2903 and NGC 5713; solid line), three unbarred isolated galaxies (NGC 0628, NGC 3938, and NGC 4254; dotted lines), one barred weakly interacting galaxy (NGC 0337; dashed line), and one unbarred weakly interacting galaxy (NGC 5194; dashed line). The horizontal axis shows the deprojected radius in units of kpc (top plot) and R/R_{25} (bottom plot). The points and error bars are the mean and 1σ dispersion of 0.5 kpc bins. In the case of barred galaxies, the dotted vertical line indicates the radius where the bar ends. For barred galaxies, the dotted vertical line indicates the radius where the bar ends. As expected from the mass–metallicity relation, the lowest Z_{gas} values are in NGC 0337, which has the lowest stellar mass and latest Hubble type. The most striking result is that the barred and unbarred galaxies show similarly shaped Z_{gas} profiles, which are flat or show very small negative gradients from the inner kpc out to large radii (7–10 kpc or 0.5–1.0 R_{25}) in the outer disc.

possibility that weakly interacting unbarred systems might have a flatter gradient than the corresponding isolated unbarred galaxies, but the number statistics in our subsample of VENGA galaxies are too small to draw any general conclusion.

All the spiral galaxies in our subsample exhibit remarkably flat Z_{gas} gradients, making it is difficult to find distinguishing characteristics in the gradients between the galaxies. Does the fine structure of the Z_{gas} radial profiles seen in Fig. 9 provide hints of the underlying enrichment and/or radial mixing processes that can lead to the observed globally flat Z_{gas} gradients? The effects of these processes might be detectable as small scale breaks or inflection points in the

Z_{gas} radial profile. Examples of such breaks have been observed by Roy & Walsh (1997), Scarano, Lépine & Marcon-Uchida (2011), Scarano & Lépine (2013), and Rosa et al. (2014). Pilyugin (2003) cautions that breaks observed with R_{23} diagnostics should be confirmed with other diagnostics due to the double degeneracy in Z_{gas} for a given value of R_{23} (described in Section 4.5). The Z_{gas} in most of our data is high enough that we avoid this issue. The fine structure of the Z_{gas} radial profile for the isolated barred galaxy NGC 2903 shows a positive Z_{gas} gradient in the nucleus which then flattens then inverts to a negative gradient towards the end of the bar. This pattern is seen using all the Z_{gas} diagnostics except those based on N2, which shows opposite behaviour in the gradient (see discussion in Section 5.2). The gradient then becomes flatter and smooth in the outer disc beyond the bar. The case is less clear for our other isolated barred galaxy NGC 5713 which appears to show a break in the Z_{gas} radial profile at the end of its bar using the R_{23} based diagnostics but the same break is not seen in the other diagnostics, although the scatter in R_{23} is large beyond the end of the bar. Our one weakly interacting barred spiral NGC 0337 shows a stronger negative gradient over its bar which then becomes flatter in its outer disc. None of our unbarred isolated galaxies (NGC 0628, 3938, and 4254) or unbarred interacting galaxy (NGC 5194) show any clear breaks in their Z_{gas} radial profiles beyond the inner few kpc. This fine structure, especially in NGC 2903, possibly hints at how bars can flatten Z_{gas} gradients over time, which we discuss in greater detail in Section 5.3.3.

5.3.2 Comparison of our results with other studies

Early studies based on slit spectroscopic or narrow-band imaging data (e.g. Vila-Costas & Edmunds 1992; Martin & Roy 1994; Zaritsky et al. 1994; Dutil & Roy 1999; Henry & Worthey 1999) claimed that Z_{gas} gradients are flatter in isolated barred spiral galaxies than those that are unbarred. However, these studies suffer from several caveats. They use multislit spectroscopic or narrow band photometric data of targeted bright H II regions and consequently, do not fully sample the whole galaxy from the bulge to the outer disc. Furthermore, the data from the barred and unbarred galaxies come from different studies and not observed or analysed in the same consistent manner.

Next we compare our Z_{gas} profiles to those in Rupke et al. (2010), based on multislit spectroscopy of H II regions. The study by Rupke et al. (2010) builds upon the work done by Kewley et al. (2010) by comparing Z_{gas} in 16 strongly interacting galaxies to a control sample of 11 isolated galaxies. The strongly interacting systems in this study represent major interactions/mergers as they were selected to have mass ratios close to unity (1:1 to 1:3). Rupke et al. (2010) do not give the bar type of their sample galaxies as the morphologies of the galaxies are too distorted to reliably detect a bar and assign a bar type (unbarred or barred). For their non-interacting sample, we are able to compile the bar type from the literature, using studies based on NIR images (e.g. Menéndez-Delmestre et al. 2007), CO, H I and Hα kinematics (Helfer et al. 2003; Garrido, Marcelin & Amram 2004; Hernandez et al. 2005; Hess et al. 2009; Muraoka et al. 2009). We cannot assign any bar type to the strongly interacting galaxies as they have highly disturbed morphologies. In the top row of Fig. 11, we compare N202-KD02 Z_{gas} profiles of isolated barred and unbarred galaxies in the Rupke et al. (2010) sample (two right-hand panels) and in our study (two left-hand panels). The top row of Fig. 12 repeats this comparison using the R_{23}-KK04 Z_{gas} profiles. The Z_{gas} profiles in Rupke et al. (2010) do not appear to
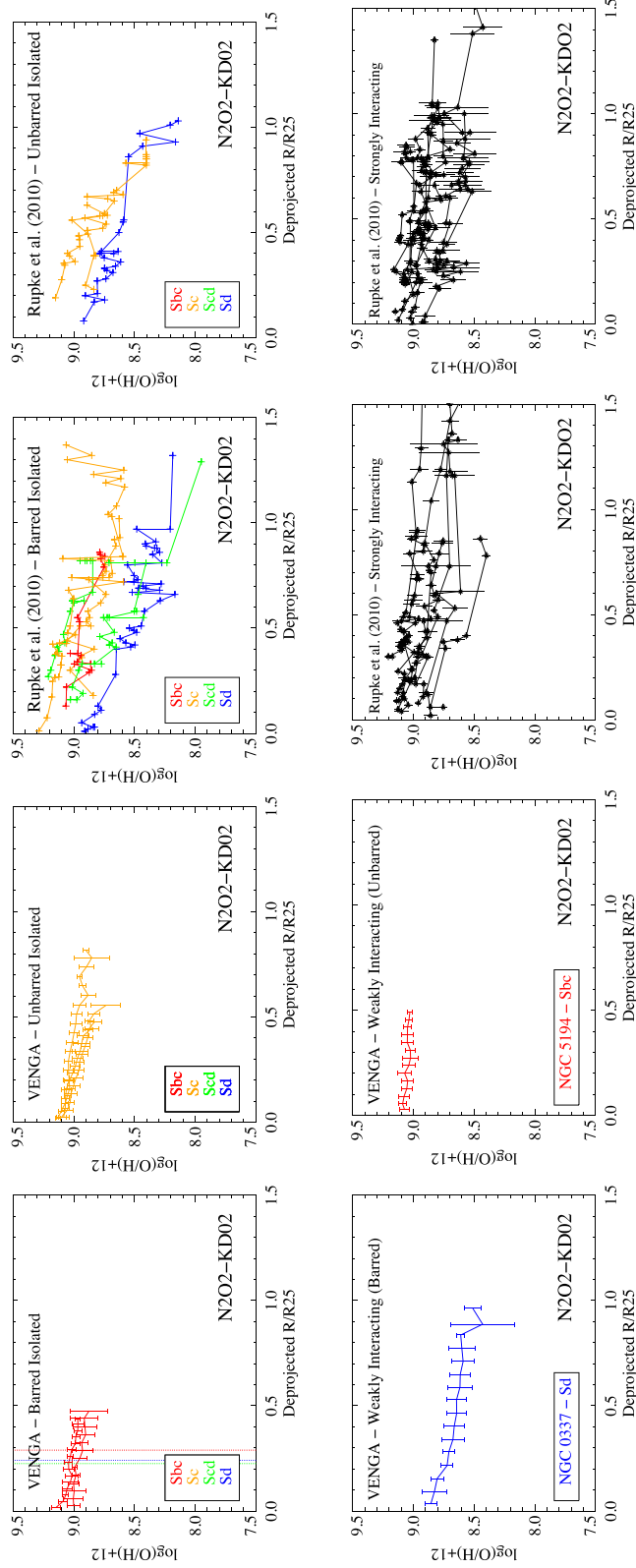
Figure 11. Radial deprojected Z_{gas} profiles based on the N202-KD02 diagnostic are shown, with the horizontal axis being the deprojected radius in units of R/R_{25}. The four left-hand panels show our study's Z_{gas} profiles for barred and unbarred galaxies, divided between isolated (top row) and interacting (bottom row) systems. The interacting systems in our study are consistent with minor interactions/mergers with mass ratios below 1:3. The four right-hand panels show Z_{gas} profiles based on multislit spectroscopic data from Rupke et al. (2010), divided between isolated (top row) and strongly interacting (bottom row) systems. These strongly interacting systems represents major interactions/mergers as they have mass ratios close to unity (1:1 to 1:3). It is striking that the VENGA-based radial Z_{gas} profiles are of much superior quality in terms of spatial sampling and scatter than the profiles based on slit-spectroscopy.
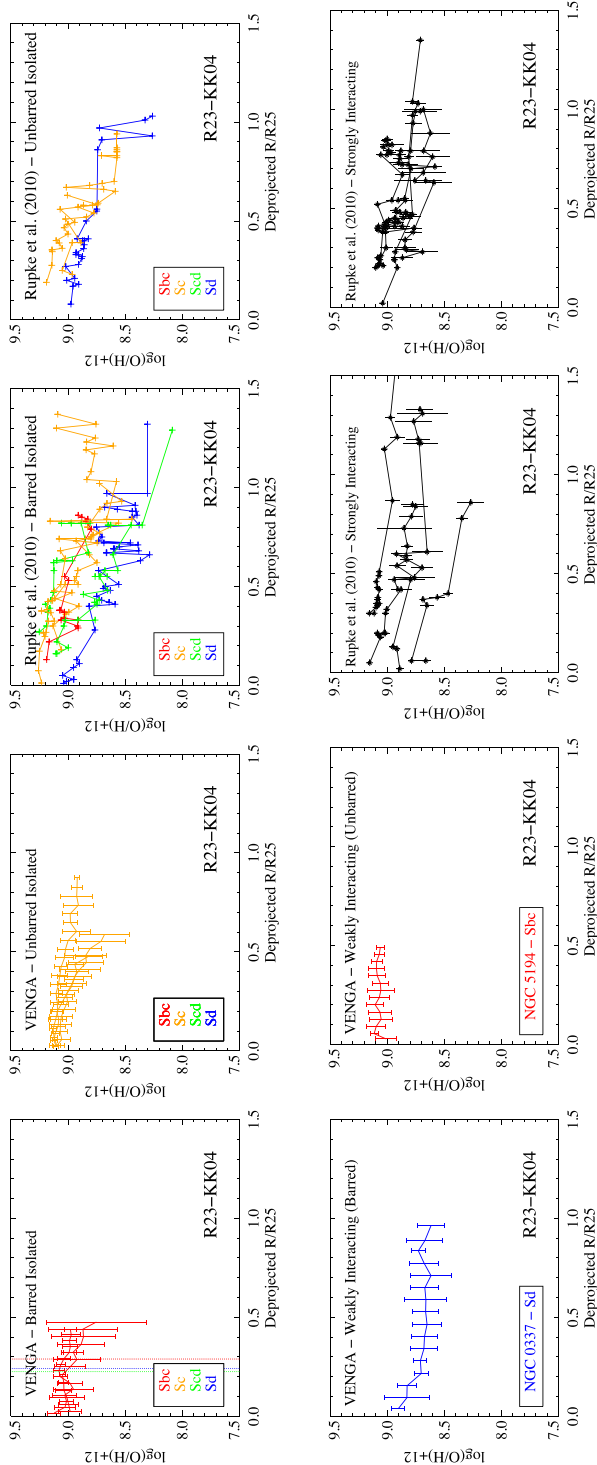
be systematically different between isolated barred and unbarred galaxies of a given Hubble type, in agreement with our results. It appears that some of the Z_{gas} profiles in Rupke et al. (2010) are steeper than the typical Z_{gas} profile we see in our data, but since the data sets have different spatial sampling, it is not possible to do a consistent comparison.

For NGC 0628, this galaxy was observed for the PINGS survey by Rosales-Ortega et al. (2011). Their radial profiles appear qualitatively similar to our own. Correcting for the assumed distance to NGC 0628, Rosales-Ortega et al. (2011) find a fibre-to-fibre Z_{gas} gradient using the R_{23}-KK04 diagnostic of -0.031 ± 0.003 dex kpc^{-1} which is nearly identical to our gradient of -0.031 ± 0.001 dex kpc^{-1}. Specifically targeting known H II regions in NGC 0628, Rosales-Ortega et al. (2011) finds a gradient of -0.044 ± 0.002 dex kpc^{-1}, slightly steeper than our value.

Finally, we compare our IFU-based results of Z_{gas} to the recent IFU studies by Sánchez et al. (2012, 2014) based on the PINGS (Rosales-Ortega et al. 2010) and CALIFA (Sánchez et al. 2011) IFU surveys. Our study extends upon the work of Sánchez et al. (2012, 2014) in several respects. As shown by Table 2, our study has a smaller sample but benefits from a higher median spatial resolution (387 pc versus 644 pc in Sánchez et al. 2012 and 985 pc in Sánchez et al. 2014), a higher spectral resolution (120 km s^{-1} at 5000 Å versus 600 km s^{-1} and 350 km s^{-1}), and the use of seven complementary Z_{gas} diagnostics. Sánchez et al. (2012) base their analyses on targeting clumpy bright H II regions in their galaxies, while our analysis uses all the spaxels in our VENGA IFU data after excluding those dominated by Seyfert or LINER gas excitations (Section 4.1), and DIG-dominated regions (Section 4.2). Sánchez et al. (2014) targets clumpy bright H II regions like Sánchez et al. (2012) but then also excludes Seyfert or LINER contaminated regions similar to our methodology. The Z_{gas} gradients reported by Sánchez et al. (2012, 2014) are derived from unweighted linear fits, similar to how we derive gradients in our sample, although the fits are limited to radii of $0.3 < r/r_e < 2.1$. We report the mean Z_{gas} gradients and 1σ uncertainties about the mean for barred versus unbarred galaxies from Sánchez et al. (2014) in Table 5. With our higher spatial and spectral resolution, and our suite of seven Z_{gas} diagnostics, we confirm the results from Sánchez et al. (2012, 2014), finding no significant difference in the Z_{gas} gradients between barred and unbarred spirals.

5.3.3 Theoretical implications of our results for bar-driven evolution

Taken at face value, our IFU-based study and the IFU studies of Sánchez et al. (2014, 2012) are finding similarly shallow Z_{gas} profiles in barred and unbarred galaxies out to a large fraction (0.5–1.0) of R_{25}. Below we discuss the implications of this result and how bars impact Z_{gas} profiles.

A large-scale stellar bar impacts Z_{gas} by driving gas inflows and outflows in different parts of the galaxy disc. Beyond the end of the stellar bar, between the corotation resonance (CR) and the outer Lindblad resonance (OLR) of the bar, gas is driven *outward* in the disc by gravitational torques (e.g. reviews by Buta & Combes 1996 and by Jogee 2006). Conversely, inside the bar, gas between the CR and the outer inner Lindblad resonances (OILR) of the bar is driven *inward* until it reaches the inner kpc region where the bulge potential tends to dominate. If a galaxy with an initially steeply negative Z_{gas} profile (where Z_{gas} falls with radius) develops a stellar bar, the bar can flatten the Z_{gas} profiles by driving gas inflow from

Figure 12. Same as for Fig. 11 but for the R_{23}-KK04 Z_{gas} diagnostic.

the bar end to the inner kpc region, and gas outflows from the bar's end to the outer disc. However, an added layer of complexity is that strong bars often induce high SFRs in the circumnuclear (inner kpc) region of spirals (e.g. Kormendy & Kennicutt 2004; Jogee et al. 2005), and this leads to an enrichment of Z_{gas}, followed by starburst-driven outflows.

The Z_{gas} profile in a present-day spiral depends on the initial Z_{gas} gradient in the early stages of galaxy formation, and the subsequent complex cumulative history of gas inflow/outflows and *in situ* SF. Therefore, it is relevant to look at cosmological simulations of barred galaxies. Cosmologically motivated simulations of disc galaxies show that bars have undergone two distinct phases of development in early and late times (Heller, Shlosman & Athanassoula 2007; Romano-Díaz et al. 2008). The first bars that formed in the first few Gyr (at $z > 2$) of a galaxy's life were induced by asymmetries in the dark matter haloes and they decayed and reformed quickly during that period, while the galaxy is growing its mass via major and minor mergers. These early transient stellar bars exist in almost all simulated galaxies, and are associated with strong radial gas flows. At later times, when the Universe was around 5–7 Gyr (e.g. $z \sim 1.5$), discs are more massive and a more stable generation of bars start to form, primarily through tidal interactions. These late-time bars are typically long lived ($\sim$5–10 Gyr), consistent with observations of bars in bright or massive galaxies out to $z \sim 1$ (Jogee et al. 2004; Sheth et al. 2008; Cameron et al. 2010).

Our empirical study finds that that present-day barred and unbarred massive spirals host similarly shallow Z_{gas} profiles. These results imply that if spirals had steeper metallicity gradient at earlier epochs, that the flattening of this gradient over time is not driven primarily by the *present-day* large-scale stellar bar. Instead, it implies that processes not directly related the *present-day* large-scale stellar bar played an important role in shaping the Z_{gas} profiles of massive spirals over their lifetime. These processes likely include gas inflows/outflows driven by *earlier* generations of transient stellar bars at $z \gg 1$, as well as gas inflows from minor mergers and tidal interactions since $z < 2$. Another layer of complexity is added by local SF activity and outflows driven by starbursts or AGN.

It is relevant to note here that observations show that minor mergers are very common at $z < 1$, being at least three times more frequent than major mergers (Jogee et al. 2009; Lotz et al. 2011). While prograde minor mergers would induce stellar bars, retrograde minor mergers are unlikely to do so, and could therefore help to flatten Z_{gas} in an unbarred spiral. Such scenarios can be tested once we have Z_{gas} profiles for large samples of barred and unbarred galaxies over $z \sim 0$ to 1.5.

5.4 Comparison of Z_{gas} gradients between low and high redshift galaxies

We explore whether Z_{gas} gradients are flattening over cosmic time by comparing our $z = 0$ results to gradients observed at higher redshifts. While all our VENGA galaxies at $z \sim 0$ show similarly shallow Z_{gas} gradients across both bared and unbarred massive spiral galaxies, our sample size is small. Do all spirals at $z \sim 0$ show similarly shallow Z_{gas} gradients? Sánchez et al. (2014), with a sample of 193 spirals, finds an average gradient with the O3N2-PP04 diagnostic of -0.16 ± 0.12 dex $(R/R_{25})^{-1}$, consistent with our value of -0.11 ± 0.13 dex $(R/R_{25})^{-1}$. The sample of 49 galaxies found in Ho et al. (2015) finds an average gradient using the N2O2-KD02 diagnostic of -0.39 ± 0.18 dex $(R/R_{25})^{-1}$, also consistent with our value of -0.34 ± 0.14 dex $(R/R_{25})^{-1}$. Bresolin & Kennicutt (2015) finds
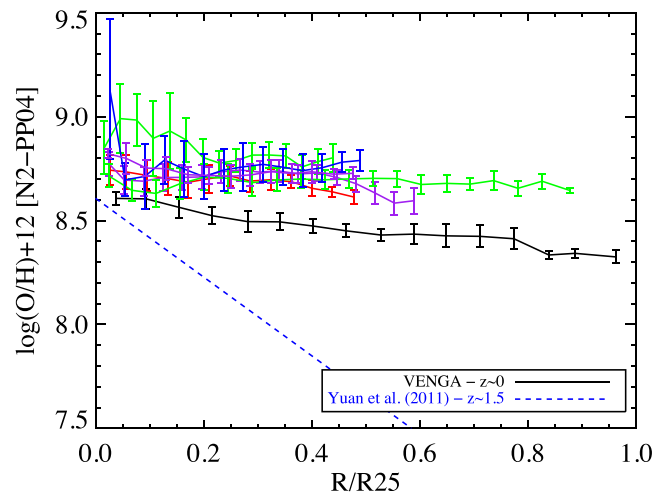

Figure 13. Radial Z_{gas} profiles in units of R/R_{25} are shown for our local ($z \sim 0$) VENGA sub-sample of spirals (solid lines), and a higher redshift ($z \sim 1.5$) gravitationally lensed disc galaxy Sp1149 (Yuan et al. 2011). For comparison in radial units of kpc, see Fig. 14. Sp1149 shows a significantly steeper gradient than our $z \sim 0$ VENGA sub-sample. These observations are consistent with the idea that Z_{gas} gradients flatten over cosmic time.

their sample of 10 low surface brightness spiral galaxies have even shallower average gradients, with -0.065 ± 0.055 dex $(R/R_{25})^{-1}$ and -0.133 ± 0.072 dex $(R/R_{25})^{-1}$ for O3N2 and N2O2 diagnostics respectively. Across all these studies we find that Z_{gas} gradients for these $z \sim 0$ spiral galaxies are at least as shallow, on average, as our own spirals. This suggests that the shallow Z_{gas} gradients we observe in our own sample are typical for most massive spirals at $z \sim 0$.

High redshift studies typically lack the spatial resolution to separate out different galactic components and excitation regions, and the effects of low spatial resolution can artificially flatten inferred Z_{gas} gradients as shown by Yuan, Kewley & Rich (2013) and Mast et al. (2014). To overcome these limitations, recent work using gravitational lensing (Yuan et al. 2011) and adaptive optics (AO) (Swinbank et al. 2012) has begun to study radial metallicity gradients at higher redshifts. Figs 13 and 14 compare the Z_{gas} gradients of our sub-sample of $z \sim 0$ VENGA spirals to two gravitationally lensed galaxies observed with AO: Sp1149 at $z \sim 1.5$ (Yuan et al. 2011) and the 'clone arc' at $z \sim 2$ (Jones et al. 2010). We use the N2-PP04 Z_{gas} diagnostic as it is common to both low and high redshift systems. The radial extent of the galactic disc changes with redshift and stellar mass so we compare the Z_{gas} gradients using the R/R_{25} scale in Fig. 13. Since some systems do not have R_{25} reported, we also compared using radius in kpc in Fig. 14.

Both higher redshift galaxies have measured dynamical masses of $\sim 2.5 \times 10^{10} M_\odot$ (Jones et al. 2010; Yuan et al. 2011). If at most ~ 20 per cent of their mass is composed of stars, the stellar mass for both galaxies would be $\leq 2 \times 10^9 M_\odot$. Therefore, the stellar masses of these two $z \sim 1.5-2.0$ galaxies are one to two orders of magnitude smaller than those of the $z \sim 0$ spirals in our sample ($1.6 \times 10^{10} M_\odot$ to $4 \times 11^{11} M_\odot$). Sp1149 at $z \sim 1.5$ (Yuan et al. 2011) has an N2-PP04 Z_{gas} gradient of -0.16 ± 0.02 dex kpc^{-1} and -1.92 ± 0.24 dex $(R/R_{25})^{-1}$ (Table 5). The 'clone arc' at $z \sim 2$ (Jones et al. 2010) has a gradient of -0.27 ± 0.05 dex kpc^{-1}. In contrast, the more massive $z \sim 0$ galaxies in our sample show much flatter N2-PP04 Z_{gas} gradients, spanning values from -0.034 to 0.003 dex kpc^{-1} and -0.57 to 0.03 dex $(R/R_{25})^{-1}$, with a mean
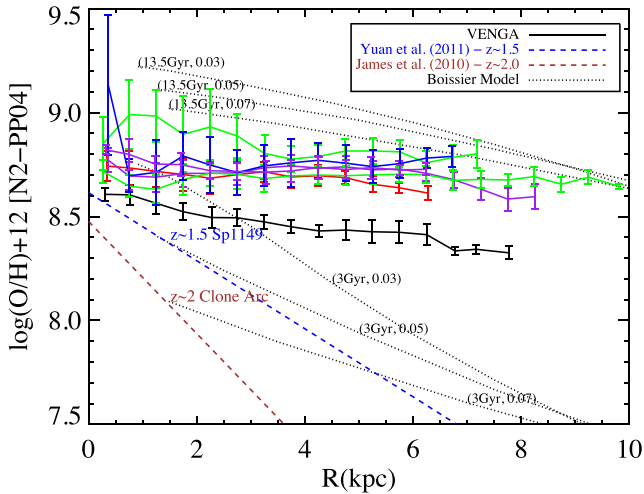
Figure 14. Comparison of the radial Z_{gas} profiles in units of kpc between VENGA galaxies at $z \sim 0$, a gravitationally lensed disc galaxy Sp1149 at $z \sim 1.5$ (Yuan et al. 2011) and the clone arc system at $z \sim 2$ (Jones et al. 2010). Both Sp1149 and the 'clone arc' shows a significantly steeper gradient than our $z \sim 0$ VENGA sub-sample. These observations are consistent with the idea that Z_{gas} gradients flatten over cosmic time. Also over-plotted are predictions from the theoretical models of Boissier & Prantzos (1999). The models at $z \sim 1.5$ (age $\sim$3 Gyr) and at $z \sim 0$ (age $\sim$13.5 Gyr) assume parameters to match Sp1149, with a circular velocity of 200 km s^{-1} and dimensionless spin parameters of 0.03, 0.05, and 0.07. The age and dimensionless spin parameters are labelled in parenthesis on the model plots.

of -0.012 ± 0.014 dex kpc^{-1} and -0.16 ± 0.19 dex $(R/R_{25})^{-1}$ (Table 5). We therefore conclude that these two lower mass galaxies (Sp1149 and the Clone Arc) at $z \sim 1.5$–2.0 have Z_{gas} profiles that are much steeper than the shallow Z_{gas} profiles exhibited by our $z \sim 0$ massive spirals. If these systems are representative of progenitor and descendant populations, then our comparisons suggest that gas phase metallicity gradients flatten over cosmic time as a galaxy grows in stellar mass. Similar results are reported by Yuan et al. (2011) who compare their data to slit based $z \sim 0$ spectroscopic data.

A few recent observations by Stott et al. (2014) and references therein report that some systems have flat Z_{gas} radial profiles at $z \sim 0.8$. If these results are representative, then they allow for the possibility that there are highly efficient processes, which can rapidly convert steep Z_{gas} profiles at $z \geq 2$ into flat profiles by $z \sim 0.8$. However, the observations by Stott et al. (2014) do not use AO, and it is possible that the flatness of the Z_{gas} profiles in their $z \sim 0.8$ systems is due to the lower spatial resolution (Yuan et al. 2013; Mast et al. 2014), despite their attempts to correct for resolution effects.

More rigorous studies of the chemical evolution of galaxies since $z \sim 2$ will require high resolution observations of Z_{gas} profiles in large samples of galaxies of different stellar masses over a range of different redshifts between $z \sim 2$ and 0. It is unclear at this stage whether the handful of existing observations over this redshift range are representative of the general population.

5.5 Comparison of Z_{gas} gradients to theoretical models

In order to explore some of the baryonic physics that shapes the metallicity profiles of galaxies, we compare different theoretical galaxy chemical evolution models to the empirical Z_{gas} profiles

(Section 5.4) of our $z \sim 0$ sample of spirals, and published Z_{gas} profiles in higher redshift $z \sim 1.5$–2.0 systems.

We start by comparing our Z_{gas} gradients to those derived by the updated Boissier model. The Boissier model was first employed by Boissier & Prantzos (1999) to simulate the chemical evolution of the Milky Way's disc, and was then generalized to other discs in Prantzos & Boissier (2000) by allowing the rotation curve and dimensionless spin parameter to scale. The scaling laws for the rotation curve and dimensionless spin parameter are deduced from ΛCDM simulations of disc formation by Mo, Mao & White (1998). In the Boissier model, a single disc is modelled as a set of independent concentric rings with no radial inflows or outflows. The stellar distribution assumes a Kroupa IMF (Kroupa 2001). For the model we compare to, the SFR law has been updated to match the empirical SFR laws found in nearby spirals (Muñoz-Mateos et al. 2011). Primordial gas infall decreases exponentially with time, with larger gas infall time-scales at greater radii. Gas accretes for a shorter amount of time in the centre than at the edge of the disc. Since this model does not include radial mixing of gas through gas inflows and outflows, it should only be considered as a model of the 'inside-out' disc formation scenario.

Fig. 14 compares the Boissier model at different ages to radial Z_{gas} profiles of our sample of $z \sim 0$ massive spirals, and the lower mass gravitationally lensed galaxies Sp1149 at $z \sim 1.5$ (Yuan et al. 2011), and the 'clone arc' at $z \sim 2$ (Jones et al. 2010) (see Section 5.4). We use models with a circular velocity of 200 km s^{-1} and dimensionless spin parameters of 0.03, 0.05, and 0.07. The Boissier models exhibit a somewhat shallower Z_{gas} gradient at $z \sim 1.5$ than Sp1149. They subsequently flatten with time from $z \sim 1.5$ to 0, but do not flatten enough to match the shallow Z_{gas} gradients in our sample of $z \sim 0$ massive spirals. This is perhaps not surprising since the Boissier models are missing important aspects of galaxy evolution and baryonic physics. They do not include the radial gas mixing via inflows and outflows, driven by bars or interactions. Furthermore, since they are not cosmological hydrodynamic simulations, they do not include galaxy mergers, cold mode gas accretion, or feedback.

Next we compare the same observations to more realistic simulations of the assembly and chemical evolution of galaxies, which are cosmologically motivated, include more baryonic physics, and allow for radial inflow/outflow of gas. We consider simulated disc galaxies in two different set of models: the MUGS models from Pilkington et al. (2012), and the MaGICC models (Gibson et al. 2013). The first set of models from Pilkington et al. (2012), called MUGS, uses the gravitational *N*-body and SPH code Gasoline (Wadsley, Stadel & Quinn 2004) to simulate 16 isolated disc galaxies that are randomly drawn from a 50 h^{-1} Mpc ΛCDM simulation with WMAP3 cosmology. Each galaxy is re-simulated at much higher resolution (Klypin et al. 2001). Pilkington et al. (2012) selects four galaxies with the most prominent discs, including g1536 and g15784. The MUGS model includes star formation and SNe feedback implemented with the 'blast wave formalism' described in (Stinson et al. 2006), heating by a background UV field, gas cooling derived using Cloudy (Ferland et al. 1998), and gas enrichment via Type II and Ia SNe assuming a Kroupa IMF.

A similar Gasoline code called MaGICC (Brook et al. 2012), is used to also simulate g1536 and g15784 (Gibson et al. 2013) using 'enhanced' feedback with about double the energy per SN in MaGICC (10^{51} erg) heating the ISM, compared to MUGS (4×10^{50} erg). MaGICC also includes radiative energy feedback from massive stars shortly before they go SN, and a Chabrier (2001) IMF, forming larger numbers of high mass stars than the Kroupa IMF in MUGS. Both simulated disc galaxies (g1536 and g15784)

are selected to be isolated and have somewhat quiescent assembly histories (Gibson et al. 2013) which are identical in both MUGS and MaGICC.

The stellar mass of the galaxies in MaGICC grow ∼4 × in stellar mass from $z = 1.5$ to 0 (∼10^8 to $4.5 \times 10^8\,M_\odot$ for g1536 and ∼10^9 to $4.2 \times 10^9\,M_\odot$ for g15784; Obreja et al. 2014) while the final stellar masses of the MUGS galaxies are up to two orders of magnitude larger ($6.0 \times 10^{10}\,M_\odot$ for g1536 and $1.1 \times 10^{11}\,M_\odot$ for g15784; Stinson et al. 2010). Fig. 15 shows how the $Z_{\rm gas}$ gradients for g1536 and g15784 simulated in both MUGS and MaGICC evolve from redshift 1.5 to 0, and compares them to our sample of $z \sim 0$ massive spirals, and the lower mass galaxies Sp1149 at $z \sim 1.5$ (Yuan et al. 2011), and the 'clone arc' at $z \sim 2$ (Jones et al. 2010) (see Section 5.4). It is clear from Fig. 15, that the primary difference in $Z_{\rm gas}$ gradients for these simulations depends on the type of feedback being used, and less on which specific disc galaxy (g1536 or g15784) is being simulated. MaGICC, with its 'enhanced' feedback, drives stronger radial mixing and more numerous outflows, so that at redshift $z \sim 1.5$ MaGICC has higher $Z_{\rm gas}$ and flatter gradients than MUGS. The $Z_{\rm gas}$ gradients in MaGICC are already so flat by $z \sim 1.5$ that they do not show much evolution or extra flattening from redshift 1.5 to 0 (Gibson et al. 2013). The galaxies in the MUGS simulation have more 'conventional' feedback and their $Z_{\rm gas}$ gradients start out strongly negative at $z \sim 1.5$ and flatten significantly between redshift 1.5 and 0 (Pilkington et al. 2012).

The simulations MUGS and MaGICC imply that the strength of the feedback can significantly affect the evolution of $Z_{\rm gas}$ gradients (Gibson et al. 2013). Although these comparisons between simulations and data are very preliminary, 'conventional' feedback used in MUGS results are in much better agreement with our sample of $z \sim 0$ massive spirals, Sp1149 at $z \sim 1.5$ (Yuan et al. 2011), and the 'clone arc' at $z \sim 2$ (Jones et al. 2010) in terms of the absolute value of $Z_{\rm gas}$, the shape of the $Z_{\rm gas}$ profiles, and the evolution in stellar masses. However, we note that the interval $z \sim 1.5$ to 0 cover a large cosmic interval of ∼10 Gyr and we need a finer grid of theoretical and empirical profiles at different redshifts over this interval to further constrain the models and the rate at which $Z_{\rm gas}$ gradients are flattened.

6 SUMMARY AND CONCLUSIONS

We have presented a high resolution study of the excitation conditions and metallicity ($Z_{\rm gas}$) of ionized gas in a sample of eight nearby barred and unbarred spiral galaxies drawn from the VENGA IFU survey. Compared to other integral field spectroscopy studies of spirals, our study benefits from a high spatial resolution (median ∼387 pc), a large spatial coverage of the galaxy (from the bulge to the outer disc), broad wavelength range (3600–6800 Å), high spectral resolution (∼120 km s^{-1} at 5000 Å), and the use of a full suite seven $Z_{\rm gas}$ diagnostics (Table 2). The combination of spatial coverage and resolution allows us to resolve individual galactic components, such as the bulge, primary stellar bar, outer disc, and separate regions of widely different excitation (e.g. H II regions, spiral arms, starburst or AGN driven outflows, diffuse ionized gas, etc.). Our results are summarized below.

(1) *Distribution of gas with excitation conditions typical of Seyfert, LINER, and star-forming regions.* We use excitation diagnostic diagrams to separate spaxels hosting gas whose excitations conditions are indicative of a hard UV radiation field or shocks (Seyfert or LINERS), and photoionization by massive stars. We also develop a procedure to identify spaxels dominated by diffuse
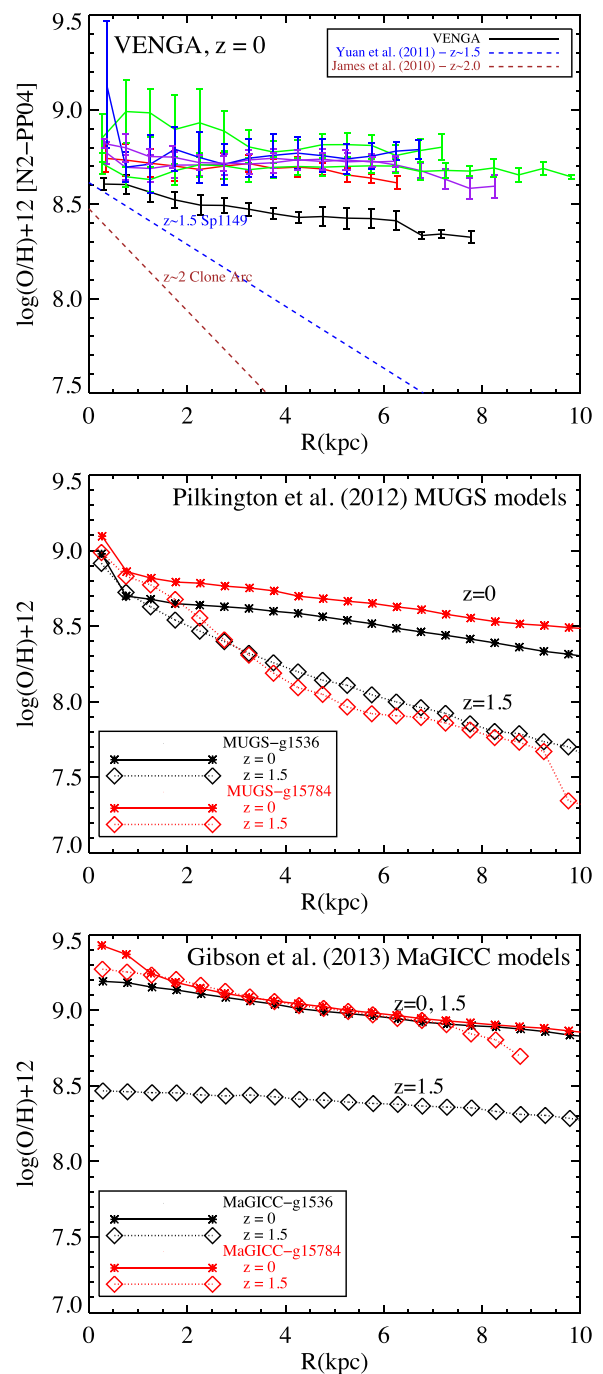
Figure 15. The radial $Z_{\rm gas}$ profiles in units of kpc are shown for our local $z \sim 0$ VENGA sub-sample, the higher redshift $z \sim 1.5$ gravitationally lensed disc galaxy Sp1149 (Yuan et al. 2011), and the $z \sim 2$ clone arc (Jones et al. 2010) (top); and for the $z = 0$ and $z = 1.5$ MUGS (middle) and MaGICC (bottom) models for the simulated disc galaxies g1536 and g15784 (Pilkington et al. 2012; Gibson et al. 2013). For the simulations, the MUGS results are in much better agreement than the MaGICC results with the evolution from high to low redshift in both the absolute value and gradients of $Z_{\rm gas}$, with what we see when comparing the flat gradients in our VENGA sub-sample to the strongly negative gradients seen at high redshift. MaGICC includes 'enhanced' feedback which drives stronger radial mixing and more numerous outflows to flatten $Z_{\rm gas}$ gradients by $z \sim 1.5$ with only a slight flattening from $z \sim 1.5$ to 0, while MUGS has more 'conventional' feedback prescriptions that appear to better match the physics driving the observed evolution of $Z_{\rm gas}$ gradients from $z \sim 1.5$ to 0 in spiral galaxies.

ionized gas (DIG), and to correct for the contribution of DIG to the Hα flux in other spaxels. While it is conventionally assumed that LINERs are caused by central starburst-driven outflows or low luminosity AGN in the nuclear regions, we find that LINER-type excitations are present at large projected distances (3–10 kpc) from the centre, and tend to be associated with DIG (Fig. 4).

(2) *Spatially resolved maps of q, SFR, and Z_{gas}.* After excluding spaxels dominated by Seyfert, LINER, and DIG, we produce accurate high resolution maps of the ionization parameter, q, the star formation rate (SFR), and seven Z_{gas} diagnostics based on the R23, N202, O3N2, and N2 metallicity indicators (Fig. 6). The distribution of q and SFR are qualitatively similar in many galaxies. However, while the average Σ_{SFR} falls by over an order of magnitude (e.g. from 0.1 to below 0.01 or from 0.01 to below 0.001 $M_{\odot}$ yr^{-1} kpc^{-2}), the average value of q typically varies by no more than a factor of 3 (e.g. from 6.95 to 7.40 dex, corresponding to 0.8 to 3 times 10^7 cm s^{-1}) (Fig. 7).

(3) *Comparison of different Z_{gas} diagnostics.* We explored how the absolute values of Z_{gas} vary between the seven Z_{gas} diagnostics (Table 4). (i) The three R_{23} Z_{gas} diagnostics (R_{23}-KK04, R_{23}-M91, R_{23}-Z94) based on the ([O III]/Hβ)/([N II]/Hα) ratios show similar Z_{gas} profiles and yield absolute values that agree within 0.1–0.2 dex; (ii) N2O2-KD02 (based on the [N II]/[O II] line ratio) gives Z_{gas} values similar to the R_{23} diagnostics, but shows a lower scatter. This may be related to the relative insensitivity of [N II]/[O II] to variations in q. (iii) O3N2-PP04 (based on the [N II]/[Hα] and [O III]/[Hβ] line ratios) gives a Z_{gas} that is systematically lower by 0.2–0.3 dex compared to the R_{23} diagnostics; (iv) N2-D02 and N2-PP04 (based on the [N II]/Hα ratio) yield a Z_{gas} that is systematically lower, by as much as 0.4 dex, compared to the R_{23} diagnostics. Furthermore, in the inner 2 kpc of some of our galaxies, the radial gradients in Z_{gas} given by N2-D02 and N2-PP04 can *be opposite to those* given by other diagnostics. Caution should therefore be exerted in using the N2-D02 and N2-PP04 Z_{gas} diagnostics.

(4) *Comparison of Z_{gas} profiles of isolated barred and unbarred galaxies.* The maps (Fig. 6) and radial profiles (Fig. 9) of q and Z_{gas} are of much higher quality in terms of spatial resolution and sampling than most other maps published to date. We find that isolated barred and unbarred spirals galaxies exhibit similarly shallow Z_{gas} profiles from the inner kpc out to large radii (7–10 kpc or 0.5–1.0R_{25}) in the outer disc. Specifically, with the N2O2-KD02 Z_{gas} diagnostic, the gradients are -0.44 ± 0.13 and -0.33 ± 0.01 dex $(R/R_{25})^{-1}$, respectively, for isolated unbarred and isolated barred spirals (Table 5). Our result on the similar Z_{gas} gradients in isolated barred and unbarred galaxies contradicts earlier claims based on slit spectroscopy, but agrees with recent IFU studies by Sánchez et al. (2012, 2014). If spirals had steeper metallicity gradient at earlier epochs, then our result implies that the flattening of this gradient over time is not driven primarily by the present-day bar. Instead, the evolution in the Z_{gas} profile is likely shaped by the cumulative history of gas inflows/outflows driven by *earlier* generations of transient stellar bars at $z \gg 1$, as well as gas inflows from minor mergers and tidal interactions since $z < 2$. Another layer of complexity is added by local SF activity and outflows driven by starbursts or AGN. We do not have a large enough sample to do a full comparison of isolated and interacting galaxies, but we note that the only weakly interacting unbarred galaxy in our sample shows a tantalizing hint of having a shallower gradient (-0.09 ± 0.01 dex $(R/R_{25})^{-1}$; Table 5) than unbarred isolated spirals.

(5) *Comparison of Z_{gas} gradients At low and high redshift in data and models.* The Z_{gas} gradients in our $z \sim 0$ massive spirals are markedly shallower, by ~ 0.2 dex kpc^{-1}, compared to published gradients for lensed lower mass galaxies at redshifts $z \sim 1.5$–2.0

(Figs 13 and 14) If these systems are representative of progenitor and descendant populations, then our comparisons suggest that gas phase metallicity gradients flatten over cosmic time as a galaxy grows in stellar mass. Simple non-cosmological theoretical models (e.g. Boissier & Prantzos 1999) that mimic an inside–out disc formation scenario through gas accretion, but do not include radial mixing, fail to provide a good match to the low or high redshift data (Fig. 14). More realistic cosmologically motivated hydrodynamical simulations (e.g. Pilkington et al. 2012; Gibson et al. 2013) that include more baryonic physics, and allow for radial inflow/outflow of gas appear to better match the data, but are highly sensitive to the adopted stellar feedback prescription (Fig. 15). It appears that the MUGS simulations with 'conventional' feedback are in better agreement than the MaGICC simulations with 'enhanced' feedback with the data in terms of the evolution of Z_{gas} values, Z_{gas} gradients, and stellar masses. However, we caution that general conclusions on the evolution of Z_{gas} profiles since $z < 2$ will require high resolution observations of Z_{gas} profiles in large samples of galaxies of different stellar masses at different redshifts between $z \sim 2$ to 0, as well as finer grids of theoretical predictions. It is unclear at this stage whether the handful of existing observations at $z > 1$ are representative of the general population at these epochs.

REFERENCES

Adams J. J. et al., 2011, ApJS, 192, 5
Alam S. et al., 2015, ApJS, 219, 12
Allen M. G., Groves B. A., Dopita M. A., Sutherland R. S., Kewley L. J., 2008, ApJS, 178, 20
Antonucci R. R. J., Miller J. S., 1985, ApJ, 297, 621
Baldwin J. A., Phillips M. M., Terlevich R., 1981, PASP, 93, 5
Belfiore F. et al., 2015, MNRAS, 449, 867
Blanc G. A., Heiderman A., Gebhardt K., Evans N. J., II, Adams J., 2009, ApJ, 704, 842
Blanc G. A. et al., 2013a, AJ, 145, 138
Blanc G. A. et al., 2013b, ApJ, 764, 117
Blanc G. A., Kewley L., Vogt F. P. A., Dopita M. A., 2015, ApJ, 798, 99
Boissier S., Prantzos N., 1999, MNRAS, 307, 857
Bresolin F., Kennicutt R. C., 2015, MNRAS, 454, 3664
Brook C. B., Stinson G., Gibson B. K., Wadsley J., Quinn T., 2012, MNRAS, 424, 1275
Brooks A. M., Governato F., Booth C. M., Willman B., Gardner J. P., Wadsley J., Stinson G., Quinn T., 2007, ApJ, 655, L17
Buta R., Combes F., 1996, Fundam. Cosm. Phys., 17, 95
Cameron E. et al., 2010, MNRAS, 409, 346
Cappellari M., Emsellem E., 2004, PASP, 116, 138
Catalán-Torrecilla C. et al., 2015, A&A, 584, A87
Chabrier G., 2001, ApJ, 554, 1274
Cole S., Lacey C. G., Baugh C. M., Frenk C. S., 2000, MNRAS, 319, 168
Conselice C. J., 2009, MNRAS, 399, L16
Considère S., Coziol R., Contini T., Davoust E., 2000, A&A, 356, 89
Dale D. A., Helou G., 2002, ApJ, 576, 159
Davé R., Finlator K., Oppenheimer B. D., 2011, MNRAS, 416, 1354
Davies R. L., Rich J. A., Kewley L. J., Dopita M. A., 2014, MNRAS, 439, 3835
de Vaucouleurs G., de Vaucouleurs A., Corwin Jr. H. G., Buta R. J., Paturel G., Fouqué P., 1991, Third Reference Catalogue of Bright Galaxies.

Volume I: Explanations and references. Volume II: Data for galaxies between 0^h and 12^h. Volume III: Data for galaxies between 12^h and 24^h

Dekel A., Birnboim Y., 2006, MNRAS, 368, 2

Dekel A. et al., 2009b, Nature, 457, 451

Dekel A., Sari R., Ceverino D., 2009a, ApJ, 703, 785

Denicoló G., Terlevich R., Terlevich E., 2002, MNRAS, 330, 69

Diaz A. I., Terlevich E., Vilchez J. M., Pagel B. E. J., Edmunds M. G., 1991, MNRAS, 253, 245

Dong X. Y., De Robertis M. M., 2006, AJ, 131, 1236

Dopita M. A., Evans I. N., 1986, ApJ, 307, 431

Dopita M. A., Kewley L. J., Heisler C. A., Sutherland R. S., 2000, ApJ, 542, 224

Dors O. L., Jr, Copetti M. V. F., 2005, A&A, 437, 837

Dors O. L., Jr, Krabbe A., Hägele G. F., Pérez-Montero E., 2011, MNRAS, 415, 3616

Drozdovsky I. O., Karachentsev I. D., 2000, A&AS, 142, 425

Dutil Y., Roy J. R., 1999, ApJ, 516, 62

Edmunds M. G., Pagel B. E. J., 1984, MNRAS, 211, 507

Ellison S. L., Patton D. R., Simard L., McConnachie A. W., 2008, AJ, 135, 1877

Erwin P., 2005, MNRAS, 364, 283

Evans I. N., Ford H. C., Kinney A. L., Antonucci R. R. J., Armus L., Caganoff S., 1991, ApJ, 369, L27

Farage C. L., McGregor P. J., Dopita M. A., Bicknell G. V., 2010, ApJ, 724, 267

Faucher-Giguère C. A., Kereš D., Ma C. P., 2011, MNRAS, 417, 2982

Ferland G. J., Korista K. T., Verner D. A., Ferguson J. W., Kingdon J. B., Verner E. M., 1998, PASP, 110, 761

Fisher D. B., Drory N., 2008, AJ, 136, 773

Florido E., Pérez I., Zurita A., Sánchez-Blázquez P., 2012, A&A, 543, A150

Freitas-Lemes P., Rodrigues I., Dors O. L., Faúndez-Abans M., Pérez-Montero E., 2014, MNRAS, 441, 1086

Garrido O., Marcelin M., Amram P., 2004, MNRAS, 349, 225

Gibson B. K., Pilkington K., Brook C. B., Stinson G. S., Bailin J., 2013, A&A, 554, A47

Giovanelli R. et al., 2005, AJ, 130, 2598

Greenawalt B., Walterbos R. A. M., Braun R., 1997, ApJ, 483, 666

Haffner L. M. et al., 2009, Rev. Mod. Phys., 81, 969

Hägele G. F., Díaz Á. I., Terlevich E., Terlevich R., Pérez-Montero E., Cardaci M. V., 2008, MNRAS, 383, 209

Helfer T. T., Thornley M. D., Regan M. W., Wong T., Sheth K., Vogel S. N., Blitz L., Bock D. C. J., 2003, ApJS, 145, 259

Heller C. H., Shlosman I., Athanassoula E., 2007, ApJ, 671, 226

Henry R. B. C., Worthey G., 1999, PASP, 111, 919

Hernandez O., Carignan C., Amram P., Chemin L., Daigle O., 2005, MNRAS, 360, 1201

Hernquist L., Mihos J. C., 1995, ApJ, 448, 41

Herrmann K. A., Ciardullo R., Feldmeier J. J., Vinciguerra M., 2008, ApJ, 683, 630

Hess K. M., Pisano D. J., Wilcots E. M., Chengalur J. N., 2009, ApJ, 699, 76

Hill G. J. et al., 2008, Proc. SPIE, 7014, 701470

Ho I. T., Kudritzki R. P., Kewley L. J., Zahid H. J., Dopita M. A., Bresolin F., Rupke D. S. N., 2015, MNRAS, 448, 2030

Hoopes C. G., Walterbos R. A. M., 2003, ApJ, 586, 902

Jogee S., 2006, in Alloin D., ed., Lecture Notes in Physics, Vol. 693, Physics of Active Galactic Nuclei at all Scales. Springer-Verlag, Berlin, p. 143

Jogee S. et al., 2004, ApJ, 615, L105

Jogee S., Scoville N., Kenney J. D. P., 2005, ApJ, 630, 837

Jogee S. et al., 2009, ApJ, 697, 1971

Jones T., Ellis R., Jullo E., Richard J., 2010, ApJ, 725, L176

Kennicutt R. C., Evans N. J., 2012, ARA&A, 50, 531

Kennicutt R. C., Jr, 1998, ARA&A, 36, 189

Kennicutt R. C., Jr, Bresolin F., Garnett D. R., 2003, ApJ, 591, 801

Kennicutt R. C. et al., 2011, PASP, 123, 1347

Kereš D., Katz N., Weinberg D. H., Davé R., 2005, MNRAS, 363, 2

Kereš D., Katz N., Fardal M., Davé R., Weinberg D. H., 2009, MNRAS, 395, 160

Kewley L. J., Dopita M. A., 2002, ApJS, 142, 35

Kewley L. J., Ellison S. L., 2008, ApJ, 681, 1183

Kewley L. J., Dopita M. A., Sutherland R. S., Heisler C. A., Trevena J., 2001, ApJ, 556, 121

Kewley L. J., Geller M. J., Jansen R. A., 2004, AJ, 127, 2002

Kewley L. J., Groves B., Kauffmann G., Heckman T., 2006, MNRAS, 372, 961

Kewley L. J., Rupke D., Zahid H. J., Geller M. J., Barton E. J., 2010, ApJ, 721, L48

Kewley L. J., Dopita M. A., Leitherer C., Davé R., Yuan T., Allen M., Groves B., Sutherland R., 2013, ApJ, 774, 100

Klypin A., Kravtsov A. V., Bullock J. S., Primack J. R., 2001, ApJ, 554, 903

Kobulnicky H. A., Kewley L. J., 2004, ApJ, 617, 240

Kobulnicky H. A., Kennicutt R. C., Jr, Pizagno J. L., 1999, ApJ, 514, 544

Kormendy J., Kennicutt R. C., Jr, 2004, ARA&A, 42, 603

Krabbe A. C., Pastoriza M. G., Winge C., Rodrigues I., Ferreiro D. L., 2008, MNRAS, 389, 1593

Krabbe A. C., Pastoriza M. G., Winge C., Rodrigues I., Dors O. L., Ferreiro D. L., 2011, MNRAS, 416, 38

Kroupa P., 2001, MNRAS, 322, 231

Laine S., Shlosman I., Knapen J. H., Peletier R. F., 2002, ApJ, 567, 97

Lara-López M. A. et al., 2010, A&A, 521, L53

Laurikainen E., Salo H., 2002, MNRAS, 337, 1118

Lee H., Skillman E. D., Cannon J. M., Jackson D. C., Gehrz R. D., Polomski E. F., Woodward C. E., 2006, ApJ, 647, 970

López-Sánchez Á. R., Dopita M. A., Kewley L. J., Zahid H. J., Nicholls D. C., Scharwächter J., 2012, MNRAS, 426, 2630

Lopez-Sanchez A. R., Esteban C., 2010, preprint (arXiv:e-prints)

Lotz J. M., Jonsson P., Cox T. J., Croton D., Primack J. R., Somerville R. S., Stewart K., 2011, ApJ, 742, 103

McCall M. L., Rybski P. M., Shields G. A., 1985, ApJS, 57, 1

McGaugh S. S., 1991, ApJ, 380, 140

Macchetto F., Capetti A., Sparks W. B., Axon D. J., Boksenberg A., 1994, ApJ, 435, L15

Madsen G. J., Reynolds R. J., Haffner L. M., 2006, ApJ, 652, 401

Mannucci F., Cresci G., Maiolino R., Marconi A., Gnerucci A., 2010, MNRAS, 408, 2115

Marinova I., Jogee S., 2007, ApJ, 659, 1176

Martin C. L., 2000, Rev. Mex. Astron. Astrofis., 27, 270

Martin P., Roy J. R., 1994, ApJ, 424, 599

Mast D. et al., 2014, A&A, 561, A129

Mathis J. S., 2000, ApJ, 544, 347

Menéndez-Delmestre K., Sheth K., Schinnerer E., Jarrett T. H., Scoville N. Z., 2007, ApJ, 657, 790

Mo H. J., Mao S., White S. D. M., 1998, MNRAS, 295, 319

Moustakas J., Kennicutt R. C., Jr, Tremonti C. A., Dale D. A., Smith J. D. T., Calzetti D., 2010, ApJS, 190, 233

Muñoz-Mateos J. C., Boissier S., Gil de Paz A., Zamorano J., Kennicutt R. C., Jr, Moustakas J., Prantzos N., Gallego J., 2011, ApJ, 731, 10

Muraoka K. et al., 2009, ApJ, 706, 1213

Obreja A., Brook C. B., Stinson G., Domínguez-Tenreiro R., Gibson B. K., Silva L., Granato G. L., 2014, MNRAS, 442, 1794

Oh K., Sarzi M., Schawinski K., Yi S. K., 2011, ApJS, 195, 13

Oppenheimer B. D., Davé R., Kereš D., Fardal M., Katz N., Kollmeier J. A., Weinberg D. H., 2010, MNRAS, 406, 2325

Osterbrock D. E., Ferland G. J., 2006, Astrophysics of Gaseous Nebulae and Active Galactic Nuclei. Univ. Sci. Books, CA

Pagel B. E. J., Edmunds M. G., Blackwell D. E., Chun M. S., Smith G., 1979, MNRAS, 189, 95

Pérez-Montero E., 2014, MNRAS, 441, 2663

Pettini M., Pagel B. E. J., 2004, MNRAS, 348, L59

Pilkington K. et al., 2012, A&A, 540, A56

Pilyugin L. S., 2003, A&A, 397, 109

Pilyugin L. S., Thuan T. X., 2005, ApJ, 631, 231

Poznanski D. et al., 2009, ApJ, 694, 1067

Prantzos N., Boissier S., 2000, MNRAS, 313, 338

Rahman N. et al., 2011, ApJ, 730, 72

Rich J. A., Dopita M. A., Kewley L. J., Rupke D. S. N., 2010, ApJ, 721, 505

Rich J. A., Kewley L. J., Dopita M. A., 2011, ApJ, 734, 87

Rich J. A., Torrey P., Kewley L. J., Dopita M. A., Rupke D. S. N., 2012, ApJ, 753, 5

Riffel R. A., Vale T. B., Storchi-Bergmann T., McGregor P. J., 2014, MNRAS, 442, 656

Romano-Díaz E., Shlosman I., Heller C., Hoffman Y., 2008, ApJ, 687, L13

Rosa D. A., Dors O. L., Krabbe A. C., Hägele G. F., Cardaci M. V., Pastoriza M. G., Rodrigues I., Winge C., 2014, MNRAS, 444, 2005

Rosales-Ortega F. F., Kennicutt R. C., Sanchez S. F., Diaz A. I., Pasquali A., Johnson B. D., Hao C. N., 2010, MNRAS, 405, 735

Rosales-Ortega F. F., Díaz A. I., Kennicutt R. C., Sánchez S. F., 2011, MNRAS, 415, 2439

Roy J. R., Walsh J. R., 1997, MNRAS, 288, 715

Rupke D. S. N., Kewley L. J., Chien L. H., 2010, ApJ, 723, 1255

Sánchez S. F. et al., 2011, in Zapatero Osorio M. R., Gorgas J., Maíz Apellániz J., Pardo J. R., Gil de Paz A., eds, Highlights of Spanish Astrophysics VI. p. 339

Sánchez S. F. et al., 2012, A&A, 546, A2

Sánchez S. F. et al., 2013, A&A, 554, A58

Sánchez S. F. et al., 2014, A&A, 563, A49

Sánchez S. F. et al., 2015, A&A, 574, A47

Sánchez-Blázquez P. et al., 2006, MNRAS, 371, 703

Sandage A., Bedke J., 1994, The Carnegie Atlas of Galaxies. Volumes I, II. Carnegie Inst. Washington, Washington, DC

Sanders D. B., Mazzarella J. M., Kim D. C., Surace J. A., Soifer B. T., 2003, AJ, 126, 1607

Sarzi M. et al., 2006, MNRAS, 366, 1151

Scarano S., Lépine J. R. D., 2013, MNRAS, 428, 625

Scarano S., Jr, Lépine J. R. D., Marcon-Uchida M. M., 2011, MNRAS, 412, 1741

Schlegel D. J., Finkbeiner D. P., Davis M., 1998, ApJ, 500, 525

Shaver P. A., McGee R. X., Newton L. M., Danks A. C., Pottasch S. R., 1983, MNRAS, 204, 53

Sheth K. et al., 2008, ApJ, 675, 1141

Shields G. A., 1990, ARA&A, 28, 525

Singh R. et al., 2013, A&A, 558, A43

Somerville R. S., Primack J. R., 1999, MNRAS, 310, 1087

Springel V., Di Matteo T., Hernquist L., 2005, MNRAS, 361, 776

Springob C. M., Masters K. L., Haynes M. P., Giovanelli R., Marinoni C., 2007, ApJS, 172, 599

Stinson G., Seth A., Katz N., Wadsley J., Governato F., Quinn T., 2006, MNRAS, 373, 1074

Stinson G. S., Bailin J., Couchman H., Wadsley J., Shen S., Nickerson S., Brook C., Quinn T., 2010, MNRAS, 408, 812

Stott J. P. et al., 2014, MNRAS, 443, 2695

Swinbank A. M., Sobral D., Smail I., Geach J. E., Best P. N., McCarthy I. G., Crain R. A., Theuns T., 2012, MNRAS, 426, 935

Torres-Flores S., Scarano S., Mendes de Oliveira C., de Mello D. F., Amram P., Plana H., 2014, MNRAS, 438, 1894

Tremonti C. A. et al., 2004, ApJ, 613, 898

Tully R. B., 1988, Nearby Galaxies Catalog. Cambridge Univ. Press, New York

Tully R. B., Shaya E. J., Karachentsev I. D., Courtois H. M., Kocevski D. D., Rizzi L., Peel A., 2008, ApJ, 676, 184

Veilleux S., Osterbrock D. E., 1987, ApJS, 63, 295

Vila-Costas M. B., Edmunds M. G., 1992, MNRAS, 259, 121

Wadsley J. W., Stadel J., Quinn T., 2004, New Astron., 9, 137

Walter F., Brinks E., de Blok W. J. G., Bigiel F., Kennicutt R. C., Jr, Thornley M. D., Leroy A., 2008, AJ, 136, 2563

Walterbos R. A. M., 1998, PASA, 15, 99

Weinzirl T., Jogee S., Khochfar S., Burkert A., Kormendy J., 2009, ApJ, 696, 411

Wood K., Hill A. S., Joung M. R., Mac Low M. M., Benjamin R. A., Haffner L. M., Reynolds R. J., Madsen G. J., 2010, ApJ, 721, 1397

Wuyts E. et al., 2014, ApJ, 789, L40

Yuan T. T., Kewley L. J., Swinbank A. M., Richard J., Livermore R. C., 2011, ApJ, 732, L14

Yuan T. T., Kewley L. J., Swinbank A. M., Richard J., 2012, ApJ, 759, 66

Yuan T. T., Kewley L. J., Rich J., 2013, ApJ, 767, 106

Zaritsky D., Kennicutt R. C., Jr, Huchra J. P., 1994, ApJ, 420, 87

Zhao Y., Gao Y., Gu Q., 2010, ApJ, 710, 663

APPENDIX A: HOW IONIZATION PARAMETER q IS DETERMINED ITERATIVELY FOR THE R_{23}-KK04 DIAGNOSTIC – METHOD 2

The iterative determination of q is based off of the R_{23} Z_{gas} diagnostic in Kobulnicky & Kewley (2004), and this procedure is detailed in appendix A2.1 of Kewley & Ellison (2008). R_{23} is dependent on q (see Fig. 8 on the top left) so we iterate to converge on a Z_{gas} and q for this Z_{gas} diagnostic. First, an initial Z_{gas} is assumed by breaking the double valued degeneracy of R_{23} using [N II]/[O II]. Breaking the double valued degeneracy is described in detail in appendix A1 of Kewley & Ellison (2008), in summary:

$$\text{upper branch}: \quad \log([\text{N II}]/[\text{O II}]) \geq -1.2 \tag{A1}$$

$$\text{lower branch}: \quad \log([\text{N II}]/[\text{O II}]) < -1.2 \tag{A2}$$

For each branch, the code assumes an initial Z_{gas} of:

$$\text{upper branch}: \quad \text{initial } \log(\text{O/H}) + 12 = 8.7 \tag{A3}$$

$$\text{lower branch}: \quad \text{initial } \log(\text{O/H}) + 12 = 8.2 \tag{A4}$$

This first initial guess for Z_{gas} and [O III]/[O II] is used to make an initial guess at q using the following (see equation 13 in Kobulnicky & Kewley 2004):

$$y = \log([\text{O III}]/[\text{O II}]) \tag{A5}$$

$$Z = \text{initial } \log(\text{O/H}) + 12 \tag{A6}$$

$$\log q =$$
$$\frac{32.81 - 1.153y^2 + Z(-3.396 - 0.025y + 0.1444y^2)}{4.603 - 0.3119y - 0.163y^2 + Z(-0.48 + 0.0271y + 0.02037y^2)} \tag{A7}$$

With the initial guess for Z_{gas} and q for each fibre, the we iterate up to 10 times to try to constrain Z_{gas} and q. First Z_{gas} is calculated from R_{23} and the initial guess for q, then we recalculates q using the Z_{gas} we just calculated and [O III]/[O II]. For the next iteration, the calculated q is then used to recalculate Z_{gas}. If the Z_{gas} difference between two iterations is $\Delta Z_{gas} < 0.01$ then the iterations stop and Z_{gas} and q are set for that fibre. If, after 10 iterations, there is no convergence, that fibre is flagged as a bad fit. This iteration makes use of R_{23}:

$$R_{23} = ([\text{O II}] + [\text{O III}])/\text{H}\beta \tag{A8}$$

For each iteration, Z_{gas} is calculated for the upper and lower branches as:

$$\log(\text{O/H})_{upper} + 12 = 9.72 - 0.777R_{23} - 0.951R_{23}^2$$
$$- 0.072R_{23}^3 - 0.811R_{23}^4$$
$$- \log(q)(0.0737 - 0.0713R_{23})$$
$$- 0.141R_{23}^2 + 0.0373R_{23}^3 - 0.058R_{23}^4 \tag{A9}$$

$$\log(\text{O/H})_{lower} + 12 = 9.40 + 4.65R_{23} - 3.17R_{23}^2$$
$$- \log(q)(0.272 + 0.547R_{23} - 0.513R_{23}^2) \tag{A10}$$

The ionization parameter q is then calculated from Z_{gas} using equation (A7), which is then used to recalculate Z_{gas} for the next iteration. This continues until convergence ($\Delta Z_{gas} < 0.01$), or up to 10 iterations, after which the fibre is flagged as a bad fit.

APPENDIX B: HOW Z_{gas} IS DETERMINED FOR OUR SEVEN DIFFERENT DIAGNOSTICS

Note: these techniques are nearly identical to those described in appendix A2 of Kewley & Ellison (2008).

(i) R_{23} – McGaugh (1991)
Assumed q: not fixed, models attempt to correct for variation in q using the [O III]/[O II] line ratio defined in y below.
Method: this method is doubly degenerate so which branch we are in is determined using [N II]/[O II] as described in equation (A1). McGaugh and Koblunicky performed detailed simulations of H II regions and have come up with the following analytical fits to the results from their models. These fits for the upper and lower branches are given in Kobulnicky, Kennicutt & Pizagno (1999):

$$x = \log(R_{23}) = \log(([O\,II] + [O\,III])/H\beta) \tag{B1}$$

$$y = \log\left(\frac{[O\,III]}{[O\,II]}\right) \tag{B2}$$

$$Z_{upper} = 12 - 2.939 - 0.2x - 0.237x^2 - 0.305x^3$$
$$- 0.0283x^4 - y(0.0047 - 0.0221x - 0.102x^2$$
$$- 0.0817x^3 - 0.00717x^4) \tag{B3}$$

$$Z_{lower} = 12 - 4.994 + 0.767x + 0.602x^2$$
$$- y(0.29 + 0.332x - 0.331x^2) \tag{B4}$$

(ii) R_{23} – Kobulnicky & Kewley (2004)
Assumed q: iterated upon.
Method: first the Z_{gas} and q are guessed at depending on if you are in the upper or lower R_{23} branch, then the code iterates to converge on a Z_{gas} and q. The equations behind this method are described in detail above in Appendix A.

(iii) R_{23} – Zaritsky et al. (1994)
Assumed q: No solution included.
Method: this method is derived by averaging the three previous calibrations for R_{23} done by Edmunds & Pagel (1984), Dopita & Evans (1986), and McCall, Rybski & Shields (1985). This method only works for the upper branch of the R_{23} double degeneracy. Which branch we are in is determined using [N II]/[O II] as described in equation (A1). If we are in the lower branch, the fibre is disregarded. If we are in the upper branch we use the following equations to calculate Z_{gas}:

$$x = \log(R_{23}) = \log(([O\,II] + [O\,III])/H\beta) \tag{B5}$$

$$Z_{upper} = 9.265 - 0.33x - 0.202x^2 - 0.207x^3 - 0.333x^4 \tag{B6}$$

(iv) [N II]/[O II] – Kewley & Dopita (2002)

Assumed q: 2×10^7, although q is nearly invariant for this Z_{gas} diagnostic.
Method: for the above assumed q, we set the line ratio equal to the following fourth degree polynomial for Z_{gas} (see table 3 from Kewley & Dopita 2002):

$$\log([N\,II]/[O\,II]) =$$
$$1106.87 - 532.154Z + 96.3733Z^2 - 7.81061Z^3 + 0.239282Z^4 \tag{B7}$$

The IDL function *fz_roots.pro* then solves for the roots of this polynomial to find Z_{gas}.

(v) ([O III]/Hβ)/([N II]/Hα) – Pettini & Pagel (2004)
Assumed q: none, fit is empirical
Method: empirical fit of line ratios to 137 H II regions, 131 have metallicities measured used the direct T_e method, while 6 are derived using strong line methods. Note that we use the Hβ/Hα line ratio to correct for extinction, so we fix Hβ/Hα to the same constant in all our data so this diagnostic is actually just based on the [O III]/[N II] line ratio. While this fit is empirical and does not correct for q, Kewley & Dopita (2002) shows that the [O III]/[N II] line ratio is strongly dependent on q.

$$x = \log\left(\frac{[O\,III]/H\beta}{[N\,II]/H\alpha}\right) \tag{B8}$$

$$Z = 8.73 - 0.32x \tag{B9}$$

(vi) [N II]/Hα – Denicoló et al. (2002)
Assumed q: none, fit is empirical.
Method: empirical fit to 236 galaxies. Approximately half are metal poor and half are metal rich to cover a wide range in Z_{gas}. A linear least squares fit to the data gives:

$$x = \log([N\,II]/H\alpha) \tag{B10}$$

$$Z = 9.12 + 0.73x \tag{B11}$$

This empirical fit covers a range of H II regions with $-2.5 < \log([N\,II]/H\alpha) < -0.3$ which corresponds to a range in Z_{gas} of 7.30 $< 12+\log(O/H) < 8.90$ in this fit. We consider values in our data of $\log([N\,II]/H\alpha) > -0.3$ corresponding to $12+\log(O/H) > 8.90$ to be an extrapolation of the fit. Fig. C1 in Appendix C1 shows this fit as a dashed line.

(vii) [N II]/Hα – Pettini & Pagel (2004)
Assumed q: none, fit is empirical
Method: empirical fit of line ratios to 137 H II regions, 131 have metallicities measured used the direct T_e method, while 6 are derived using strong line methods.

$$x = \log([N\,II]/H\alpha) \tag{B12}$$

$$Z = 9.37 + 2.03x + 1.26x^2 + 0.32x^3 \tag{B13}$$

The H II regions observed cover a range of $-2.5 < \log([N\,II]/H\alpha) < -0.3$ which corresponds to a range in Z_{gas} of $7.17 < 12+\log(O/H) < 8.87$ in this fit. We consider values in our data of $\log([N\,II]/H\alpha) > -0.3$ corresponding to $12+\log(O/H) > 8.87$ to be an extrapolation of the fit. Fig. C1 in Appendix C1 shows this fit as a solid line.

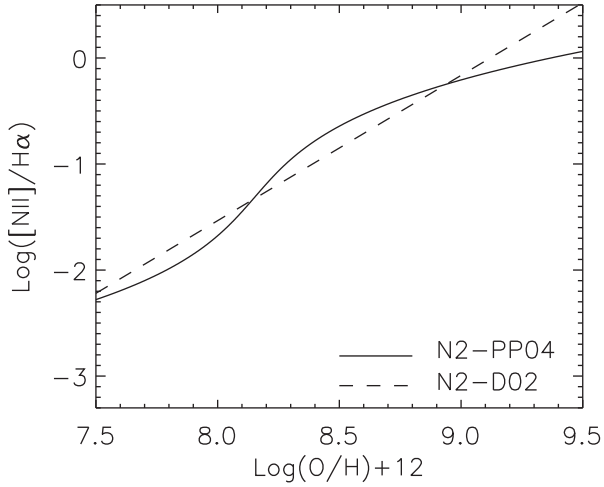## APPENDIX C: COMPARISON OF [N II]/Hα Z_{gas} DIAGNOSTICS

Figure C1. Plot showing the two empirical fits for the Z_{gas} calibrations based off the [N II]/Hα line ratio. The solid line denotes the empirical fit of a third order polynomial for N2-PP04 (Pettini & Pagel 2004) and the dashed line denotes the linear fit for N2-D02 (Denicoló et al. 2002). The axes are shown the with the same range as the top right plot in Fig. 8 for comparison to the theoretical fits from Kewley & Dopita (2002). For the Z_{gas} range covered in this study ($8.3 <$ log(O/H)+12 < 9.4), a change in [N II]/Hα leads to a larger change in Z_{gas} inferred from the N2-PP04 diagnostic than from the N2-D02 diagnostic. Details for these [N II]/Hα Z_{gas} calibrations can be found in Section 5.2 and Appendix B.

This paper has been typeset from a TEX/LATEX file prepared by the author.